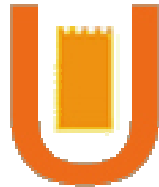# UNIVERSITY OF ROME "TOR VERGATA"

FACULTY OF ENGINEERING
Department of Mechanical Engineering

Ph.D. course
MATERIALS ENGINEERING

XXI Cycle

STUDY OF ANELASTIC PHENOMENA IN MATERIALS OF ENGINEERING INTEREST

Paolo Deodati

Tutor

Prof. Roberto Montanari

Table of contents

Chapter 4
Internal friction peak due to nitrogen in tungsten

PART II

Chapter 5
Nickel Based Superalloys

Chapter 6
Spark Plasma Sintering (SPS)

Chapter 7
Human Teeth

Introduction

The theoretical principles of anelastic phenomena in solids were formulated for the first time by C. Zener in $1937 - 1938$. Virtually at the same time N. N. Davidenkov formulated the principles of the nonlinear mechanics of materials. Special literature operates with various terms for describing inelastic phenomena in solids, for example, internal friction, physical acoustics, absorption of ultrasound, static and dynamic hysteresis loops, internal dissipation of energy, and damping of oscillations. In 1990 De Batist and Magalas suggested a generalized concept for the description of these phenomena known today as mechanical spectroscopy of materials. Mechanical spectroscopy (MS) studies absorption spectra of mechanical energy under the conditions of applied periodic external mechanical field. Mechanical spectroscopy is a powerful tool for the study of materials. In particular, it is shown that such a technique can help the mechanical characterisation of materials.

The elastic and anelastic properties of the material have been investigated by using a vibrating reed technique with electrostatic excitation and frequency modulation detection of flexural vibrations mode of cantilevered mounted reed samples.

All measurements of the internal friction (Q^{-1}) and of the resonance frequency (*f*) were performed from -150 °C up to 1000°C, so it was possible to determine, continuously, the dynamic Young modulus. This is an important step forward compared to traditional methods of tensile testing, because there are some problem to determine the elastic modulus at lower and higher temperature. With this method all the instrumentation errors was cleared.

In this work we have studied the elastic and anelastic properties of a wide range of materials:

- Titanium matrix composite (Ti6Al4V/SiC$_f$), Titanium alloys (SP700, Ti6Al4V)
- High nitrogen steel
- Tungsten
- Nickel based super alloys (single crystal and directional solidified)
- Nanostructured alloys
- Human teeth.

This work has been divided into two parts: the first one is based on anelastic relaxation phenomena and the second one is focused on irreversible phenomena.

Chapter 1

Internal Friction Theory

1.1 The anelasticity

Hooke's law establishes a linear relationship between stress and deformation in the elastic range, provided that the effort increases so infinitely slow so that the system state has the opportunity to follow changes of the load. In the elastic field, the energy stored throughout the system during the load is released during the unloading.

In this case the process is energetically reversible.

A repetition of cycles of loading and unloading will not cause any energy loss.

In the stress/deformation curve the energy stored by the system is represented by the area under the curve, therefore so that the area will be zero the two ways, corresponding to the increase and decrease the load must be the same.

About a real material, were the is an application of external load not infinitely slow (as in reality precisely), there is never an immediate adjustment of the system to the variation of this load, but it conforms after a certain period of time. This delay, due to physical reasons of different nature, implies a clear deviation from the "ideal" elastic behaviour characterized by the Hooke law. This process of loading and unloading of stress, applied in the range of reversibility, involves friction of a quantity of energy, precisely defined internal friction.

In the stress/deformation curve the loading way do not coincide with the unloading one, the cycle presents a hysteresis phenomena, and the area between the loading and unloading curve represent the energy loss in the cycle, namely the transformation of mechanical energy in heat.

In general the mechanical phenomena characterized by internal friction are called anelasticity.

The Hooke law describes the behaviour of an ideally elastic body.

Taking in account the time dependence of strain and deformation the Hooke law can be written as follow:

$$\sigma(t) = M\varepsilon(t) \qquad \text{(I-1)}$$

in this equation σ and ε are in linear relation.

In the real process we have to consider the derivate of the velocity of loading variation, so we have to introduce in Eq. I-1 the derivate, on time, of strain and deformation so we obtain:

$$a_1\sigma + a_2\dot{\sigma} = b_1\varepsilon + b_2\dot{\varepsilon} \qquad \text{(I-2)}$$

This equation describes quite well the behaviour of a real solid, so are called Standard Linear Solid (SLS).

So the equation can be written:

$$\sigma + \tau_\varepsilon\dot{\sigma} = M_r(\varepsilon + \tau_\sigma\dot{\varepsilon}) \qquad \text{(I-3)}$$

Where τ_ε is the relaxation time of the stress at constant deformation, τ_σ is the relaxation time of deformation at constant stress, M_r is the relaxed elastic modulus.

Applying at time t=0 a constant strain σ_0 the Eq. I-3 can be written:

$$M_r\varepsilon + M_r\tau_\sigma\dot{\varepsilon} = \sigma_0 \qquad \text{(I-4)}$$

The solution is:

$$\varepsilon(t) = \frac{\sigma_0}{M_r} + (\varepsilon_0 - \frac{\sigma_0}{M_r})e^{-t/\tau_\sigma}$$

The trend is showed in Fig.I-1
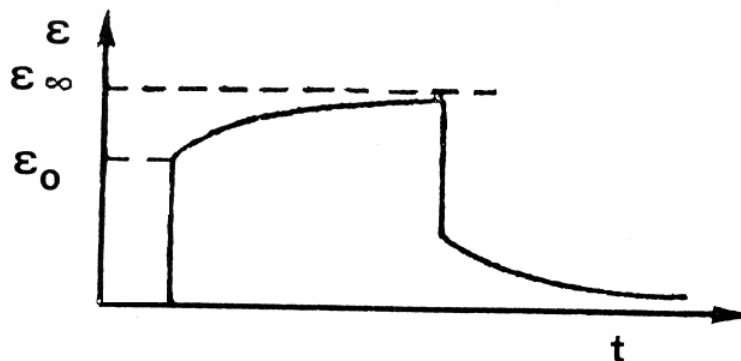
Fig. I-1

At loading point the deformation go instantaneously to ε_0 than grow exponentially until the value $\varepsilon_\infty = \sigma_0 / M_r$.

Figure I-2 show the stress deformation curve relatively at the same phenomena at σ constant.
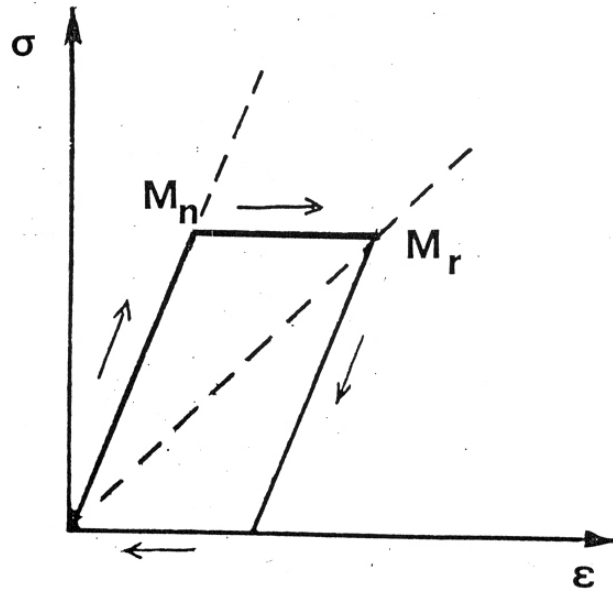
Fig. I-2 Stress deformation curve relatively at σ constant.

M_n and M_r are respectively the elastic modulus not relaxed and relaxed.

$M_n = \sigma_0 / \varepsilon_0$ represent the relation between the applied stress at time $t=0$ and the deformation, ε_0, that the solid assume instantaneously, while M_r correlate the stress and the deformation after the relaxation.

Imposing constant the deformation the eq. I-3 become

$$\sigma + \tau_\varepsilon \dot{\sigma} = M_r \varepsilon_0$$

And the solution is:

$$\sigma(t) = M_r \varepsilon_0 + (\sigma_0 - M_r \varepsilon_0) e^{-t/\tau_\varepsilon}$$

The fig. I-3 show the trend of $\sigma(t)$ and $\varepsilon(t)$.
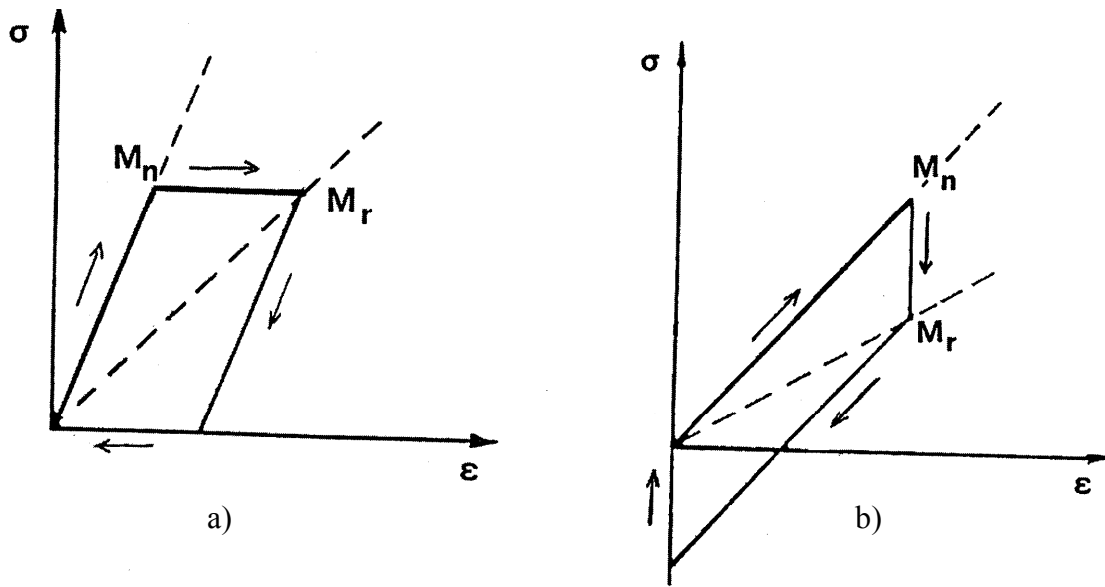
Fig. I-3 Stress deformation curve relatively at σ (a) and ε constant (b).

in the considered case of relaxing at stress and deformation constant, τ_σ and τ_ε determine the velocity with which the system going to the thermodynamic equilibrium.

1.2 Dynamic properties of the standard anelastic solid

If the applied stress to the sample is cyclical, in particular sinusoidal, stress and deformation can be defined, using the complex notation, as follows:

$$\sigma(t) = \sigma_0 e^{i\omega t} \qquad \varepsilon(t) = \varepsilon_0 e^{i\omega t} \tag{I-5}$$

Replacing in the Eq. I-3 and simplifying we obtain:

$$\sigma_0 (1 + i\omega\tau_\varepsilon) = M_r (1 + i\omega\tau_\sigma)\varepsilon_0$$

It's now possible to define the complex modulus M_c

$$M_c = M_r \frac{(1 + i\omega\tau_\sigma)}{(1 + i\omega\tau_\varepsilon)}$$

M_c is a complex quantity so σ(t) and ε (t) are out of phase, and if we indicate with δ the phase angle we can consider tan (δ) the measure of the loss energy

$$\tan\delta = \frac{\text{Im}(M_c)}{\text{Re}(M_c)} = \omega\frac{(\tau_\sigma - \tau_\varepsilon)}{(1+\omega^2\tau_\sigma\tau_\varepsilon)} = [(\frac{M_n - M_r}{\overline{M}})][\frac{\omega\overline{\tau}}{(1+\omega^2\overline{\tau}^2)}] \qquad (I\text{-}6)$$

The first factor it's the measure of the relatively variation of stress and deformation during the relaxation.

The second factor determines the dependence of the internal friction on the frequency. We obtain the maximum value of tanδ when ωτ=1.

Defining Dynamic Modulus the component of the Complex Modulus responsible of the component of the stress in phase with the deformation, that's the real part of the complex modulus

$$M_\omega = M_r(1+\omega^2\overline{\tau}^2) = M_n - \frac{(M_n - M_r)}{(1+\omega^2\overline{\tau}^2)}$$
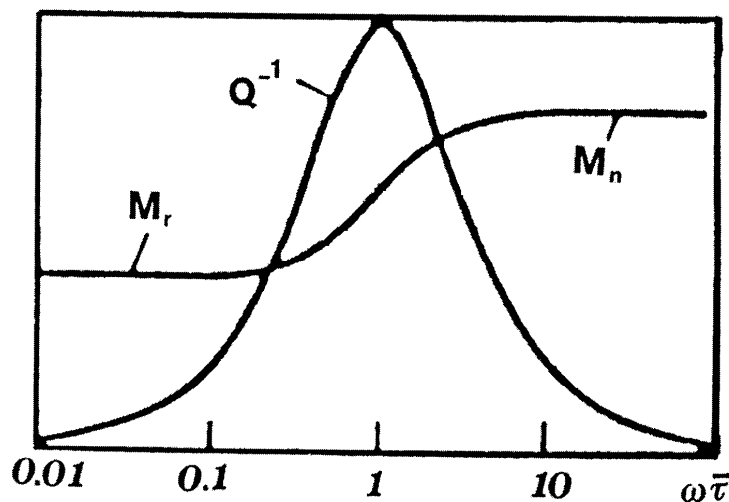
Fig. 4 Trend of tanδ and M$_\omega$ versus frequency

From figure I-4 we can observe:

–   At lower frequency there isn't energy loss due to the lack of time for the deformation to follow the applied stress. The relationship between stress and deformation in characterized by M_r.

–   At higher frequency the relaxation can not proceed due to the time less, and the internal friction go to zero again. The relationship between stress and deformation in characterized by M_n.

– At intermediate frequency, with $\omega\bar{\tau} \cong 1$, we obtain the maxima amplitude of internal friction. The value of the modulus is included between M_r and M_n.

1.3 Measurement of internal friction

There are several ways to measure the internal friction of metal materials, here we describe only the method of frequency modulation, one of the most widely used for precision and reliability of results.

The frequency modulation method is based on the electric conversion of a mechanical vibration: the sample excited electro statically by an electrode become in vibration and the consequent variation of capacity of sample/electrode modulate an oscillator. Working with a single electrode is of great importance because it reduces the parasitic capacitance, the noise due to the secondary mechanical system and also allows to operate in a wide temperature range.

The high sensitivity of this method, that allows to use one electrode not in contact with the sample, reduces the instability of the measure and provides the ability to appropriately adjust the distance electrode/sample via software.

Specimen and electrode can be considered like the plate of a condenser and the mechanical vibration of the sample, in resonance, cause changes of the capacitance.

These capacity variation modulate in frequency a periodic electrical signal; the variation of the pulse carrier is :

$$\Delta\omega = -\frac{1}{2}\omega_h \frac{\Delta C}{C}$$

Were ω_h is the carrier pulse and $\Delta C/C$ is the variation of the capacity of the system due to the mechanical vibration.

The amplitude of the modulation is proportional to the variation of capacity, which clearly show the importance of reducing parasitic capacitance.

In the measurement of internal friction of material in resonance, the shape of the sample have a great importance because the equation of propagation of elastic waves in solid can be solved with good approximation only for simple geometries.

The most used shape are reeds and circular plates, in this work we used only the first one.

Starting from the equation of propagation of elastic waves in solid it's possible to know the frequencies of the sample.

The electronic noise can be minimized by the use of appropriate filters while on the friction of air is necessary to perform the measure in vacuum with pressure values of up to 10^{-2} torr.

An internal friction measure is performed by placing the specimen in resonance and after a certain time removing the signal of excitement; the way in which the sample is de-energized and losses energy depends only on the internal structure, if as we have said, become irrelevant external factors of friction.

The mechanical vibration of the sample modulate in frequency an electrical signal, then this will be sufficient to demodulate the signal and then amplify it in order to obtain an electrical signal proportional in amplitude to changes in capacity specimen / electrode.

Removing the exciting signal the mechanical vibration, owing to internal friction of energy, decrease in amplitude and the electrical signal in output have an sinusoidal damped trend.

The energy loss in the half-cycle, called Q^{-1}, can be written by:

$$Q^{-1} = \frac{d}{\pi} = \frac{1}{n\pi} \ln\left(\frac{V_0}{V_n}\right) = tg\delta = \frac{1}{2\pi}\frac{\Delta E}{E} = \frac{\omega_2 - \omega_1}{\omega_0}$$
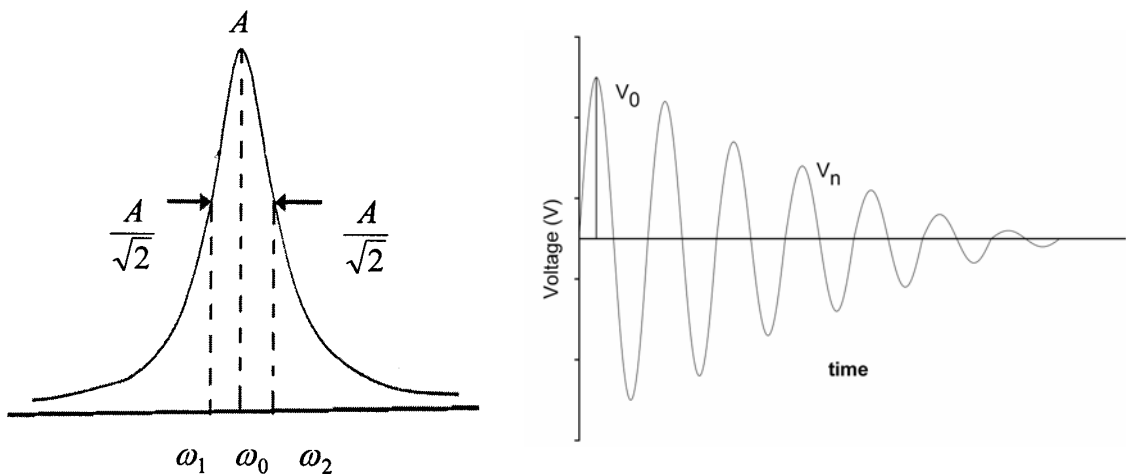
Fig. I-5 Two methods for determine the Q^{-1}.

In this work we use the cantilever method as shown in figure I-6, and the equation of the propagation of the wave in solid is:

$$\frac{\partial^2 y}{\partial t^2} + a^2 \frac{\partial^4 y}{\partial x^4} = 0$$

Where $a^2 = \dfrac{EI}{\rho S}$, I moment of inertia, E the elastic modulus ρ the density and S is the area of the section of the sample.

With the boundary condition the differential equation can be written: $\cos HiL \cdot \cosh HiL = -1$, so the solution is the resonance frequency:

$$f_r = \frac{m^2 h}{2\pi \sqrt{12} L^2} \sqrt{\frac{E}{\rho}} \qquad (I-7)$$
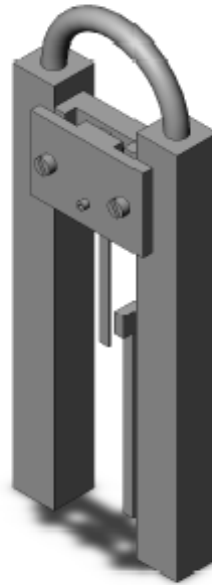
Fig. I-6 Model of cantilever of VRA 1604.

Where m is a constant (m=1.875), L the length, h the thickness and ρ the material density.

The main mechanism which produce anelastic damping are associated with the diffusive motion under stress of point defects, the motion of dislocations or part of them, and the motion of grain boundaries or other interfaces.

Points defect relaxation generally means an anelastic relaxation caused by a diffusive redistribution of point defects under the action of an applied stress. This necessarily requires an elastic interaction between the applied stress and the distortions of a crystal lattice created by the point defects, so that under the action of the external stress the

internal equilibrium distribution of the defects is changed and the driving force for a directed diffusion is produced.

One possibility , is the movement of interstitial atoms from compressed to dilated regions in an inhomogeneous stress field, i.e., a long range diffusion driven by the hydrostatic stress component. The other possibility, named reorientation, is related to the anisotropy of both the applied stress and the defect induced distortions. Compared with the movement of interstitial atoms relaxation, reorientation processes have much more practical importance for two reasons:

1. they apply to a much larger variety of point defects and their clusters;
2. they require only short-range diffusion, ideally over atomic distances.

So that the relaxation times are much shorter and more likely to cause internal friction of elastic vibrations practically relevant frequency ranges.

However, not all point defects in metals are subjected to a reorientation mechanism: some of them may cause damping, while others may not. This ability depends on specific symmetry relations and on the direction of the oscillating applied stress. The main condition is that the symmetry of the local elastic distortions, caused by the defects in the crystal lattice, is lower than the symmetry of the lattice itself; when specified in crystallographic terms, this is known as so-called selection rules for anelasticity.

The temperature of anelastic relaxation (i.e., of internal friction peak) is determined by the activation energy of diffusion of the phenomena and by the frequencies of vibrations.

The anelasticity phenomena are governed by a relaxation time (τ) as seen in equation I-3, i.e. τ is the time required for the deformation for reaching the equilibrium with the applied load.

We have also seen that the maxima amplitude of internal friction it is observable when $\omega\tau \cong 1$, so we can express the relaxation time in the from:

$$\tau = \tau_0 e^{\frac{H}{RT}} \qquad\qquad\qquad \text{(I-8)}$$

The equation of a Debye peak show that, to trace out a peak reasonably completely, requires the ability to vary ω over about two decades. For a resonance method, this requirement usually means that several specimens, possibly vibrating in different modes, must be used to cover the range. There is, however, another way of tracing out the peak, namely, by varying τ while keeping ω constant.

So imposing that $\omega\tau \cong 1$ and substituting in the eq. I-8 we obtain:

$$\ln \omega\tau = \ln \omega\tau_0 + \left(\frac{H}{R}\right)\left(\frac{1}{T}\right)$$

So that there is a linear relation between $\ln\omega\tau$ and the reciprocal absolute temperature. It is clear then, that a plot of a given dynamic response function versus Q/RT differs from a plot of the same function versus $\ln\omega\tau$ only by a constant shift parallel to the abscissa. On the other hand, a plot versus 1/T involves an additional change in the scale of the abscissa by the factor H/R.

For the case of a Debye peak, the condition that $\ln\omega\tau = 0$ at the peak gives

$$\ln \omega\tau_0 + \left(\frac{H}{R}\right)\left(\frac{1}{T_p}\right) = 0 \qquad\qquad (I-9)$$

Where T_p is the temperature at the peak. If a series of peaks is obtained at a number of different frequencies, a straight line plot can be made of $\ln\omega$ versus $1/T_p$, whose slope is then H/R. this method, wich is one of the most common ways of obtain the activation energy.

Often it is desirable to obtain an approximate value for the activation energy knowing only the peak temperature at one frequency, or conversely, knowing H, one may wish to determine at what temperature the peak will appear for a given frequency.

These objectives can only be accomplished if the value of τ_0 is known. From the type of phenomenon occurring, one can often estimate τ_0 to within an order of magnitude, and then estimate H from T_p or vice versa, using Eq. (I-9). In practice, such estimates are made so often that it is convenient to have a graph from which one ca read the values directly.

In cases in which data are given at only two frequencies ω_1 ω_2, it is convenient to use the relation

$$\ln\left(\frac{\omega_2}{\omega_1}\right) = \left(\frac{H}{R}\right)\left(\frac{1}{T_{p1}} - \frac{1}{T_{p2}}\right) \tag{I-10}$$

To calculate the activation energy from the shift, $(T^{-1}_{p1} - T^{-1}_{p2})$, in the peak position. A disadvantage of this simple procedure is that the location of the peak temperature is difficult to determine with high precision. It is therefore useful to note that Eq. I-8 applies not only to the shift of the peak temperature itself, but also to the shift of every point of the peak. To improve this statement, we need only note that any normalized dynamic response function of a standard anelastic solid is a function only of the product $\omega\tau$.

Chapter 2

Titanium Composite

2.1 Introduction.

A great effort has been made in the last 20 years to develop new composites with Ti-alloy matrix reinforced by long ceramic fibres [II-1-7], which result equipped unidirectional with high-performance. About that the research and development about specific components are still active in many countries and few technical details are published in this regard.

In a conventional aircraft engine, most of the weight depends by mechanical components as rotors or anchorages, that a lot of parts is in the rotation during work condition. So it would be desirable to decrease the weight of the external elements to reduce the radial contribution. An high savings about this weight it is possible to have by the composites, that reduce the need for heavy structures through their high strength along the circle by optimal radial property.

The Ti6Al4V-SiC$_f$ composite has proved a promising material for aeronautical applications including turbine components and structural high stressed parts (Fig.II-1), and however that applications including high thermic-mechanical stresses.
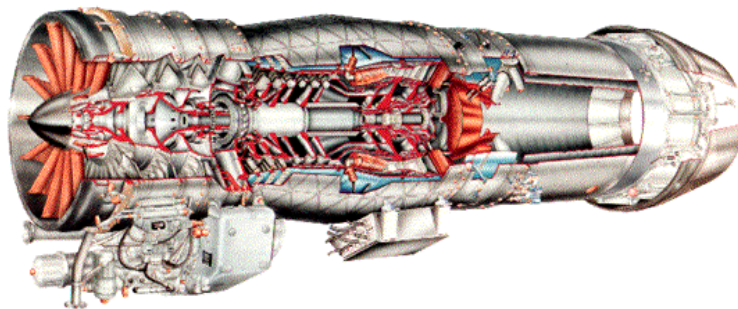

Fig. II-1 Application for the composite Ti6Al4V-SiC$_f$

To value the real suitability of the material, in this section several studies have been carried out especially about the fiber /matrix interface. In fact mechanical behaviour is governed especially by the fibre-matrix interface where diffusion of atomic species and

chemical reactions may occur leading to structural instability. So the main target of this work was to assess how mechanical and micro-chemical properties are affected by long-term heat treatments.

Moreover an important part of the experimental study has been the comparison between two type of the aforesaid composite, different about their specific fabrication process.

2.2 State of the art

Since the real and the potential Ti6Al4V-SiC applications are attractive for both industrial and scientific aim, especially in recent years various studies about the chemical, thermal mechanical characterization of this material has been developed.

The studies have been directed mainly to microstructural analysis of the fiber-matrix interface and to the diffusion kinetics about the same area, trying to predict and to monitor any changes in the mechanical properties of the material.

In most cases the situation has been studied by SEM and TEM micrograph analysis, or XPS and AES technical, adopted on the perpendicular plane to the major axis of fiber. In particular firstly there the interaction between C and Ti at moderate temperature (between 400 and 750 ° C) has been reported. At these temperatures during short heat exposure time, there is the formation of a titanium carbide compound TiC, controlled by the diffusion of Ti in C [II-8]. The study element diffusion evaluated through the XPS spectrum, the analysis of the thickness of the carbide layer and in particular the comparison with the more general diffusion theories, have reported discrepancies in the results [II-8].

These discrepancies appear to be due to difficulties about the assessing the real value of the carbide thickness and the activation energy for the diffusion of C in TiC, higher in this case than for the diffusion C-Ti [II-8].

The complexity of the diffusion phenomena increases logically on the interface zone between the fiber and the matrix of a composite material. First, by the literature this situation seems to be confirmed, i.e. the formation of titanium carbide increase with the temperature. The presence of SiC fibers coated with a carbon layer also includes a complex diffusion that involves more elements and especially the aforesaid carbon layer degradation. A situation, can cause the contact Ti-SiC and the formation of elements such as Ti_5Si_3. In fact, while with the presence of the carbon layer it is possible to note the presence of only TiC in the form of thin particle, with the following contact SiC-matrix layer, adjacent to the matrix and composed of a mixture of TiC particle and

Ti$_5$Si$_3$, forms near the already constituted TiC layer. This fact means that both the C that the Si take part in the diffusion reactions [II-9].

In the reaction zone presence of elements apparently "unrelated" were detected, too. In fact on the fiber oxygen high concentrations has been identified especially by Auger spectroscopy, but also the existence of high-temperature empty (~ 950 °C) in the same zone, due to a vacancy saturation [II-10]. To this point, about the interesting zone quantity of solid precipitates and solutions is a detectable, involving an hardness increase and ductility reduction of the areas on the matrix immediately adjacent with the fiber, with the consequent influence about the ability to transfer load from matrix to fiber [II-10].

After the measures of the elements present at the interface and their concentration, the diffusion kinetics evaluation is fundamental. Generally, a study of this kind begins by observing the thickness of the reaction zone by optical microscopy [II-11]. In this case the difficulties, however, are caused by the irregular nature of this area especially in the part devoted to the matrix. That's why you choose an "average" value thickness is placed.

It is known primarily as the formation rate of the reaction zone grows very rapidly with the temperature increasing of a heat treatment [II-11]. This growth can be characterized, as shown in [II-4], by a not constant value of the diffusion coefficients during the heat exposure time . This situation first is due to the interaction between the outer layer of carbon fiber and titanium (with formation of titanium carbide), then to the interaction with the SiC (with the formation of more complex reaction) that produces a second zone that may be related to different diffusion phenomena, as soon as the aforesaid layer is consumed [II-11].

About aluminium and vanadium, alloy elements in the matrix, they seem to be detected in the interface only in very little amount (especially vanadium can be found at the Ti$_5$Si$_3$). Howerer it results demonstrated that the rates of growth are lower in this case than that in the fiber- pure Ti diffusion, reflecting the influence of these factors about the kinetics of reactions.

2.3 Property and production

The studied material is a composite constituted by a titanium matrix in Ti6Al4V alloy, used in the 90% of the aerospace and aeronautical applications. About the micro-structural aspect, this alloy is a mixed phase $\alpha+\beta$ (with few percent of β phase), where the α phase is a {hcp} phase, β a {ccc} phase. About the additional elements in the alloy (Al and V), they act especially as stabilizing for the two phase into the titanium alloy: Al is a substitutional element in the α phase, V is an interstitial element in β phase.

Ti	Al	V	Fe	C	O_2	N_2	H_2
Balance	5,5÷6,76	3,5÷4,5	<0,25	<0,08	<0,2	<0,05	<0,015

Tab. II-1 Ti6Al4V chemical composition

About the SiC fibers, these are as long fibers reinforcement. The fibers, usually denominated by the mark SCS-6, have a diameter of 140 μm and they are produced by PVD deposition, where the SiC accretion occurs on a carbon precursory (Fig. II-2).
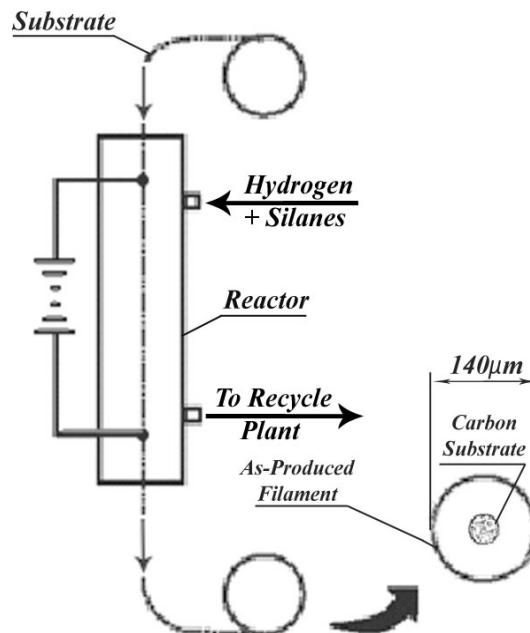
Fig. II-2 PVD technology production to the SiC fiber (type SCS-6) fabrication

The final microstructure consists in a fiber constituted by three concentric parts: a first part is the internal carbon core of the fiber; the second is a silicon carbide (by two different phases) part; the third is a carbon coating by a thickness of 3 μm (this part has used to increase the strength of the fiber by a curing of surface defects). The fiber structure is showed in Fig. II-3.
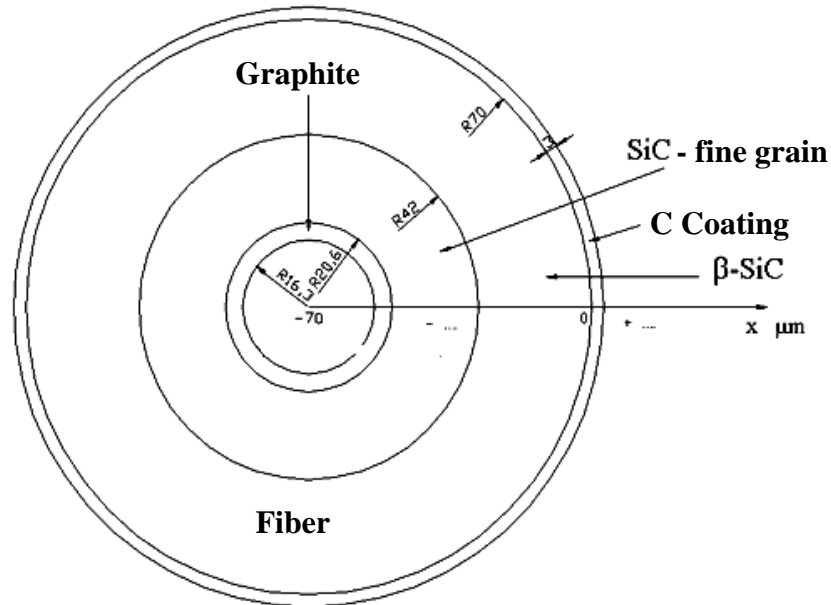
Fig. II-3 SCS-6 fiber microstructure on the trasversal section

The fiber property are summarized about the following points:

- Not too expensive costs
- High strenght
- High resistence to high temperatures (up 1200÷1400 °C)
- Low density
- Excellent chemical and corrosion resistance
- Good wettability by metals

As summarizing, in the Tab.II-2 is possible to see the principal mechanical and thermic property for the two components of the studied composite.

Matrix Ti6Al4V		Fiber SiC-C (SCS-6 type)	
Density	4,5 g/cm^3	Density	3 g/cm^3
Tensile Strength, Yield	830 MPa	Diameter	140 μm
Modulus of elasticity E	114 GPa	Modulus of elasticity E	400 GPa
Tensile Strength, Ultimate	980 MPa	Tensile Strength, Ultimate	4 GPa
C.T.E.	9 ppm/K	C.T.E.	4 ppm/K

Tab. II-2 Mechanical and thermic property for the components of the Ti6Al4V-SiC$_f$ composite

The composite has produced at C.S.M. laboratories in Castel Romano (Rome). It has been fabricated by hot isostatic pressure (HIP) in a multi-step process. Preforms (450 x 200 mm^2) made of four layers of unidirectional SCS-6 fibres alternated with five Ti6Al4V sheets (thickness of 0,6mm for the external, 0,1 for the internal sheets) have been prepared. They were then put inside a AISI 304 steel die, which was then evacuated (3x10^{-6} mbar) and sealed. HIP cycle (showed in Fig II-.4) has been realized by a hot isostatic press ASEA-QH21, which permits to control independently temperature and pressure. The material (Fig. II-5) was kept at 1163 K for 1.8 x 10^3 s under a pressure of 1200 bar; after cooling to room temperature the panels were extracted from the die. Finally by that for the experimental tests samples (with dimension of about 10 mm x 20 mm) have been obtained by spark erosion wire cutting (Fig. II-6).
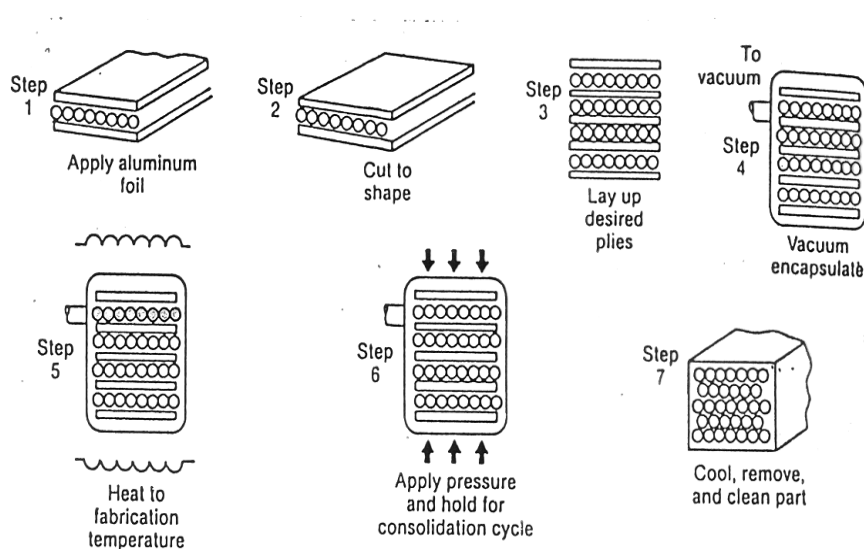
Fig. II-4 H.I.P. (Hot Isostatic Pressure) process to the fabrication of the composite

T_{max} (°C)	P_{max} (bar)	Time stop die (min)
890	1200	60-90

Tab. II-3 Process parameters for the HIP production
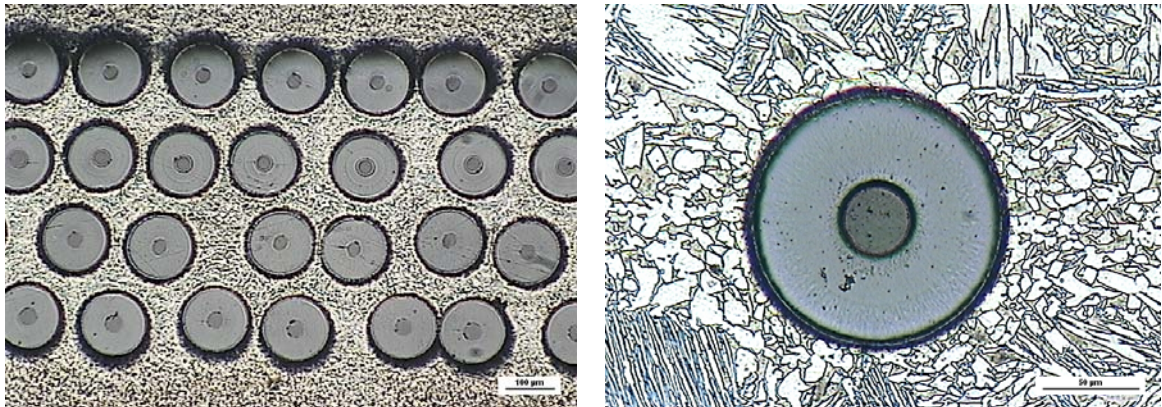

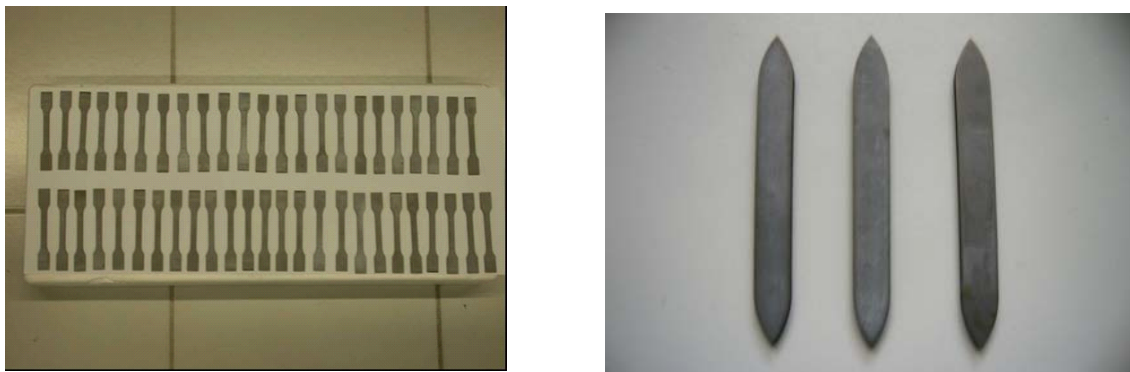**Fig. II-5 Ti6Al4V-SiC$_f$: result of the HIP process and particular micrography**

Fig. II-6 Samples of the composite obtained to the experimental tests

About the internal friction probes, samples constituted by only one layer of fibers have been tested, cause to the necessary vibrational characterization of the sample during the starting test.

The experimental development of this work has regarded the analysis and the studies also about the Ti6Al4V-SiC$_f$ composite produced by Roll Diffusion Bonding, thanks to a innovative pilot project realized at the C.S.M. laboratories. Details are present in [II-12].

The process consists in the manufacturing of composite samples reinforced by the unidirectional SCS-6 fibres, by the mean of a semi-continuous/continuous approach. The matrix is constituted by Ti6Al4V sheet.

The materials are assembled as a lay-up of two metallic sheets between that one layer of fibers is inserted, as shown in Fig. II-7.
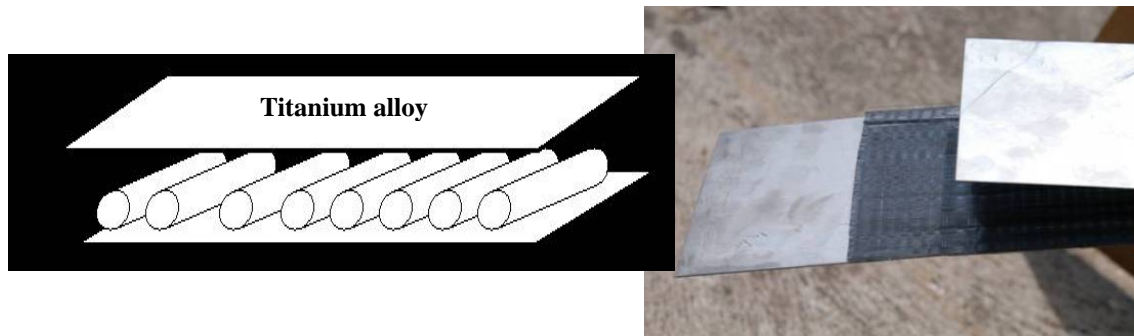
Fig. II-7 Composite lay-up and preparation of a precursor for the studied composite

During the Roll-Diffusion Bonding phase, the just-assembled sample (precursor) has been put under a backward and forward strip-tension under inert gas. As well as the pressure also the rolling speed and mill-stand temperature is computer controlled to improve the bonding reaction and this is the reason for the process called: Roll-Diffusion-Bonding (RDB). The metallic strips play the role of the composite matrix and under the combined effects of temperature and pressure flows from the surfaces through the fibre inter-spaces inside the fabric resulting in a complete metallic and ceramic-to-metal bonding.

The process phase is summarised as follows:

1- heating-up of a portion of the lay-up in the rolling-inert gas chamber;
2- plastic deformation of the metal matrix that starts the flow between the fibres;
3- first chemical reactions (inter-diffusion) at the fibre-matrix interfaces;

4- facing and contact between the two metal flows in the spaces between the fibres;

5- matrix recrystallisation in the joining surfaces;

The bonding process is stabilised and is completed in about 10 seconds. A further diffusion bonding phase is improved by mean of post-heat treatment just controlling the composite strip temperature to improve the diffusion strength.

The design parameters adopted for the pilot equipment first dimensioning are reported in Tab. II-4

Exercise temperature (°C)	Mean pressure in the contact arc (MPa)	Time (s)
900	500	6

Tab. II-4 Experimental reference parameters adopted for the pilot plant design

About the composite production, the adopted solution consist in the heating up a sealed chamber with inside the work rolls by mean of electrical resistance, in fact all other devices, micro-waves, induction, joule effect have shown higher complexity and higher costs. By this way a compacted working region has been manufactured (electric resistance are distributed on a crown of about 240 spatial degrees on each work roll) where has been possible to control both composite strip and rolling tool temperature, with also the atmosphere. In particular the large thermal mass of the rolling tools, simulated as an infinite heat source, is able to heat up the Ti-MMC precursor reaching 900°C in about few tenths of seconds.

To warranty a safe working temperature of the work-rolls has been necessary a special cooling circuit. Moreover to avoid an excessive cooling effect, it was necessary to design special "concentric work-rolls": an inner force-roll and an external high-temperature resistant alloy work-ring (Fig. II-8).
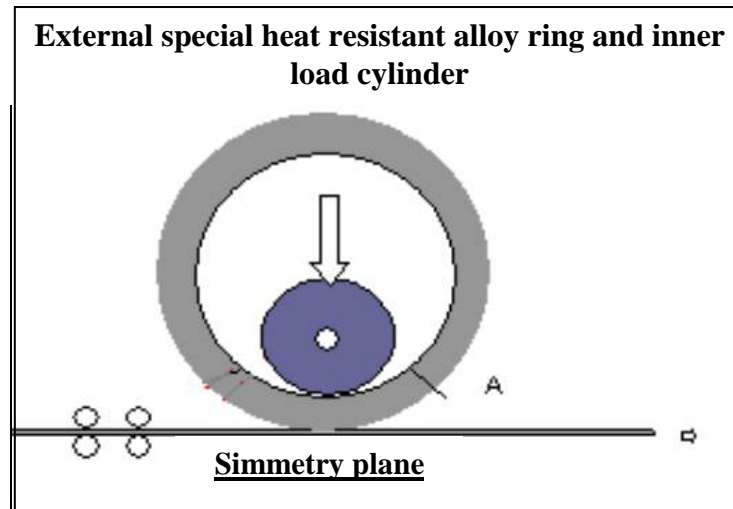
**Fig. II-8 Rolling Cylinders with the splitting of the thermal-tool (external ring)
and the pressure-tool (inner cylinder)**

This solution has permitted two advantages: the heating up only of the external special alloy-rings, and the manufacturing of cheap standard tool-steel inner-cooled work-rolls. Obviously the space between inner and external tool has been insulated with special ceramic shields in order to reduce the thermal dispersions.

The work-rolls rotation starts when the external ring high temperature surface reaches a temperature that is sufficient to warranty at least 900°C in the contact-arc.
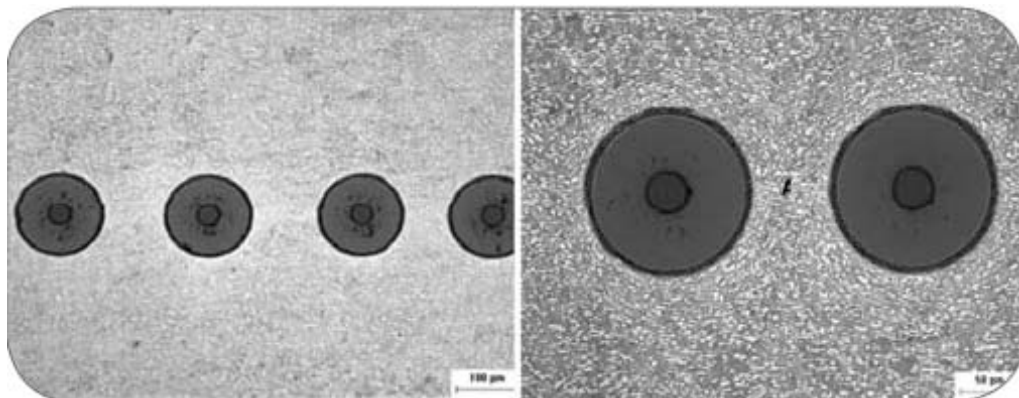
Fig. II-9 Ti6Al4V-SiC$_f$: result of the Roll Diffusion Bonding process and particular micrography

2.4 Low temperature damping

2.4.1 Experimental

In the Titanium fiber reinforced composites gaseous impurities such as hydrogen, nitrogen and oxygen absorbed during manufacturing processes and in operating conditions can strongly modify their mechanical behavior . In these composites further structural instability phenomena may occur at the fiber matrix interfaces determined by diffusion processes and chemical reaction thermally driven [II-13-15].

The Ti6Al4V (α +β) alloy, is characterized by a duplex hcp (α) and bcc (β) microstructure. The microstructure of the composite matrix consisted of the hcp α phase and a minority bcc β phase, approximately 4%. The monolithic Ti6Al4V alloy display a similar α+β microstructure.

It is known that the solubility of hydrogen in the β phase is much higher than in the α one. The reported hydrogen diffusion activation energy in the β phase is much lower than in the α phase [II-16].

Anelasticity measurements through mechanical spectroscopy has been extensively employed to understand details of point defects dynamics in Ti alloys [II-17] and to investigate transient or permanent damping effects depending on the evolution of thermal stresses at the fiber-matrix interfaces in composites [II-18].

The inverse mechanical quality factor (Q^{-1}) and the resonance frequency, proportional to the square root of the dynamic young modulus at constant density and shape :6 cm lenght, 0.5 cm width, 0.08 cm thickness. All measurements of the internal friction (Q^{-1}) and of the resonance frequency (f_r) , were performed in the 0.6-3.5 kHz frequency range at a strain amplitude $\varepsilon < 10^{-5}$ and a pressure in the vacuum chamber 10^{-4}-10^{-3} Pa. Before each thermal run of measurements , in the 80-350 K range at a constant heating rate of 1 K/min, all samples where thermally equilibrated at the lower temperature for 30 mins. All ageing treatments at temperatures in the 600-900 K range have been performed in a vacuum of 10^{-4} Pa .

2.4.2. Results

Fig. II-10 shows the internal friction and the resonance frequency vs. temperature for the monolithic Ti6Al4V alloy and the prepared fiber reinforced composite. A prominent peak thereafter indicated P_1, is observed in both materials at appoximately 120 K (1kHz), the relaxation strength is significantly enhanced in the composite in comparison with the monolithic matrix alloy. A second very broad peak P_2 centered at around 250 - 270 K is observed respectively in the alloy and the composite spectra. The background damping in the whole temperature range investigated appears higher in the composite.
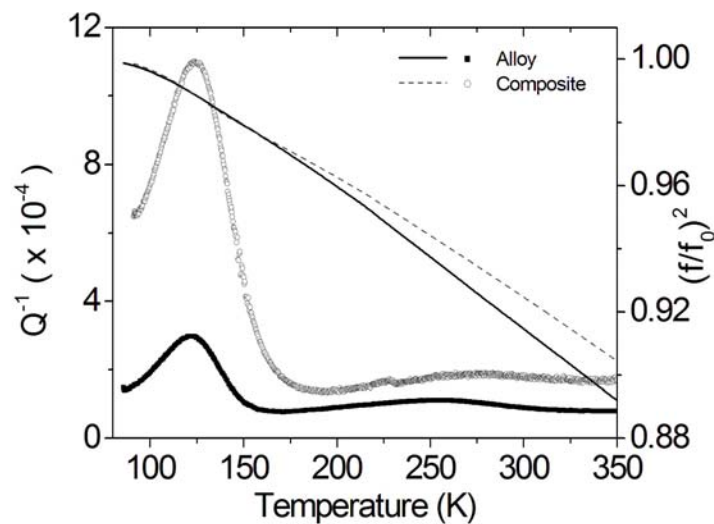
Fig. II-10 Internal friction and resonance frequency of the Ti6Al4V monolithic alloy and the Ti6Al4V-SiC$_f$ composite as prepared.

The relaxational nature of both peaks was confirmed by the shift of the peaks temperature with frequency. The values obtained for the activation energy and frequency factors are reported in Table II-5. After thermal ageing up to 900 K in a 10^{-4} Pa vacuum, a significant reduction of the P_1 peak relaxation strenght both in the monolithic alloy and the composite, up to 50%, is experienced, as can be seen in Figure II-11 .

Table II-5 Anelastic relaxation peaks parameters

Peak	P_1	P_2
Temperature (1 kHz)	120	$250 - 270$
Activation energy (eV)	0.21±0.02	0.50 ± 0.03
τ_0	10^{-15}	10^{-12}
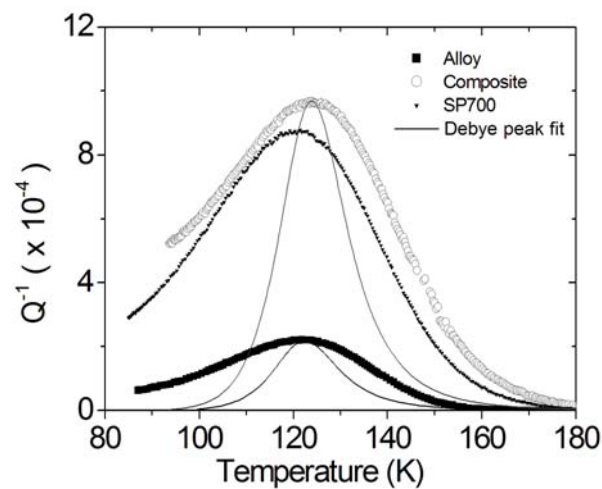
Fig. II-11 Internal friction and resonance frequency of the Ti6Al4V monolithic alloy and the Ti6Al4V-SiC$_f$ composite after ageing at 900 K.

In the composite the background damping with respect to the as received samples (Fig. II-10) increases with temperature, moreover a small reduction of the modulus (frequency) occurs with reference to the values experienced in as fabricated condition (Fig. II-10). The P_1 peak with a relaxation strenght similar to that observed on the composite and significantly higher than that of the monolithic matrix alloy is observed also on the SP-700 alloy (Fig. II-12).
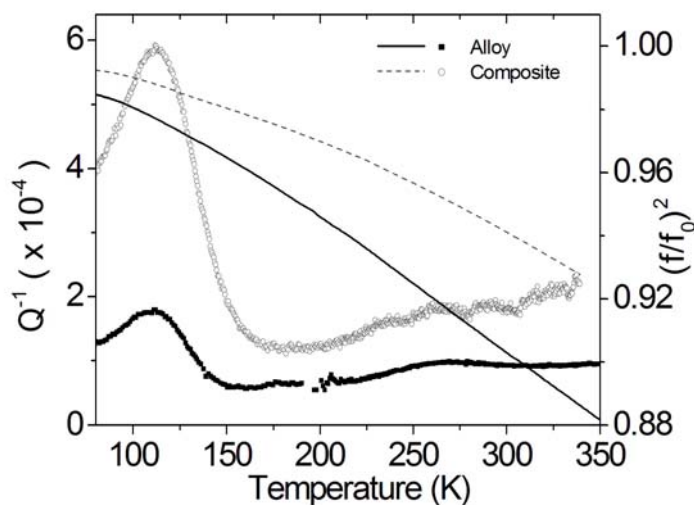
Fig. II-12 Comparison of the internal friction of the P1 peak for the composite, the alloy and SP-700. The P1 peak is broader with respect to that resulting by assuming a Debye relaxation.

On the basis of the internal friction spectra presented above, the P_1 peak can be attributed to hydrogen . The activation energy obtained from the peak shift (Table II-5) is slightly lower than that reported for hydrogen diffusion in the β phase of vanadium free titanium [II-15], but is slightly higher than those obtained by NMR in titanium with vanadium additions [II-20]. A value comparable with our results, within the uncertainty of measurements, was obtained by internal friction measurements on the Ti6Al4V alloy [II-21] . In the SP-700 alloy spectra (Fig.II-12), a well resolved peak having roughly the same activation energy of the Ti6Al4V alloy is present. In the SP-700 alloy measurements performed at low frequency [II-22] yeld similar activation energy. The prominent P_1 peak can be therefore attributed to a Snoek type relaxation caused by redistribution of interstitials hydrogen atoms in the β phase.

A significant difference in the P_1 relaxation strenght is yet observed (Fig. II-12) between the matrix alloy and the composite. Moreover the peak relaxation strenght in the SP-700 , mainly β phase alloy, is similar to that of the composite (Fig. II-12). The overall hydrogen content, measured was respectively : 116 ppm in the monolithic Ti6Al4V alloy, 187 ppm in the composite and 97 ppm in the SP-700 alloy. These values are within the low concentration solubility limit where a linear dependence of the (200) β phase XRD line breadth in Ti6Al4V was reported [II-22] and a proportionality

between the relaxation strenght and the amount of interstitial hydrogen responsible for Snoek relaxation , in the β phase is observed [II-23]. Therefore an apparent inconsistency for the differences in the relaxation strenght of the alloy and the composite Fig. II-12, could   be explained by assuming different   redistribution or segregation of hydrogen in different phases or at dislocations. In this regard it must be considered that dislocation density evaluated by XRD analysis [II-19] is one order of magnitude higher in the matrix alloy with respect to the composite.The relaxation strenght reduction Fig. II-12 after ageing, which is of the same order (50%) in the alloy and in the compositefor similar dynamic ageing treatments, is anyway consistent with a similar mechanism of hydrogen occupancy reduction of the interstitial sites in the bcc β phase responsible for the P_1 Snoek type relaxation. As regard the broad peak P_2 observed at around 250 K   the average activation energy obtained by the peak shift method in the matrix alloy , Table II-5, correspond   well within the measurement uncertainty, to that reported for hydrogen diffusion in the β phase [II-16] .

2.5 High temperature damping

2.5.1 Experimental

The microstructure and the mechanical properties of the Ti6Al4V-SiC$_f$ composite, have been extensively investigated in as-fabricated condition and after long-term (up to 1,000 h) heat treatments at T = 873 K, i.e. the temperature foreseen for its application in aeronautical engines [II-13-26]. The experimental results demonstrated that the mechanical characteristics of this composite are preserved even after the treatments in the most severe conditions examined by us. This is possible due to the formation of thin TiC sublayer between the matrix and the fibres during the fabrication process at high temperature (1163 K). Because the diffusion of C in TiC is much slower than that in α-Ti, the chemical reaction is retarded and the interface remains substantially stable.
This technique has been already used to study the monolithic alloy and a review of results is reported in the book of Blanter et al. [II-17]. In Mg composites, reinforced by C fibres, Schaller [II-27] has showed that thermal stress relaxation at the interface gives rise to transient mechanical loss due to dislocation motion.

IF results on the Ti6Al4V-SiC$_f$ composite have been reported in [II-19]: a new IF peak was explained by considering a mechanism of re-orientation of interstitial-substitutional (i-s) pairs, induced by the applied alternate stress. This hypothesis, based on previous observations [II-24] of chemical gradients at the fibre-matrix interface, needed to be supported further by some experimental evidence. In particular it was necessary to determine the depth distribution of C not affected by a possible contamination occurring during the mechanical preparation of sample surface. Therefore, a physical simulation has been made by depositing a layer of graphite on Ti6Al4V foils and by investigating the depth profiles of chemical elements by means of X-ray photoelectron spectroscopy (XPS) before and after sample annealing in an ultra-high-vacuum (UHV) chamber at 773 K, a temperature quite lower than that used in composite fabrication (1163 K).
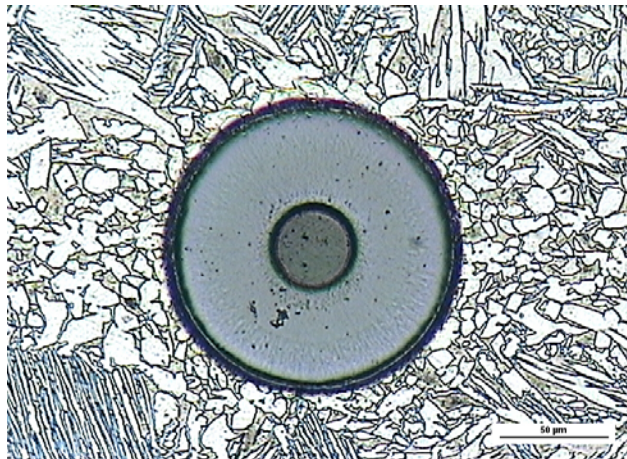
Fig. II-13. Cross-section of the composite.
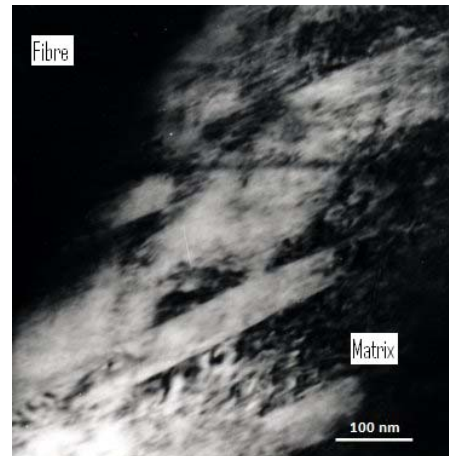
Fig. II-14. Microstructure of the composite near the fibre.

The matrix of the composite mainly consists of the hcp α phase with a minor amount (~ 4 %) of the bcc β phase, i.e. of the same structure of the monolithic Ti6Al4V alloy. As it is shown in Fig. II-13, the SCS-6 fibres are coated by a 3 μm thick carbon layer. TEM investigation demonstrated the following features: (i) good quality of the fibre-matrix interface without debonding, (ii) the presence of a layer of TiC between graphite coating and matrix, (iii) a banded structure of the matrix near the fibres (Fig. II-14), (iv) few free dislocations near the fibres. The dislocation density in the α phase, determined by X-ray diffraction (XRD), was 6.1 x 10^9 cm^{-2} for the composite and 5.5 x 10^{10} cm^{-2} for the monolithic alloy [II-25].

The dynamic modulus is proportional to f^2 thus its relative change as temperature increases can be described by the curve $(f/f_0)^2$ vs. T, being f_0 the resonance frequency at room temperature.

The temperature has been increased from room temperature to 1173 K at a heating rate of 1.7 x 10^{-2} Ks^{-1}. Strain amplitude was kept lower than 1 x 10^{-5}. For comparison, all these experiments have been performed for the samples of the composite and monolithic Ti6Al4V alloy.

For physical simulation of the interface between the matrix and graphite, ad hoc samples have been prepared by depositing (thermal evaporation) a thin layer of graphite on Ti6Al4V foils. Then these samples were annealed in UHV (< 10^{-8} mbar) at $T = 773$ K. XPS depth profiling of the samples before and after annealing has been performed in order to determine the chemical composition of the interface.

XPS experiments have been carried out in an ESCALAB MkII spectrometer (VG Scientific Ltd), equipped with standard Al Kα excitation source and a 5-channeltron detection system, at a base pressure of ~ 10^{-10} mbar. For the depth profiling, the Ar$^+$ ion gun has been set to the energy of 1.0 keV and the sample current density of about 2 μA cm^{-2}. The binding energy (BE) scale was calibrated by fixing the C 1s peak of the graphite at BE = 284.6 eV. The accuracy of the measured BE was $\pm$ 0.1 eV. More experimental details on XPS depth profiling have been reported elsewhere [II-15,25].

2.5.2 Results

The trends of Q^{-1} and $(f/f_0)^2$ vs. T for monolithic alloy and composite are shown in Fig. II-15. The Q^{-1} curve of the composite displays a peak superimposed to an exponentially increasing background. In correspondence of the peak, the modulus exhibits a change.
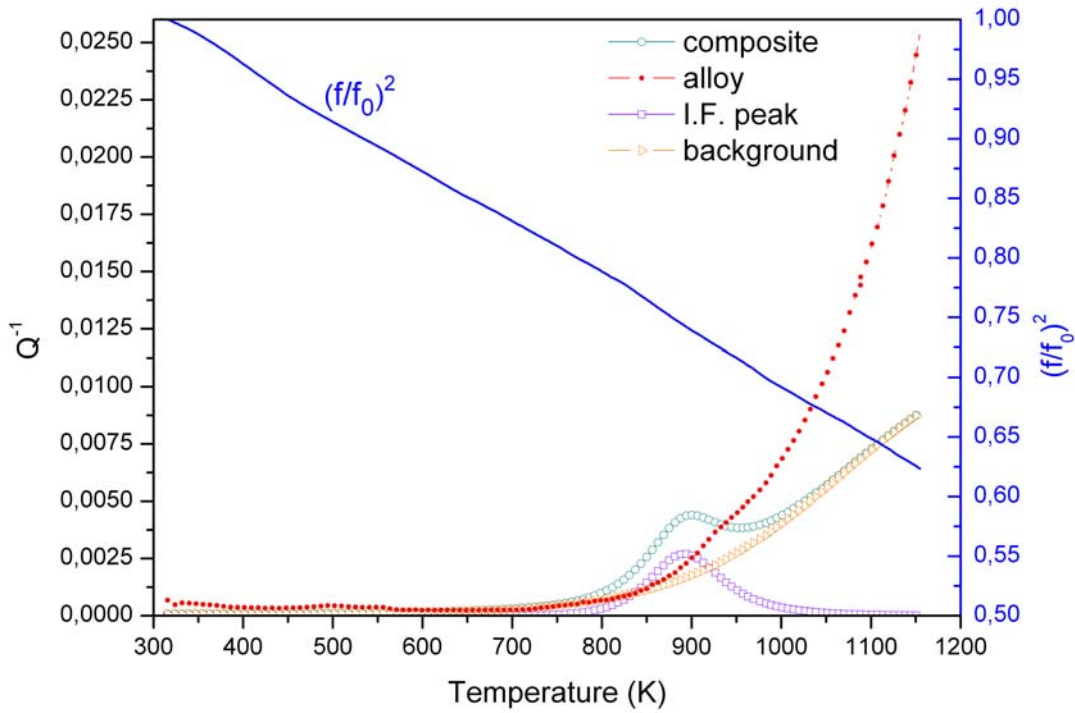
Fig. II-15 Q^{-1} and $(f/f_0)^2$ vs. T trends of the composite (f_0= 898 Hz). The Q^{-1}curve is the superposition of a Debye peak and an exponential background. The IF curve of the monolithic Ti6Al4V alloy is displayed for comparison.

The IF spectrum vs. temperature T can be fitted by the sum of two contributions: an exponential curve for the background, Q^{-1}_B (T), and a single Debye peak, Q^{-1}_P (TP):

$$Q^{-1}(T) = Q_B^{-1}(T) + Q_P^{-1}(T) = Q_B^{-1}(T) + \frac{\Delta}{2}\sec h \frac{H}{R}\left(\frac{1}{T} - \frac{1}{T_P}\right) \qquad \text{(II-1)}$$

being $\Delta/2$ the peak maximum, H the activation energy of the physical process giving rise to the IF peak, R the gas constant and T_P the temperature of peak centre. The peak position depends on the resonance frequency thus it is a relaxation peak. This is supported by another result: repeated test cycles on the same sample do not induce any permanent changes of resonance frequency f_0 and Q^{-1} at room temperature.

For a relaxation peak, the temperature of peak maximum T_P depends on the resonance frequency f :

$$\omega\tau = 2\pi f \tau_0 e^{\frac{H}{RT_P}} = 1.$$ (II-2)

Therefore, the activation energy H and the relaxation time τ_0 can be determined by the tests carried out with different resonance frequencies. From the Arrhenius plot in Fig. 16, the values of $H = 186$ kJ mol^{-1} and $\tau_0 = 2.3$ x 10^{-15} s have been obtained.
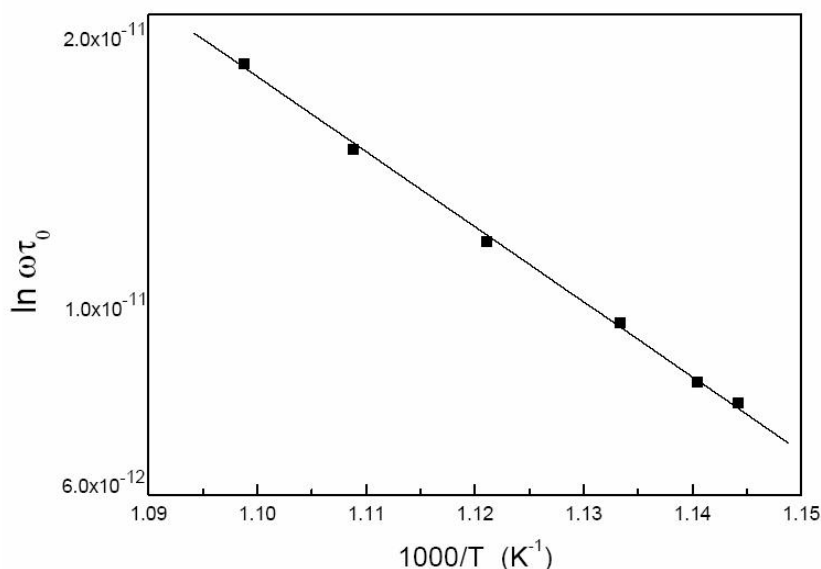
Fig. II-16 Arrhenius plot for the determination of H and τ_0

In the alloy, the IF peak was not observed, while the exponential background was higher than that of the composite.

XPS depth profiles of *ad hoc* samples (thin C film deposited on Ti6Al4V alloy) before and after annealing in UHV for 22 hours at 773 K are shown in Fig. II-17. Zero point of sputtering depth in both profiles corresponds to the surface of graphite overlayer characterized by C 1s peak at BE = 284.6 eV. Going deeper into the sample, the signal of C 1s remains at the same value of BE, however this fact does not indicate the continuation of graphitic structure, but corresponds to atomic C diffused into metallic alloy. A sublayer of native metal oxides (O 1s line) without any changes after annealing is observed at the graphite/metal interface. The presence of titanium carbide (C carbide line) in the as-prepared sample can be explained by the sample modification induced by

ion sputtering [II-15,25]. Such a modification, promoting the formation of TiC even at low ion energies, has been observed also in metallic Ti samples [II-26]. The increase of carbide signal in annealed sample (Fig. II-17b) is caused by thermal formation of TiC, which was detected previously in pure Ti samples [II-15,29]. However, the most important feature of micro-chemical composition of annealed sample is a deep diffusion (~ 100 nm) of atomic carbon (C 1s line in Fig. II-17b) into metallic matrix.

2.5.3 Discussion

The IF background of the monolithic Ti6Al4V alloy is noticeably higher than that of the composite. The background is strongly structure-sensitive [II-30] and the difference can be explained by considering a different contribution from dislocation damping in the two materials: the grain size is near the same (~ 30 μm), while they have a different dislocation density (one order of magnitude higher in the alloy).
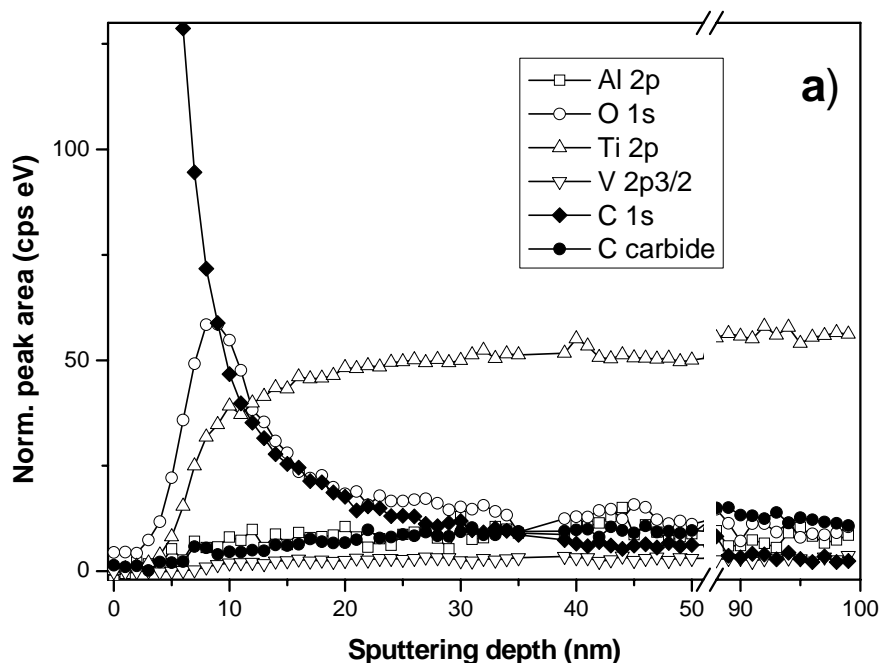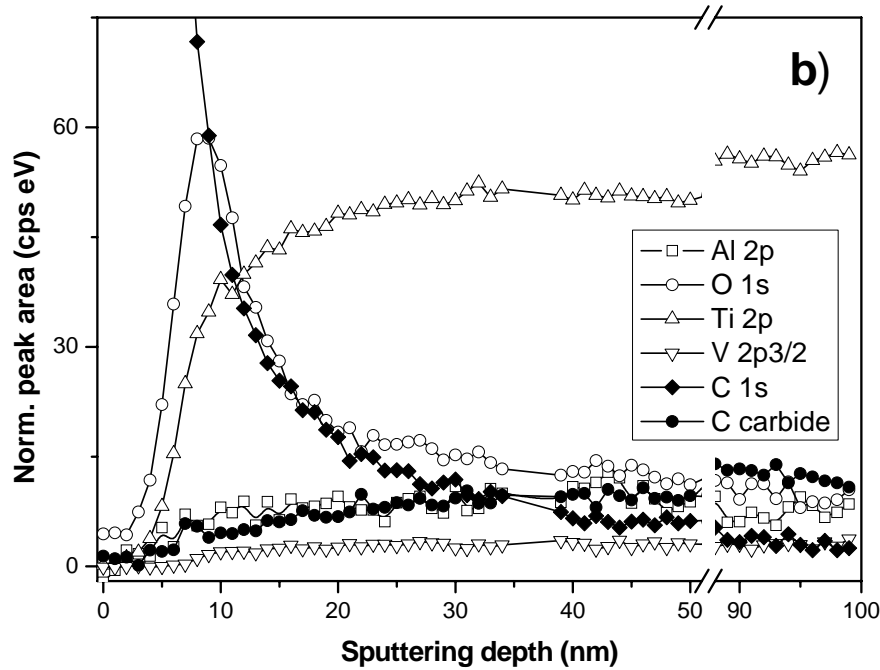
Fig. II-17 XPS depth profiles of of the C/Ti6Al4V sample before (a) and after (b) annealing in UHV at $T = $ 773 K.

The IF spectrum of the composite shows a Debye peak which is not observed in the alloy. Therefore, its origin is connected to the presence of the fibres and their effects on the surrounding matrix. To identify the physical origin of this peak, some hypotheses have been considered. Several phenomena, giving rise to the energy dissipation, may occur at the fibre-matrix interface, when the composite is subjected to thermal and/or mechanical stresses. At high stresses, plastic flow and interface de-bonding may occur, while at low stresses, the matrix and the fibres undergo only elastic distortions.

The effects of plastic flow and fibre-matrix de-bonding on damping have been discussed by Schaller [II-27]. Due to the different thermal expansion of matrix and fibres, internal stresses arise during the production process, when the samples are cooled from HIP temperature of 1163 K to room temperature. However, TEM observations show few free dislocations near the fibres. On the other hand, a simple calculation shows that these stresses are not sufficiently high to induce the formation of dislocations. The mean stress α_M in the matrix caused by cooling from HIP temperature (T_{HIP}) to room temperature (T_R) can be expressed by:

$$\sigma_M = \frac{E_F E_M}{(E_F \phi + E_M (1-\phi))} \phi(\alpha_M - \alpha_F)(T_{HIP} - T_R)$$ (II-3)

where E_F, α_F and E_M, α_M are the Young's modulus and the coefficient of thermal expansion of fibre and matrix, respectively; ϕ is the volume fraction of fibres. Introducing in Eq. (II-3) the values of E_F = 400 GPa, E_M = 114 GPa, α_M = 9.6 x 10^{-6} K^{-1}, α_F = 4.1 X 10^{-6} K^{-1} and ϕ = 0.3, was obtained σ_M = 350 MPa. This value is much lower than the matrix yield stress (850 MPa). Therefore, plastic flow and de-bonding at the fibre-matrix interface can be ruled out as possible causes of the IF peak. The attention has been focused then on elastic strains at the interface. This condition has been analysed by He and Lim [II-31] on the basis of the interfacial diffusion mechanism [II-32]. When a shear stress is applied to the interface, which is not perfectly planar on a microscopic scale, it is under tension at some locations and under compression at some others, as shown schematically in Fig. II-18. The stress gradient induces the atom diffusion along the interface, causing anelastic behaviour. However, the activation energy H = 186 kJ mol^{-1}, determined from present experiments, is quite different from those controlling the atomic diffusion of Ti, Al and V in both α and β phases, present in the matrix, thus the IF peak can not be ascribed to such a mechanism.
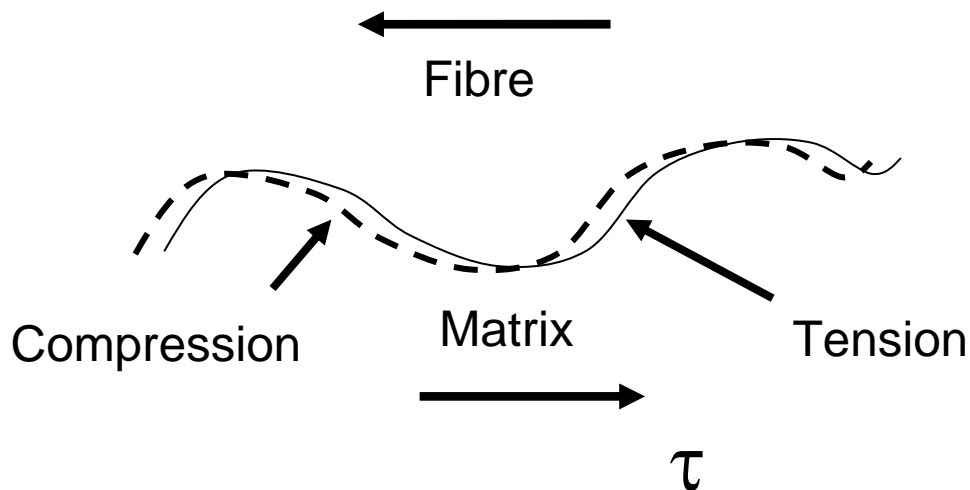

Fig. II-18 Schematic view of the fibre-matrix interface, which is not perfectly planar on a microscopic scale. When a shear stress is applied some locations are in tension, others in compression.

Also the diffusion processes inside the fibres, which have a stratified axial-symmetric structure, are not compatible with the peak activation energy because $H = 318$ kJ mol^{-1} for C in SiC [II-33] and $H = 911$ kJ mol^{-1} for Si in SiC [II-34] .

As shown in Fig. II-13, the fibres are coated by a carbon layer (thickness ≈ 3 µm) which separates SiC from the matrix. During the process of composite fabrication, carried out at high temperature (1163 K), carbon reacts with titanium, forming a thin layer (few nanometers thick) of titanium carbide (TiC) [II-15,17,25]. TiC thickness is increasing when the material is heated, but this kinetics is very slow. The activation energy for TiC growth, independently determined by Naka et al. [II-31], is of 194 kJ mol^{-1}, i.e. it is very close to that of IF peak. Therefore, the peak seems somehow connected to the growth of the TiC layer between the carbon coating of the fibre and the matrix. Furthermore, it is necessary to consider that TiC activation energy is very close to that of carbon diffusion in the α phase of Ti ($H^* = 182$ kJ mol^{-1}). The distribution of elemental composition determined by XPS depth profiling microchemical profiles (Fig. II-17) testifies that in the matrix around the fibre exists an extended zone (at least 100 nm wide), where the content of carbon is relatively high. Of course, this process can not occur in monolithic alloy, where a very low concentration carbon is homogeneously distributed. On these grounds, it is possible to suppose that the IF peak is caused by the stress-induced reorientation of i-s pairs (C-Al and C-V) in the hcp α phase of the matrix near the fibres. Fig. II-19 illustrates the presence of i-s pair in the α phase.

● Ti atoms
○ interstitial
⬡ substitutional
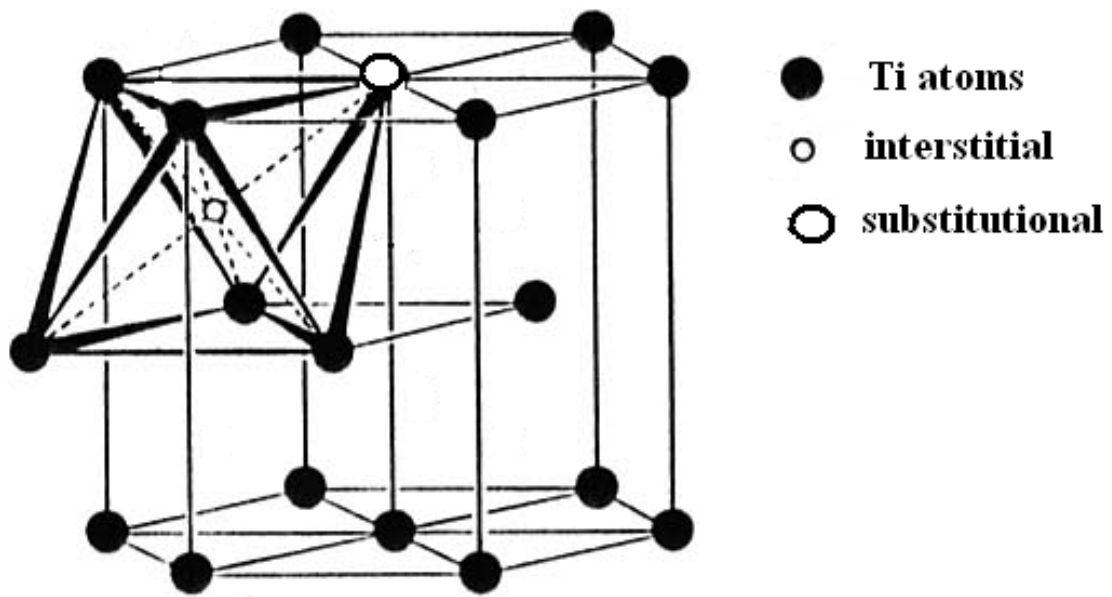
Fig. II-19 Interstitial substitutional (i-s) pair in the h.c.p. lattice of the composite α phase.

This mechanism for hcp metals has been discussed by Gupta & Weining [II-36] and Povolo & Bisogni [II-37].

2.6 High temperature comparison between Ti6Al4V-SiC$_f$ producted by HIP and RDB

2.6.1 Experimental

Roll Diffusion Bonding onding (RDB) is a new process, developed at C.S.M., for producing Ti composite composites reinforced by long fibres. The prototypal "diffusion bonding" plant p permits t ermits to co co-roll at high temperature in superplastic rolling field (under tempe temperature and strain rate control) rature foils of titanium alloy and fabrics made of SiC monofilaments.

The innovative RDB laboratory laboratory-equipment has been developed at C.S.M. laboratories and patented (n° 2006A000261, May 2006) [II-40].

The process permits to manufactur manufacture Ti-composite sheets with a mono-directional reinforcement of SiC fibres; in this case the matrix is the Ti6Al4V alloy and the reinforcement consists of fibres SCS-6, whose internal structure is displayed in Fig. II-20a). Two metallic strips are assembled with a layer of fibres between them (Fig. II-20b) and co-rolled.
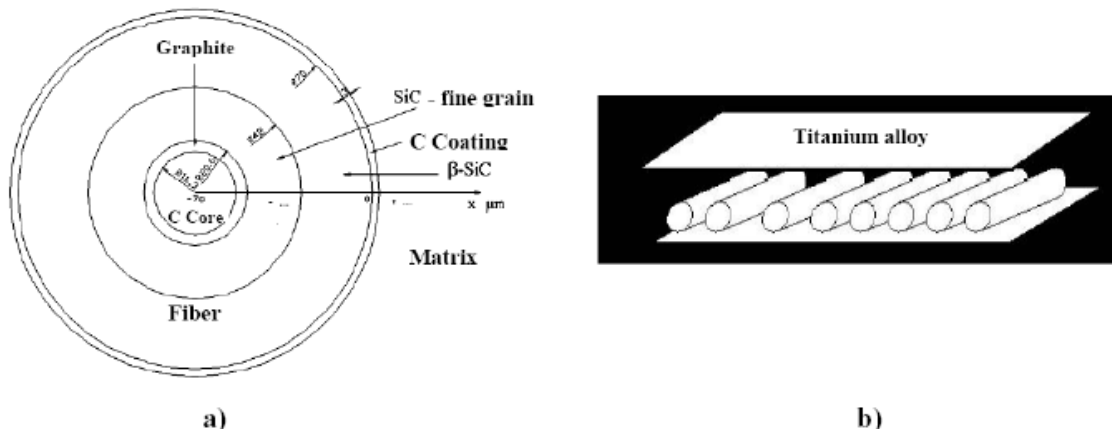
Fig. II-20 a) SCS-6 fibre structure. b) RDB composite layering.

The bonding process is completed in about 10 s. The main parameters adopted for the first dimensioning of the pilot plant are: process temperature = 900 °C, mean pressure in the contact arc = 500 MPa, time = 6 s. More details are reported in [II-40].

Samples for observations and analyses were obtained by spark erosion from composite sheets.

Optical and electron microscopy observations have been performed on cross-sections, after mechanical polishing and etching in Kroll reagent.

XPS and AES analyses, described elsewhere [II-38], have been done by using an Escalab Mk II spectrometer (VG Scientific, UK) equipped with 5-channeltron detection system. Photoelectrons were excited by using a standard Al $K\alpha$ excitation source, while Auger electrons were induced by electron gun LEG 200, operated at 10 keV and 1 – 10 nA current. XPS spectra were collected at constant analyzer pass energy of 20 eV, while AES spectra were registered in constant retard ratio (1:2) mode.

XRD measurements have been carried out using the Co-Kα radiation (λ = 1.79 Å). Spectra were collected in step step-scanning mode with 2 Θ steps of 0.05° and counting time of 2 s per step in the angular range 10° - 100 °.

High precision peak profiles of the most intense reflections of α phase were recorded with 2 Θ steps of 0.005° and counting time of 20 s per step.

Micro-hardness tests have been carried out on cross-sections of RDB and HIP composites.

Mechanical spectroscopy experiments, i.e. internal friction and dynamic modulus measurements, have been carried out on bar-shaped samples using the method of frequency modulation. The VRA 1604 apparatus used in the experiments has been described in deta detail in [II-41]. The resonance frequencies were in the he kHz range. The samples . have been heated from room temperature to 850 °C with a heating rate of 1.7 x 10^{-2} °Cs^{-1}.

2.6.2 Results and discussion

Micro-hardness of RDB composite is higher (500 HV) than that of HIP one (323 HV).

Fig. II-21 (a-b) compares the structures in t the cross section he sections of s RDB (a) and HIP (b) composites. It can be observe observed that the grains after RDB have smaller size and more homogeneous shape than those after HIP. The mean grain sizes are 5 and 30 μm for RDB and HIP composites respectively.

Sometimes samples of RDB composite, cut near the rim of the sheet, exhibit cavities due to an incomplete metal flow in the interstices between the fibres (Fig. II-21 c).
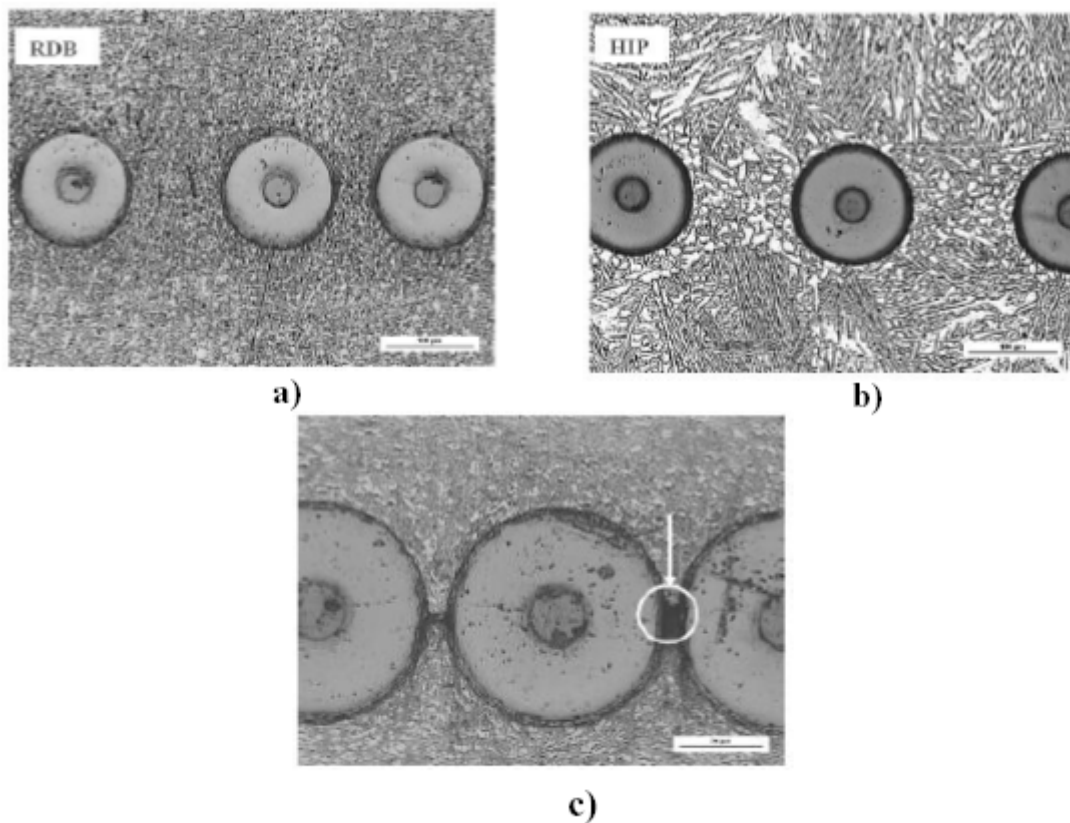
Fig. II-21 Cross sections of the RDB (a and c) and HIP composites. In c) a cavity due to an incomplete metal flow is evidencied.

XPS results are summarized in Table II-6, where the atomic concentrations and binding energy (BE) values of the main XPS peaks of elements (Ti, Al, C, Si and O) are reported reported. These peaks were assigned to the oxidized Ti (BE = 458.3 eV) and Al (BE = 74 ÷ 75 eV) in the alloy matrix and SiC fibres (C 1s at BE = 283.0 eV and Si 2p at BE = 100.2 eV). The lowest BE of Ti $2p_{3/2}$ peak ($\sim$ 454 eV) corresponds to metallic Ti. Moreover, the contribution of graphitic carbon (BE = 284.4 eV) from the core and external coating of the fibres was also revealed. The amount of surface oxides (BE = 530.5 ÷ 531.8 eV) and carbon contamination (BE = 285 eV) was significantly reduced after a brief cycle of Ar^+ sputtering at 2 keV. However, in XPS results it is difficult to identify the presence of TiC because the component of another carbide (SiC) is already present in C 1s spectra, while the first component in Ti 2p spectra (BE = 454.3 eV) could be due to carbide, but it overlaps with metallic Ti.

Tab II-6-XPS quantitative analyses: atomic concentrations and BE values of the elements in the composite (after 30 minutes of ion sputtering) and in the alloy (without fibres).

	Al 2p	C 1s		N 1s	O 1s		Si 2p	Ti 2p		
XPS quantitative analysis										
lapped zone (sputtered)										
at. %	4.5	17.3	28.8	-	17.3		27.6	4.4		
BE [eV]	75.2	283.0	284.4	-	531.8		100.2	454.3	456.3	458.3
alloy zone (unsputtered)										
at. %	2.0	-	40.0	2.0	44.0		-	12.0		
BE [eV]	74.3	-	285.0	400.2	530.5	532.7	-	453.5	-	458.4

The results of AES measurements carried out on the five points across the fibr fibre/matrix interface indicated in Fig. II-22a, are shown in Fig. II-22b. The peak intensity o he of AES spectra demonstrate that Ti-C inter inter-diffusion occurs during RDB process, in particular C deeply penetrates into the matrix.

Moreover, the O presence is confirmed in the fibre but especially in the matrix. Similar results have e been obtained from analyses of the HIP composite [II-37].
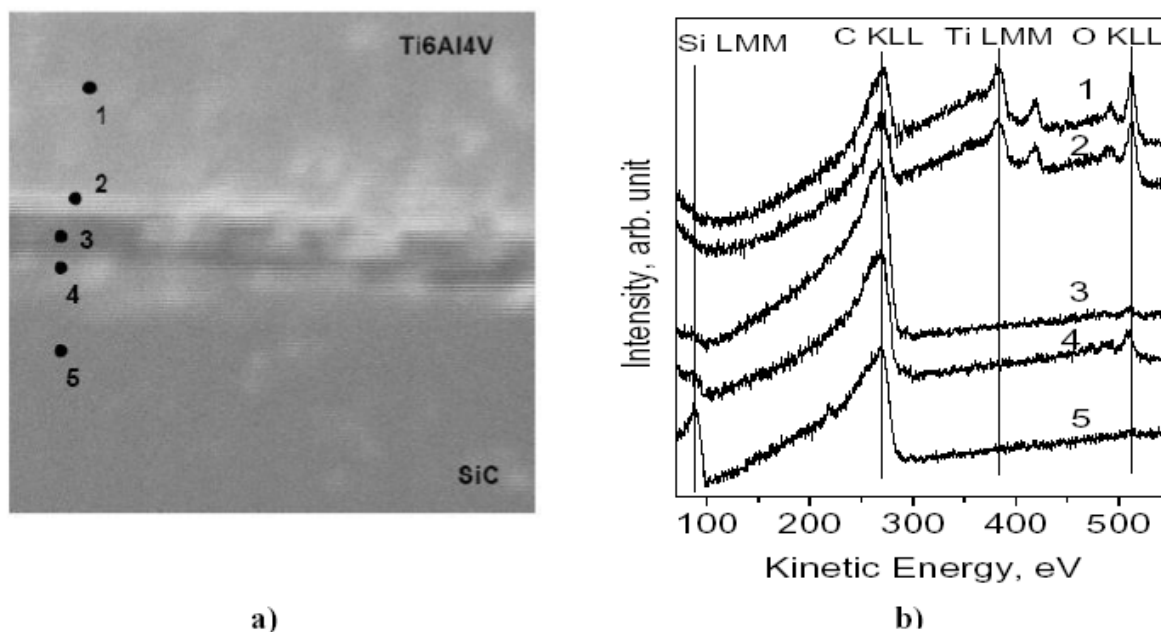
Fig. II-22 a) SEM image (80 x 80 μm^2) of teh fibre-matrix interface; the markers (1-5) indicate the pionts of Auger spectra acquisition. b) Auger spectra measured in the points 1-5.

XRD showed that peak profiles of RDB composite are quite broader than the corresponding profiles

of HIP composite. An example is displayed in Fig. II-23 where the intensities and positions of the {100 } peaks have been normalized for making easier the comparison.
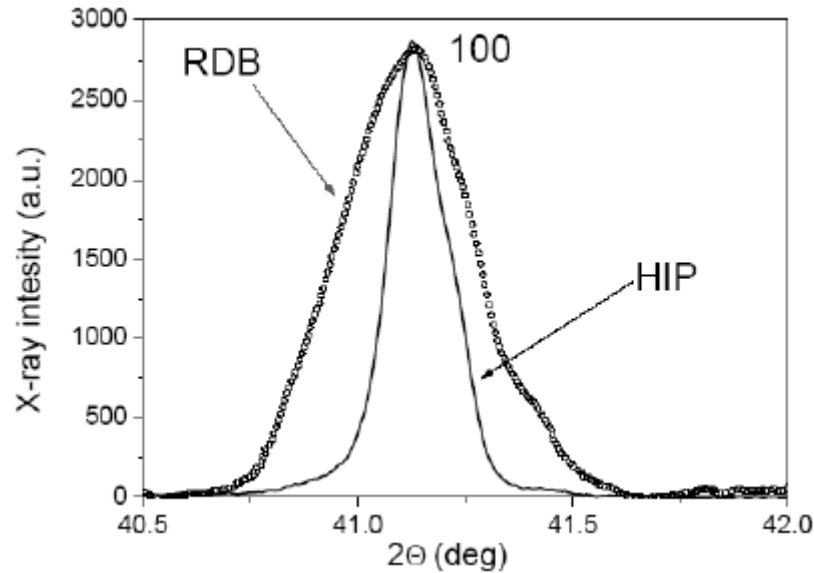
Fig. II-23 Precision {100 } peak profiles of HIP and RDB composites.

For each XRD reflection the total line broadening β_T , corrected from instrumental broadening, is basically due to two contributions, the size of coherently diffracting domains (β_D) and the micro micro-strains (β_ε). β_T can be written as:

$$\beta_T = \beta_D + \beta_\varepsilon = \frac{K\lambda}{D\cos\theta} + 2\varepsilon\tan\theta \qquad\qquad (II-4)$$

where D is the domain size, ε the average micro micro-strain, ϑ the Bragg angle, λ the X-ray wavelength and K a constant (= 0.89). In the case of Ti and Ti alloys the coherently diffracting domains are the grains.

Introducing in Eq. II-4 the D values determined for the two composites by metallographic observations

the micro micro-strain ε has been determined. Finally, the dislocation density ρ was calculated by means of the Williamson -Smallman relationship [II-42]:

$$\upsilon = \frac{\Xi \varepsilon^2}{k_0 b^2} \qquad\qquad \text{(II-5)}$$

where $\Xi = 16$ is a constant, b is the modulus of Burgers vector and $k_0 \cong 1$ is a factor depending on dislocation interaction. From this calculation the values of tion $\rho = 1.1$ x 10^{12} cm^{-2} for the RDB composite and $\rho = 6.0$ .0 x 10^{9} cm^{-2} for the HIP composite have been obtained obtained; they are in good agreement with the larger hardness exhibited by the RDB composite.

Fig. II-24 a) shows Q^{-1} and $(f/f_0)^2$ vs. T trends of the RDB composite. From the resonance frequency the elastic modulus E = 137 GPa has been determined determined, which is the same value of HIP composite. The Q^{-1} curve shows a peak at about 900 K superimposed to an exponentially erimposed increasing background, in correspondence of the peak the elastic modulus, proportional to f^{2}, exhibits a change. In tests with different frequencies the peak position changes indicating that the IF peak is a relaxation peak. The corresponding activation e energy nergy $H = 189$ kJ/mol and the relaxation time $\tau_0 = 2$ x 10 10^{-15} s are very close, inside the experimental error, to those determined for the HIP composite ($H = 186$ kJmol^{-1} , $\tau_0 = 2.3$ x 10^{-15} s) thus it is the same IF peak in the two materials. The anelastic phenomena giving rise to the peak have been extensively discussed in [II-19]: it was ascribed to stress induced reorientation of interstitial interstitial-substitutional (i-s) pairs (C-Al and C-V) in the hcp α phase of the matrix near the fibres according to the mechanism discussed by Gupta & Weining [II-36] and Povolo & Bisogni [II-37] for hcp metals.

Moreover, comparing the IF curve curves of the two materials in Fig. II-24 b) the RDB composite exhibits a higher background. The background is strongly structure-sensitive [II-30] thus the result can be easily explained by considering the smaller grain size and the higher dislocation density of the RDB composite which provide a greater contribution to the damping.

a)

b)
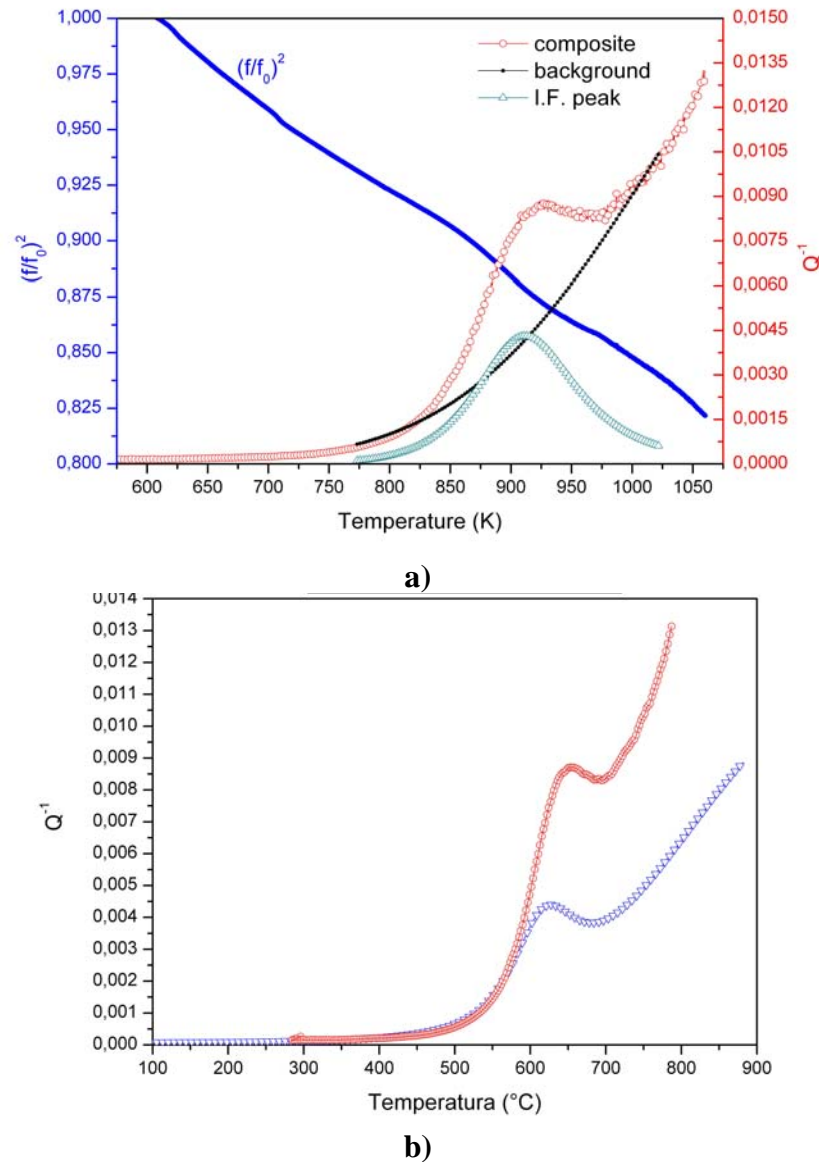
Fig. II-24 a) IF and *(f/f₀)²* trends of RDB composite. The IF curve exhibits the superposistion of an exponentially increasing background and a Debyepeak. b) Comparison between IF curves of RDB and HIP composites.

The microstructure of Ti6Al4V+SiC_f composite produc produced by RDB shows smaller grains and higher dislocation density with respect to that prepared by HIP; these features guarantee better mechanical properties.

As shown by XPS and AES analyses, the structure of the fibre fibre-matrix interface is substantially the same after RDB and HIP, therefore it is reasonable to expect a similar mechanical behaviour of the two materials after long term heat treatments at temperatures up to 600 °C. The mechanical properties of RDB composite should be scarcely affected by the treatments also in the most severe conditions (1000 hours), as

already observed for HIP composite. Experimental tests are underway to assess the hypothesis.

Also the IF spectra of the composites are similar. They exhibit a relaxation peak superimposed to an exponentially increasing background. The peak is due to C-Al and C-V pairs reorientation in the α phase of Ti6Al4V matrix around the fibres. The background, which is strongly structure sensitive, is higher for the RDB composite owing to its dislocation density and smaller grain size.

On the basis of present results RDB seems to be advantageous with respect to HIP for producing Ti-composites because the costs are lower and the mechanical properties better.

References

[II-1]   Debolt H.E., ''Boron and Other High Strength, Low Density Filamentary Reinforcing   Agents'', *Handbook of Composites*, ed. G. Lubin, Van Nostrand Reinhold, 1982, 69-76.

[II-2] Nourbakhsh S. and Margolin H., Proc. TMS annual meeting in Anaheim, CA, U.S.A., ''Metal and Ceramic Matrix Composites'', 75, (1990) p75.

[II-3] Mittnick M.A., Proc. TMS annual meeting in Anaheim, CA, U.S.A., ''Metal and Ceramic Matrix Composites'', 605, (1990) p605.

[II-4] Jha S.C., Forster J.A., Pandey A.K., Delagi R.G., *Cold Rolled Titanium Aluminide and Titanium Alloy Foils ISIJ International Vol.31* 10, 1991, pp.1267-1271.

[II-5] *Structural Materials Handbook, Vol. 2: new advanced materials(section XI)*, ed. European Space Agency, 1994.

[II-6] Clyne T.W., "3.7.12. Metal Matrix Composites: Matrices and Processing", *Encyclopaedia of Materials: Science and Technology, §3.7, Composites: MMC, CMC, PMC*, ed. A Mortensen, Elsevier, 2001, 1-14.

[II-7]   Upadhyaya D. et al., ''A Comparison of SCS-6/Ti-6Al-4V and Sigma SM1240/Ti-6Al-4V Composite System: a Microstructural Characterization'', *Recent Advances in Titanium Metal Matrix composites*, ed. F. H. Froes and J. Storer. Warrendale, PA: TMS The Minerals, Metals & Materials Society 139, 1995, 139-145.

[II-8] C.Arvieu, J.P.Manaud, J.M.Quenisset, *Interaction between titanium and carbon at moderate temperatures*, Journal of Alloys and Compounds 368 (2004), 116-122

[II-9] Y.C.Fu, N.L.Shi, D.Z.Zhang, R.Yang, *Effect of C coating on the interfacial microstructure and properties of SiC fiber-reinforced Ti matrix composites*, Materials Science and Engineering A426 (2006), 278-282

[II-10]   G.Das, *Study of the Reaction Zone in an SiC Reinforced Titanium Alloy Composite*, Metallurgical Transactions A Vol.21A (1990),1571-1578

[II-11] P.Martineau, R.Pailler, M.Lahaye, R.Naslain: *SiC filament/titanium matrix composites regarded as model composites (Part2: Fibre/matrix chemical interactions at high temperature)*, Journal of Materials Science 19 (1984), 2749-2769

[II-12] Testani C. and Ferrato F., *Sviluppo di un processo a basso costo per realizzare materiali compositi a matrice di titanio mediante "Roll Diffusion Bionding"*, La Metallurgia Italiana (2008), 9-14

[II-13] M.E. Tata, R. Montanari, C. Testani, G. Valdrè, La Metallurgia Italiana 7-8 (2005) 43.

[II-14] R. Donnini, S. Kaciulis, A. Mezzi, R. Montanari, M.E. Tata, C. Testani, La Metallurgia Italiana 10 (2007) 15.

[II-15] A. Mezzi, R. Donnini, S. Kaciulis, R. Montanari, C. Testani, Surface and Interface Analysis, 40 (2008) 277.

[II-16] R.J. Wasilewsky and G.L. Kehl, Metallurgia, 50 (1954) 225.

[II-17] M.S. Blanter, I.S. Golovin, H. Neuhauser, H.R. Sinning, Internal Friction in Metallic Materials-A Handbook, Springer Berlin 2007, p.261.

 [II-18] R. Schaller, Materials Science and Engineering A 442 (2006) 423

 [II-19] P. Deodati, R. Donnini, R. Montanari, C. Testani: Materials Science and Engineering A 521–522 (2009) 318

[II-20] C.Korn and D. Teitel , Phys. Stat. Sol (a) ,44 (1977) 755.

[II-21] Du Ja Ju, J. Physique ,C5, 42 (1981) 775.

[II-22] G.F. Pittinato and W. D. Hanna, Met. Trans. 3, (1972) 2905.

[II-23] X.S.Guan, H.Numakura, M.Koiwa, K.Hasegawa, C.Ouchi, Mat. Sci. Eng. A.272 (1999) 230

[II-24] R. Donnini, S. Kaciulis, A. Mezzi, R. Montanari, C. Testani, in: Proc. of the Conf. on Appl. Mechanics 2007, April 16-19, Malenovice, Czech Republic (2007), p. 55

[II-25] R. Donnini, S. Kaciulis, A. Mezzi, R. Montanari, C. Testani: Mater. Sci. Forum Vol. 604-605 (2009), p. 331.

[II-26] P. Deodati, R. Donnini, R. Montanari, C. Testani, T. Valente: Mater. Sci. Forum Vol. 604-605 (2009), p. 341.

[II-27] R. Schaller: Mater. Sci. Eng. A Vol. 442 (2006), p. 423.

 [II-28] J. Luthin, H. Plank, J. Roth, Ch. Linsmeier: Nucl. Instrum. Methods Phys. Res. Sect. 182 (2001), p. 218.

[II-29] C. Arvieu, J.P. Manaud, J.M. Quenisset: J. Alloys Compd. Vol. 368 (2004), p. 116.

[II-30] A.S. Nowick, B.S. Berry, in: Anelastic Relaxation in Crystalline Materials, Academic Press, New York and London (1972), p. 454.

[II-31] L.H. He, C.W. Lim: Composites Sci. and Technol. Vol. 61 (2001), p. 579.

[II-32] R. Raj, M. Ashby: Metall. Trans. Vol. 2 (1971), p. 1113.

[II-33] M.H. Hou, R.F. Davies: J. Mater. Sci. Vol. 14-10 (1979), p. 2411.

[II-34] M.H. Hou, R.F. Davies, D.E. Newbury: J. Mater. Sci. Vol. 15-8 (1980), p. 2073.

[II-35] M. Naka, J.C. Feng, J.C. Schuster: Metall. and Mater. Trans. Vol. 28 A (1997), p. 1385.

[II-36] D. Gupta, S. Weining: Acta Metall. Vol. 10 (1962), p. 292.

[II-37] F. Povolo, E.A. Bisogni: Acta Metall. Vol. 14 (1966), p. 711.

[II-38] R. Donnini, S. Kaciulis, A. Mezzi, R. Montanari and C. Testani: Surf. Interface Anal. Vol. 40 (2008), p. 277

[II-39] R. Donnini, S. Kaciulis, A. Mezzi, R. Montanari and C. Testani: Mater. Sci. ater. Forum Vol. 604 604-605 (2009), p. 331

[II-40] C. Testani and F. Ferraro: La Met : Metallurgia Italiana Vol. 8 (2008), p. 9.

 [II-41] S. Amadori, E.G. Campari, A.L. Fiorini, R. Montanari, L. Pasquini, L. Savini and E. Bonetti: Mater. Sci. Eng. A Vol. 442 (2006), p. 543

[II-42] G.K.Williamson and R.A.Smallman: Phil. Mag. Vol.1 (1956), p. : 34

Chapter 3

High Nitrogen Steel produced by Pressurized-Electroslag-Remelting

3.1 Introduction

The interchangeable between different materials is certainly an element of uncertainty that affects the stainless steel market and that certainly will determine the future developments: the steels, because of their versatility, competing in the many materials and metal alloys such as carbon steel and painted or coated, aluminium, Copper, various steels and special alloys, and especially in recent years (and much more in the future) the titanium.

The Italian market represents one of the most interesting and important markets in Europe as in the world (now consumes twice as stainless steel than ten years ago and per capita consumption is one of the largest in the world), but also the production sector is one of the interesting, both because the technological point of view has always been at the forefront is because it is held by an industrial fabric, that if in terms of mills is concentrated, processors is relatively diverse and fragmented. Regarding the division of the world market in two major families of stainless steel, 75% of products are made of austenitic steel and 25% ferritic steel, with considerable differences across countries (eg in North America and Japan on 40% of products are ferritic steel) [III-1].

Some aspects of economic and market must however be taken into account to avoid easy and optimistic predictions about the future of stainless steel:

- Market trends in the military industry;
- Evolution of the Asian market;
- Market trends in industrialized countries;
- Market development for scrap;
- Market development of nickel;
- Development of consumption;
- Situation in terms of production scene rearrangements large manufacturing companies.

Although technological innovation has always played a decisive role on the development production of stainless steels, primarily in the following fields:

- Melting process optimization;
- Continuous casting;
- Hot rolling, 'Endless' and rolling 'DRAP';
- Cold rolling, rolling speed and reduction per pass;
- Process Automation;
- Composition.

In respect to their influence on the constitution, heat treatment, and microstructure of steels carbon and nitrogen have much in common. But two advantages of N over care used to create a variety of new high nitrogen steels (HNS): dissolved nitrogen improves the corrosion resistance of stainless steels. Stable nitrides increase the strength of creep resistant steels. In contrast to carbon, nitrogen is a volatile element. Its low solubility in the steel melt calls for appropriate manufacturing procedures to overcome this drawback. The nitrogen content varies from about 0,1 to 3 wt %.

3.2 Manufacture

Elements like Mo, Mn, Cr, V, Nb, and Ti lower the activity of nitrogen in the melt and thereby raise its solubility.

Their effectiveness increases from left to right, but the solubility product in the austenite drops by about nine orders of magnitude. Therefore V, Nb and Ti are used in small quantities only, if dissolution of nitrides during heat treatment is intended. Elements like Ni, Si and C decrease the nitrogen solubility and are-if possible kept on the low side. Applying these alloying rules we end up with steels high in chromium, i.e., stainless or creep resistant grades. The resulting solidification sequence $L \rightarrow \delta \rightarrow \gamma$ implies that the low solubility in δ-ferrite is the highest to be retained (Fig. III-1). The figure also shows that in contrast to δ -ferrite the solubility of nitrogen in austenite increases during cooling. It is therefore obvious to go for martensitic Cr or CrMo-steels with an austenitic regime at hardening temperature instead of ferritic grades. The addition of Mn will suppress δ-ferrite and lead to austenitic CrMn (Mo)-steels. The high chromium

content of duplex steels offers excellent nitrogen solubility in the melt, but some of it will be lost during solidification due to ferrite formation.
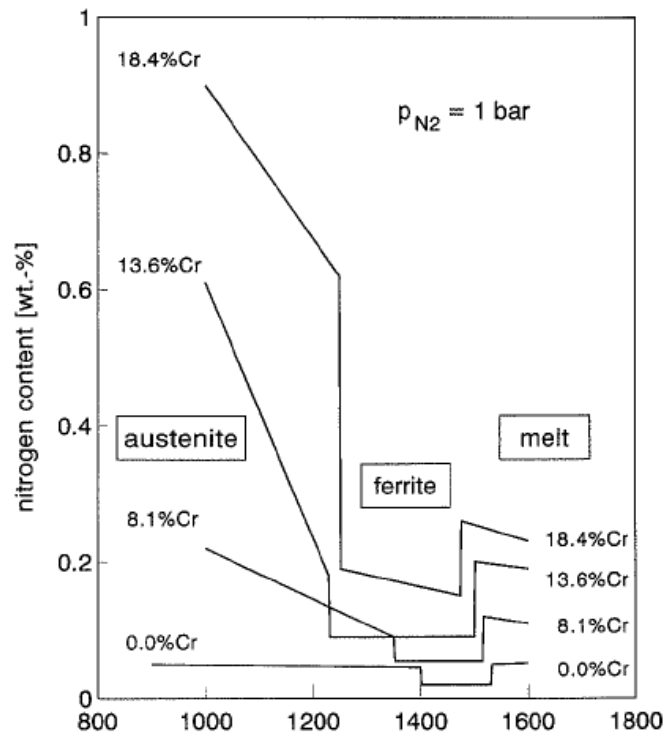
Fig. III-1 Nitrogen solubility in steel as a function of temperature and chromium content [III-22].

Applications are seen in castings like compressor discs and parts for water energy machines. Up to 0,1 % of N is added to creep resistant steels with 9 to 12 % Cr for components of steam turbines [III-2] a recent development revealed superior properties of steel Crl5Ni2MolN.18 to be used in the quenched and tempered state and to replace the respective carbon grades [III-3]. Especially for high strength application, e.g. Rp~ 800 MPa, the tempering temperature of this HNS is 30 to 40 °C higher than for the respective carbon grade which more than doubles the CVN impact toughness (Fig. III-2).
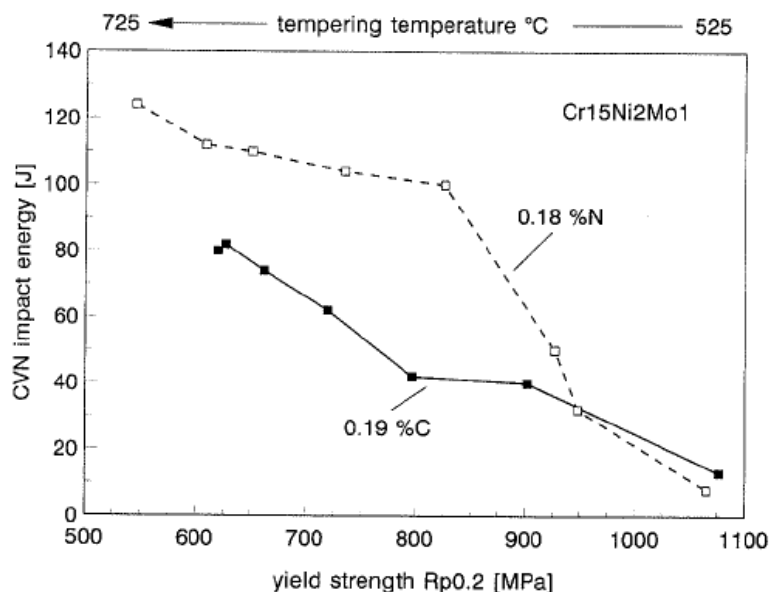
Fig. III-2 Comparison of mechanical properties quenched and tempered stainless steels containing carbon or nitro gen [III-3]

The austenitic steel Crl8Mnl8N.55 is solution annealed and quenched to a yield strength Rp>600 MPa. Forged rings of this material are cold expanded to e.g. l m in size and Rp~1250 MPa. These nonmagnetic high strength retaining rings are shrink-fitted on generator shafts to counteract the centrifugal forces of the copper wiring [III-4]. They replace steels like Mnl8Cr4C.55 which are liable to fail by stress corrosion cracking. For load-bearing structures in superconducting another non magnetic HNS is used: Cr25Nil 5Mn4N.35. It fulfils the requirement of Rp$\geq$1200 MPa and $K_{IC}\geq$ 200 MPa m$^{\frac{1}{2}}$ at 4K [III-5]. High strength ropes to support electric cables in off-shore application were made of Crl9Mn10Ni7Mo3N.5 cold drawn to Rp~2000 MPa [III-6]. The highest resistance to general pitting, and crevice corrosion is met by Cr24Nil7Mn6M04N.5. This super austenitic steel reaches Rp>420 Mpa and a pitting resistance equivalent number (PREN) of ~50 which comes close to nickel alloy 625 (NiCr22M09Nb). Applications are in Flue Gas Desulphurization (FGD), oil mining with salt water pollution, waste water handling of landfill sites, pulp and paper production [III-7].

In stainless duplex steels nitrogen is enriched in the austenite making up for the lower yield strength and CrMo content of this phase. Nitrogen may help to save nickel in stabilizing the austenite and retards the embrittling precipitation of sigma- and chi- phase. Due to their high PREN Cr26Ni7M04N.3and Cr22Mn7Ni3-M02N.4 are for example applied in the oil, off-shore, chemical and food industry as well as in FGD. However, the nitrogen content in the austenite should not exceed 0.9 % N to avoid quasi

cleavage in austenite [III-8,9]. Experiments with Cr25Mnl8N.65 showed nitrogen content of 1.11 in the austenite and brittle fracture in both phases.

The enrichment of nitrogen in the austenite during intercritical rolling or heat treating is used to increase the lower corrosion resistance of this phase. The strong work hardening of Cr17Ni1Mo1N.1 at the beginning of deformation is characteristic for dual phase steel and beneficial in sheet forming. The hard martensitic islands are expected to improve the wear resistance.

3.3 Pressure Metallurgy

By raising the nitrogen pressure p_{N2}, during melting the uptake of nitrogen is increased following from Sieverts's law which is derived for equilibrium of the nitrogen transfer reaction given in Fig. III-3. At high pressure deviations from this law arise [III-10]. Of the various processes proposed over the years pressurized-electroslag-remelting (PESR) is the one industrially employed today [III-11]. Using a Si_3N_4 slag and a pressure up to 42 bars ingots weighing up to 20 Mg are manufactured. PESR is generally combined with alloying to achieve higher nitrogen content in the melt and to attain a sufficient level of solubility in the solid state as well (see Fig. III-l).

During welding surplus nitrogen will degas and pores in the weld metal have to be avoided by a suitable welding procedure [III-12]

$$\frac{1}{2}N_2 \Rightarrow [N]$$

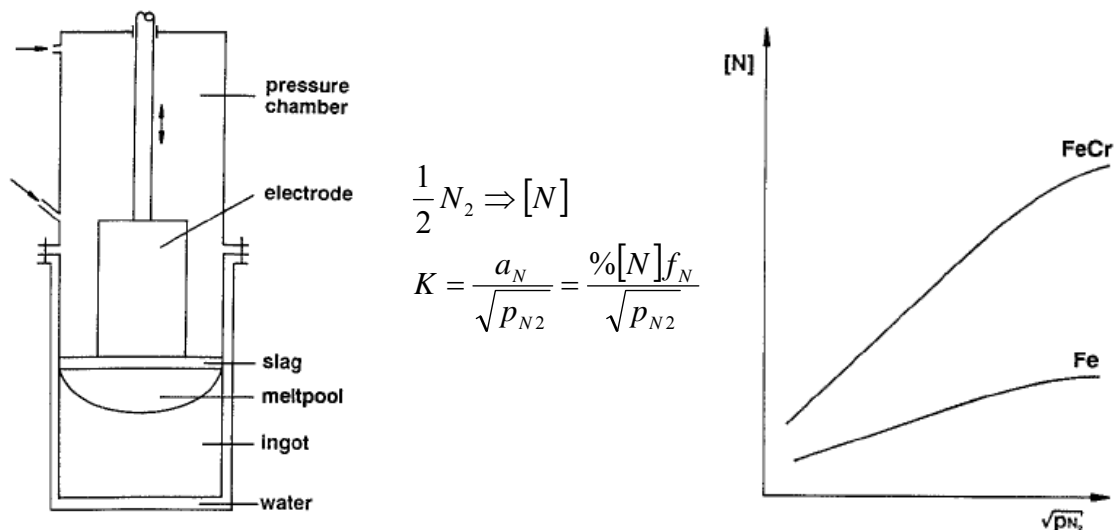$$K = \frac{a_N}{\sqrt{p_{N2}}} = \frac{\%[N]f_N}{\sqrt{p_{N2}}}$$

Fig. III-3 Raising the nitrogen content [N] in steel by melting under nitrogen pressure p_{N2} as realized in the pressurized-electro-slag-remelting process (PESR) [III-11].

The martensitic HNS Crl5MolN.3C.3 produced by PESR has to rely on some carbon to reach a hardness $\geq$ 59 HRC because p_{N2} =42 bars is-at the CrMo-content given- insufficient to raise N to ~0.60 %. Tempered in the regime of secondary hardening this new material maybe used for stainless bearings and for tools in the processing of food and aggressive polymers. Induction hardened ball screws are employed to move the flap traps of aircraft [III-13] (Fig. III-4). The pronounced secondary hardening by nitride precipitates improves the performance of hot work tool steels [III-14]. Dies made of PESR Cr5MolVlN.22C.17 for the drop forging of turbine blades produced 2.6 times more sockets in the first step and 1.3 times more blades in the final step than standard AISI H13 due to an improvement in hot strength at 600°C by ~30 %. Repair welding of HNS requires special skill, which may limit the acceptance of this tool material [III-15].
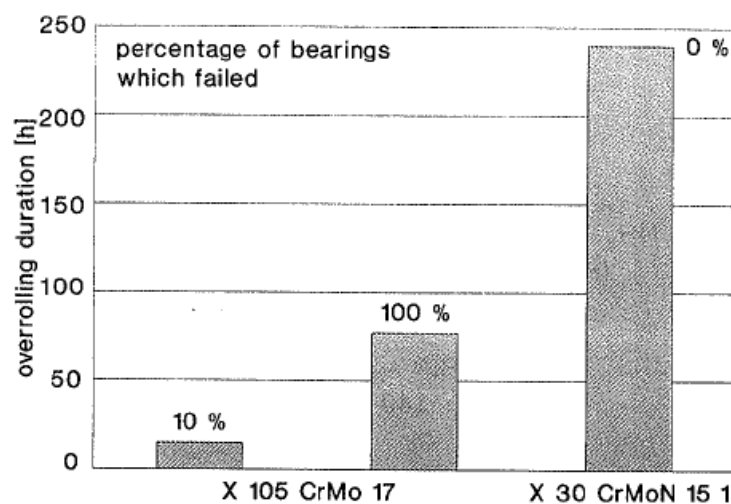
Fig. III-4 Improved life of stainless ball bearings made of new HNS Crl5MolN.3C.3 as compared to a conventional carbon grade (over-rolling test at p_0=2800 MPa and 12000 rpm with intermittent salt spraying). [III-24,25]

The effect of nitrogen on the creep resistance of chromium steels is summarized in Fig. III-5. A beneficial influence is also found in [III-16]. Long time tests with PESR steel are under way and will show if the smaller size, slower growth and more even distribution of the carbo-nitrides as compared to carbides remain effective. In case of improved long-time performance the application will probably focus on forged parts like turbine blades and rotor discs as well as on seamless tubes.

_____

In austenitic CrMn steel the increase of nitrogen by PESR allows for the addition of Mo which results in a further increase of corrosion resistance. Crl8Mnl8-M02N.85 is a Ni-free, biocompatible steel with Rp>800 MPa used for costume jewellery and dental braces [III-17]. The best combination of corrosion resistance and strength is met by the superaustenitic steel Cr24-Ni20Mn7M07N.85 [III-18].
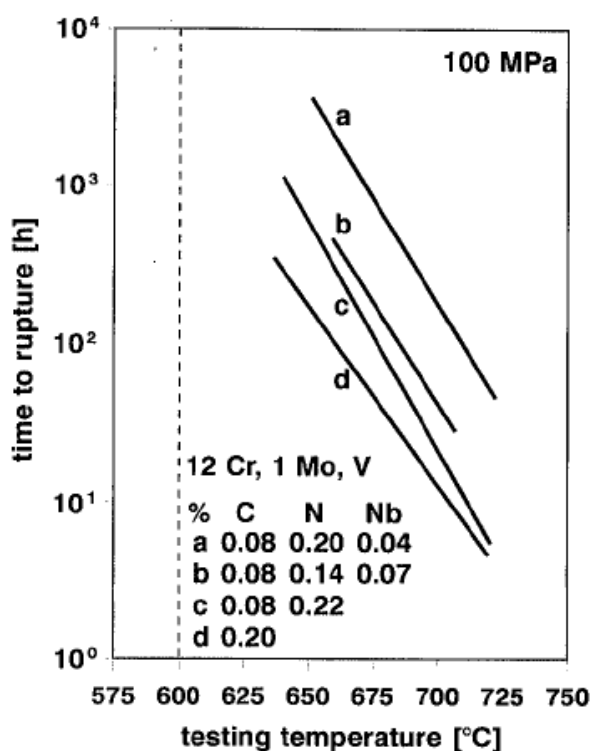
Fig. III-5 Delay of creep rupture by nitrogen as measured in iso-stress experiments up to -2000 h.

3.4 Powder Metallurgy

The solid state is best suited to introduce high nitrogen content below or even above the solubility limit resulting in the precipitation of nitrides. Because of the limited range of diffusion large cross sections are therefore compacted from nitrided powder. This manufacturing route A is described in Fig. III-6. The nitride layer formed on the powder grains is subsequently dissolved during HIP resulting in a fine dispersion of nitrides as known from PM high speed steel. In route B nitrogen is brought into the system by means of CrN powder. Its partial decomposition during HIP offers nitrogen to the steel powder within the powder mix. To avoid an embrittling net of nitrides around the steel grains the size ratio of CrN powder/steel powder has to be increased if the CrN-content

is raised. Due to the size distribution of gas-atomized powders available the route B microstructure consists of a coarse dispersion of nitrides in a steel matrix. Hot working is therefore limited [III-19].
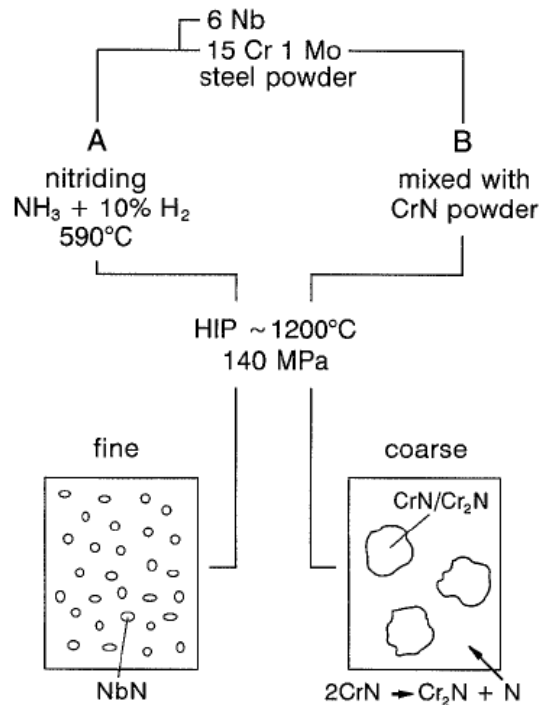
Fig. III-6 Powder metallurgical production of stainless HNS with fine or coarse nitrides embedded in a martensitic matrix [III-19,20]

About 6% Nb or V are added to route A powder to precipitate nitrides during nitrating so that Cr and Mo remain dissolved in the matrix for passivation. The nitrogen content of these steels runs up to 1.5 or 3 %, respectively. The application of the fine dispersion is seen for parts subjected to corrosion erosion like in pumps, valves and extruders.

The coarse dispersion seems best suited against grooving wear in an aggressive surrounding [III-20].

These wear resistant grades contain a high content of hard nitride particles and are therefore less sensitive o hard impurities like non-metallic inclusions and scale stemming from the PM process. Austenitic steels are less tolerant and a loss in toughness is observed in Crl8Mnl8N,8 as compared to PESR steel.

3.5 Relaxation phenomena in HNS Austenitic steel

3.5.1 Experimental

The presence of nitrogen in austenitic steels produces solid solution strengthening, increases the corrosion resistance and stabilizes the γ phase [III-21]. The difficulty of producing High Nitrogen Steel (HNS) is due to the thermodynamic limit of solubility of nitrogen in liquid or solid state. Generally, nitrogen solubility in austenitic steels does not exceed 0.4 wt % [III-22] and, under certain conditions, discontinuous precipitation of chromium nitrides occurs [III-23-24].

The examined material is an austenitic steel with high nitrogen content prepared by Pressurized Electroslag Remelting (PESR). The nominal chemical composition is: 20 Cr 2.5 Mo, 17 Mn, 0.2 C, 0.8 N, Fe to balance (wt %). Fig. III-7a) shows the original austenitic structure of the material; TEM micrograph in fig. III-7b) evidences some very small Cr_2N precipitates with size of ~ 50 nm in the N supersaturated matrix.

Internal friction (IF) and dynamic modulus measurements provide information on atomic mechanisms, which can not be otherwise investigated. For instance, Banov et al. [III-26-27] showed that the austenitic steel Fe-18 Cr-4 Mn- 0.4 N (wt %) exhibits a relaxation peak with activation energy $H = 1.47$ eV due to the re-orientation of atom pairs formed by one nitrogen atom and one substitutional atom. The same mechanism was observed in the alloy Fe-18 Cr-16 Ni-10 Mn-0.21 N (wt %) with lower nitrogen concentration, in this case two peaks have been identified with activation energies $H_1 = 1.41$ eV and $H_2 = 1.10$ eV [III-28].

This experimentation presents the results of IF and dynamic modulus measurements performed in repeated test runs on the same samples to assess the microstructural changes of the HNS austenitic steel.

During each IF cycle (heating and cooling) the samples cross a temperature range (700-800 °C) where the precipitation of chromium nitrides (Cr_2N) takes place. Therefore, repeated test runs have been performed on the same samples to investigate their microstructural evolution. For example, Fig. III-7c) shows that part of the original N supersaturated austenite (γ_S) transforms after five test runs.

_____

a)   b)

c)
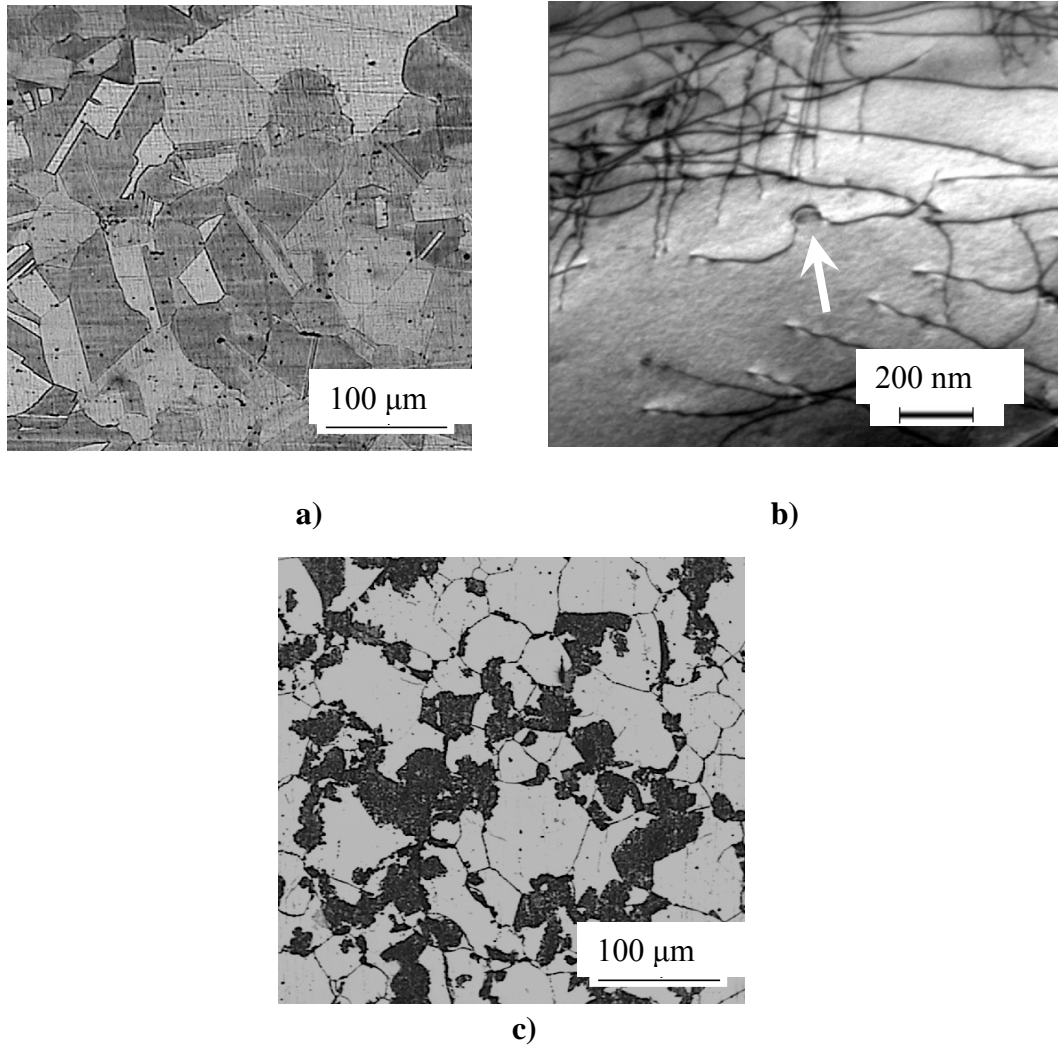
Fig. III-7- a) Structure of the steel in as-prepared condition. b) Some Cr$_2$N nano-precipitates like that indicated by the arrow are present in the as-prepared steel. c) Structure after five IF test runs.

3.5.2 Results and discussion

At room temperature the Young's modulus of the alloy is 196 GPa.

Fig. III-8 a) displays the IF spectrum of the as-prepared material; it is the superposition of an exponentially increasing background and a broad peak. If the tests are carried out with different resonance frequencies the central peak position shifts indicating that its origin is connected to relaxation processes, as confirmed by the slope change of dynamic modulus in correspondence of the peak.

Successive test runs carried out at constant frequency shift the peak to higher temperatures. For example, after five runs the central position is about 80 °C higher while the intensity of background remains unchanged (Fig. III-8 b).

The background strongly depends on defective structures, in particular grain size and dislocation density [III-30]. Since heat treatments at 800 °C for 8.28 x 10^4 s (23 hours) do not change the mean grain size and scarcely affect the dislocation density [III-25], also repeated test runs do not remarkably modify these microstructural features and, consequently, the background level.

For a relaxation peak, the temperature T_P of peak maximum depends on the resonance frequency f by the equation II-2.

From the Arrhenius plot, $ln \ \omega\tau$ vs. $1/T_P$, the activation energy H = 1.76 eV and τ_0 = 2.23 x 10^{-16} s have been obtained.
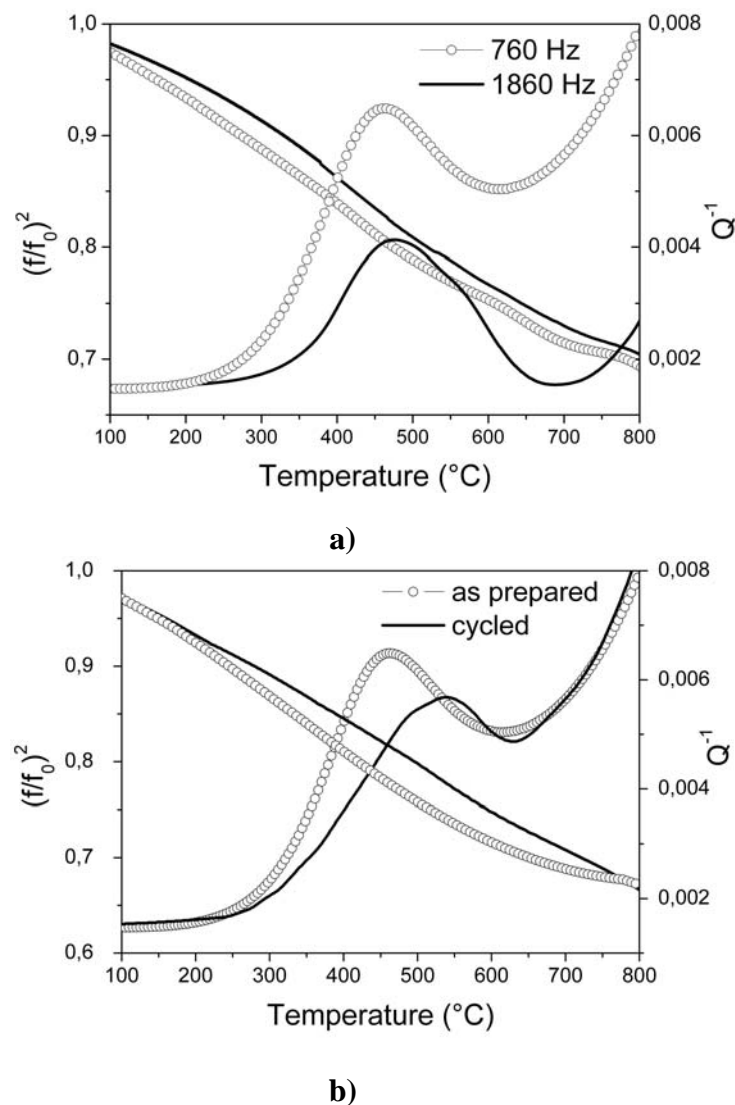

a)

b)

Fig. III-8 a) Steel in as-prepared condition: Q^{-1} and $(f/f_0)^2$ vs. T trends obtained in tests with two different resonance frequencies (760 and 1860 Hz). b) Comparison of Q^{-1} and $(f/f_0)^2$ vs. T trends of the alloy in as-prepared condition and after five IF test runs (f_0 = 760 Hz).

The steel in as-prepared condition consists of a single N supersaturated austenitic phase and the activation energy determined by us is very close to that of N diffusion in γ-iron (1.74 eV). Therefore, the IF peak can be considered as a Snoek-like peak due to the re-orientation of interstitial-substitutional (i-s) pairs. The main substitutional elements are Cr and Mn thus both of them could form the pairs with the interstitial atoms (N and C). However, the bond between Cr and N is so strong that these elements tend to form Cr_2N nanoprecipitates (see fig. III-7 b). In fact, this suggests that only Mn atoms contribute to form pairs with N and C.

On these grounds two Debye peaks due to the re-orientation of N-Mn and C-Mn pairs have been considered to fit the experimental data, after subtraction of the background. A Debye peak is described by the relationship:

$$Q^{-1}(T) = \frac{\Delta}{2} \sec h \frac{H}{R} \left(\frac{1}{T} - \frac{1}{T_P} \right)$$

(III-1)

being $\Delta/2$ the peak maximum. For the activation energy and the relaxation time of the first process, i.e. the re-orientation of N-Mn pairs, $H = 1.76$ eV and $\tau_0 = 2.23 \times 10^{-16}$ s have been taken. The values $H = 1.50$ eV and $\tau_0 = 2.69 \times 10^{-15}$ s, determined by Kê & Tsien [III-31] in the Fe-18.5Mn alloy with a Mn content similar to that of the steel examined here, have been assumed for the re-orientation of C-Mn pairs. This attempt of fitting failed because the experimental IF peak is too wide. So, we assumed that each process was characterized by single activation energy and a discrete distribution of relaxation times. This reflects variations in the environment of the species responsible for the relaxation, in particular the distribution of substitutional atoms or the interstitial clustering in the neighbourhood of the i-s pairs reorienting under the external applied stress.

For each relaxation process due to the reorientation of N-Mn and C-Mn pairs, instead of a single pre-exponential factors τ_0 a series of τ_n has been considered which according to Eq. (II-2) leads to n Debye peaks centred at different T_P. The central values τ_0 of each distribution are those used in the previous attempt of fitting, namely 2.23×10^{-16} s for N-Mn pairs and 2.69×10^{-15} s for C-Mn pairs. Positions and magnitudes of the remaining τ_n have been treated as adjustable parameters to get the best fit displayed in

fig. III-9 a). The distributions of relaxation times τ_n, normalized to the central value, are displayed in fig. III-9 b) and c).

a)

b)   **c)**
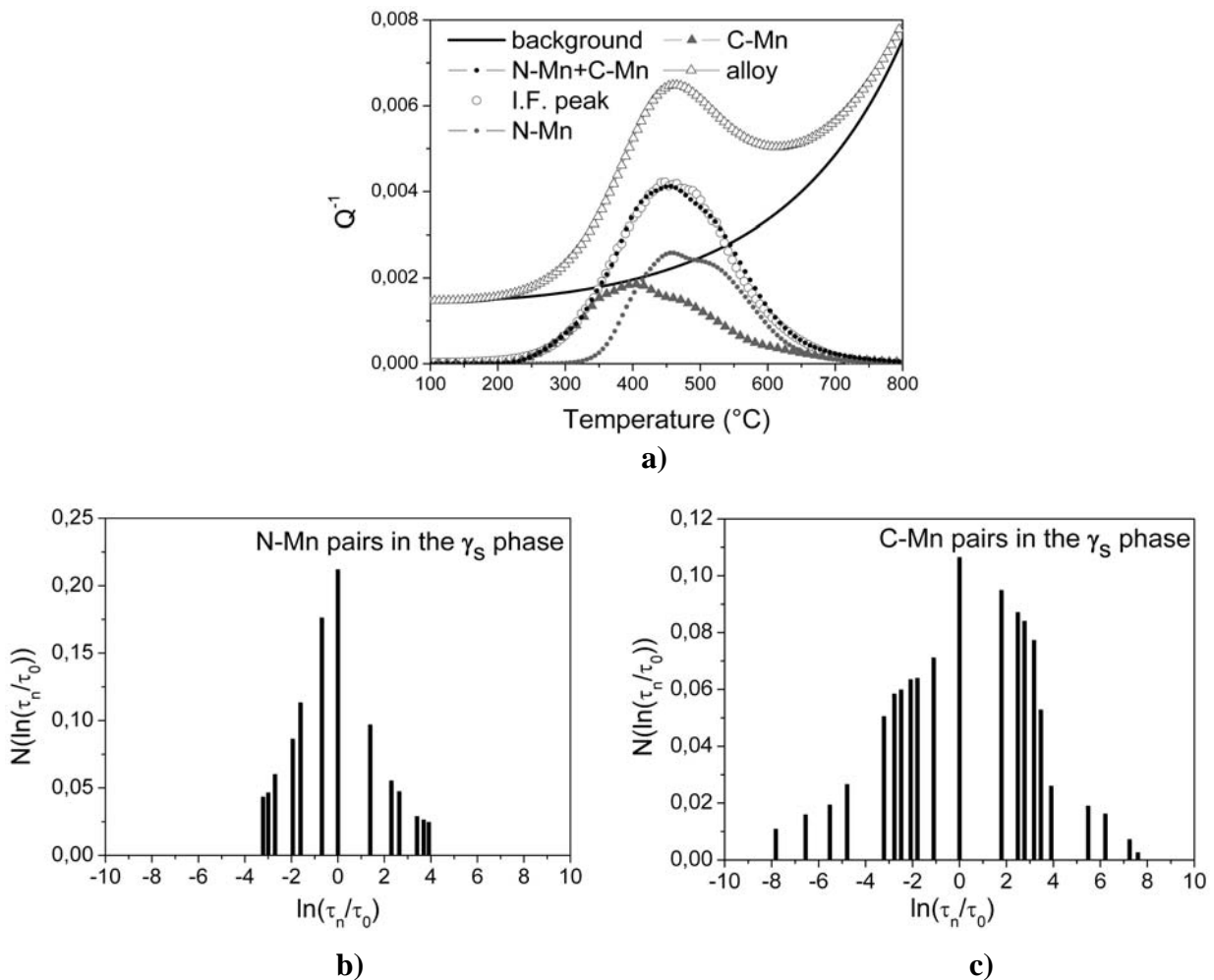
Fig. III-9 a) Fitting of the broad IF peak of as-prepared steel. b) c) Distributions of relaxation times τ_n used to get the best fit displayed in a).

In the samples already submitted to IF test runs part of the material has been transformed and its fraction depends on the number of runs. The microstructure is characterized by two austenitic phases plus Cr_2N precipitates. XRD spectra evidenced that the lattice parameter of the secondary austenite γ is smaller (3.615 Å) than that of the supersaturated austenite γ_S (3.6356 Å) [III-25]. Therefore, it is reasonable that the peak shift to higher temperatures observed in cycled samples (Fig. III-8 b) depends on a new anelastic process, namely the re-orientation of N-Mn pairs in the lattice of the phase γ which is not present in the as-prepared steel. The activation energy of this process has been determined to be 1.92 eV.

The same procedure used to get the fitting in fig. III-9 has been employed for fitting the IF spectra of cycled samples, however in this case two activation energies for N-Mn pairs in γ and γ_S have been considered. An example is given in Fig. III-10.

a)

b)
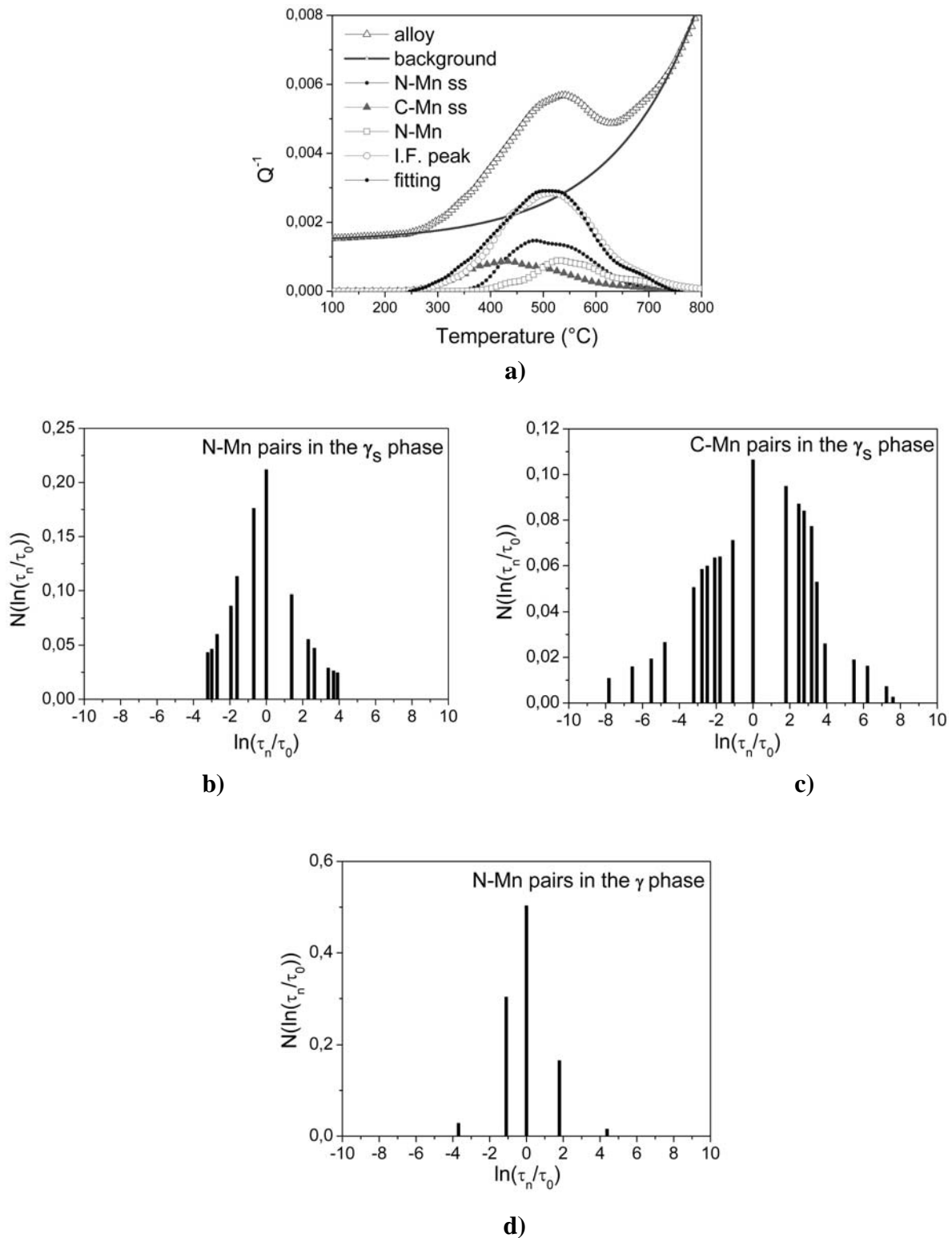

c)

d)

Fig. III-10 a) Fitting of IF data of the steel after five test runs. b) c) d) Distributions of relaxation times τ_n used to get the best fit displayed in a).

_____

REFERENCES

[III-1] H. Berns and X. Xie: Rader Rundsch., I (1992), 71.

[III-2] H. Izume: Proc. Int. Conf. Advances in Material Technology for Fossil PowerPlants, Chicago, (1987), 143.

[III-3] R, Ehrhardt: Doctoral Thesis, Ruhr-University, Bochum,(1995).

[III-4]G. Stein, J. Menzeland M. Wagner: High Nitrogen Steels (HNS '90), ed. by G. Stein and H. Witulski, Verlag Stahleisen, Dtisseldorf, (1990), 399.

[III-5] A. Nyilas, B. Obst and H. Nakajima: High Nitrogen Steels (HNS '93), ed. by V. G. Gavriljuk and V. M, Nadutov, Inst, for Metal Physics, Kiev, (1993), 339.

[III-6] V. G. Gavriljuk: Personal Communication.

[III-7] C. G. Gillessen, W. Heimannand T. L. Ladwein: Stee! Res., 62 (1992), 9, 412.

[III-8] P. J. Uggowitzer, N. Paulus and M. O. Speidel: Application of Stainless Steel 92, ed. by H. Nordberg and J. Bjdklund, ASM Int., Materials Park, Ohio, (1992), 62.

[III-9] J. Foct and H. Akdut: Scr. Metall. Mater. 29 (1993), 2, 153.

[III-10] J. C. Rawersand N. A. Gokcen: Slee! Res., 64 (1993), 2, IlO.

[III-11] J. Menzel and G. Stein: High Nitrogen Steels (HNS'93), ed, by V. G. Gavriljuk and V. M, Nadutov. Inst, for Metal Physics, Kiev, (1993). 573.

[III-12] G. Stein and F. Tr6sken: High Nitrogen Steels (HNS'90), ed. By G. Stein and H. Witulski, Verlag Stahleisen, Dusseldorf, (1990), 303

[III-13] Business Report of FAGKugelfischer GeorgSchzifer AG,(1 991), 40.

[III-14] J. Lueg: High Nitrogen Tool Steels (in German),Doctoral Thesis, Ruhr-University, Bochum,(1990).

[III-15] C. Ernst and K. Rasche: NewMaterials-Processes, Experiences for Tooling, ed, by H. Berns. M. Hofmann,L. A. Norstr6m, K. Rasche and A.-M. Schindler, Mat. Search, Andelfingen, (1992), 481.

[III-16] B. R. Anthamatten, P. J. Uggowitzer, Ch. Solenthaler and M. O. Speidel: High Nitrogen Steels (HNS'90), ed. by G. Stein and H. Witulski, Verlag Stahleisen, Dtisseldorf, (1990), 436.

[III-17] Data by Vereinigte Schmiedewerke,Essen, Germany.

[III-18] P. J. Uggowitzer, R. Magdowskiand M. O. Speidel: Proc. Int. Conf. Innovations in Stainless Steel, Florence, La Metalurgia Italiana, 86, (1993), (6-7), 347.

[III-19] G. Wang:Doctoral Thesis, Ruhr-University, Bochum,(1992).

[III-20] H. Berns and G. Wang:High Nitrogen Steels (HNS'93), ed, by V. G. Gavriljuk and V. M. Nadutov. Inst. for Metal Physics, Kiev, (1993), 415.

[III-21] P. Shankar, D. Sundararaman, S. Ranganathan: Journal of Nuclear Materials Vol. 254 (1998), p.1

[III-22] H. Hanninen, J. Romu, R. Ilola, J. Tervo, A. Laitinen: Materials Processing Technology Vol. 117 (2001), p. 424

_____

[III-23] Q.X. Dai, Z.Z. Yuan, X.M. Luo, X.N. Cheng: Materials Science and Engineering Vol. A 385 (2004), p. 445

[III-24] Heon Young Ha, HyukSang Kwon: Elettrochimica Acta Vol. 52 (2007), p. 2175

[III-25] A. Mezzi, S. Kaciulis, R. Montanari, L. Rovatti, N. Ucciardello and A. Carosi in: *Discontinuous precipitation in a high nitrogen austenitic steel*, This Conference.

[III-26] R.M. Banov, I.M. Parshorov, Ts.S. Kamenova, (1978 a) Izv Acad Metalli Vol. 3, p. 178

[III-27] R.M. Banov, I.M. Parshorov, Ts.S. Kamenova, (1978 b) Izv Acad Metalli Vol. 1, p. 126

[III-28] V.G. Gavriljuk, J. Foct, S.N. Bugaychuk and A.L. Sozinov: Scripta Mater. Vol. 37-12 (1997), p. 1889

[III-29] S. Amadori, E.G. Campari, A.L. Fiorini, R. Montanari, L. Pasquini, L. Savini, E. Bonetti: Materials Sci. & Eng. Vol. A 442 (2006), p. 543

[III-30] A.S. Nowick, B.S. Berry, in: Anelastic relaxation in crystalline materials, Academic Press, New York and London (1972), p. 454

[III-31] T.S. Ke, C.T. Tsien, Sci. Sinica Vol. 5 (1956), p. 625

_____

Chapter 4

Internal friction peak due to nitrogen in tungsten

4.1 Introduction

Tungsten is a promising armour material for plasma facing components of nuclear fusion reactors because of its low sputter rate and favourable thermo-mechanical properties (high melting point and good thermal conductivity) [IV-1].

Previous works have demonstrated the feasibility of 5 mm thick W coatings on CuCrZr substrates and their capability to withstand heat fluxes up to 5 MW/m^2 in condition relevant for fusion reactor plasma facing components [IV-2]. Morphology, structure and integrity of the manufactured coatings and their mechanical properties and impurity content have been extensively investigated [IV-3-4].

A complete physical-chemical characterization of plasma facing materials is of fundamental importance because they are subjected to simultaneous high thermal and ionic fluxes. This work reports some results obtained in an experimental campaign for investigating the microstructural characteristics and properties of tungsten samples prepared by different companies. The attention is focused on the elastic and anelastic behaviour which has been investigated by Mechanical Spectrometry experiments, i.e. internal friction (IF) and dynamic modulus measurements carried out in the temperature range 300-1123 K.

4.2 Material and experimental

The examined material had the following chemical composition [IV-5]: Al 0.0015, C 0.003, O 0.002, N 0.0005, W to balance (wt %).

After mechanical polishing the material has been etched in boiling H_2O_2 (3%), then examined by optical microscopy.

XRD measurements in the 2Θ range 30 - 110 degrees have been carried out by using the Co Kα radiation (λ = 0.179 nm) in step scanning mode with steps of 0.05 (2Θ degrees)

_____

and counting time of 2 s per step. High precision peak profiles were measured with steps of 0.005 (2Θ degrees) and counting time of 20 s per step.

IF and dynamic modulus measurements have been carried out on bar-shaped samples (23.9 mm x 4 mm x 0.57 mm). The VRA 1604 apparatus employed in the experiments was described in detail in [IV-6]. Q^{-1} values have been determined from logarithmic decay of flexural vibrations. The resonance frequency f was in the range of kilohertz. The samples have been heated from room temperature to 1123 K with heating rate of 1.7×10^{-2} Ks^{-1}. The strain amplitude was kept lower than 1×10^{-5}.

4.3 Results and discussion

The optical micrograph in fig. IV-1 shows the tungsten structure; the mean grain size is about 25 μm and a residual porosity is observed. The density determined by direct measurements was found to be 18.14 g cm^{-3}, i.e. 94% of that of bulk material (19.35 g cm^{-3}).
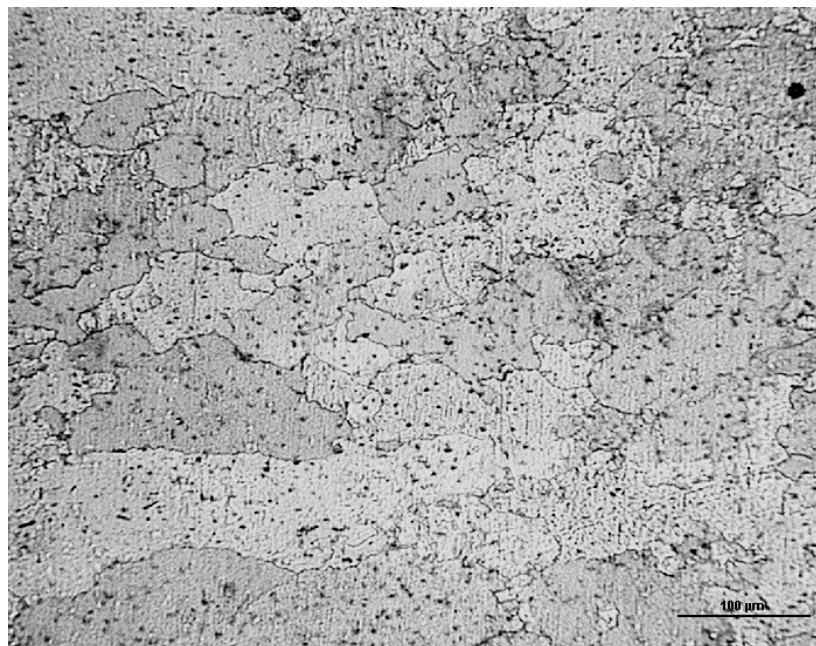
Fig. IV-1- Structure of the tungsten.

The XRD spectrum is displayed in fig. IV-2, and the relative intensities of the main XRD peaks are reported in Table IV-1.
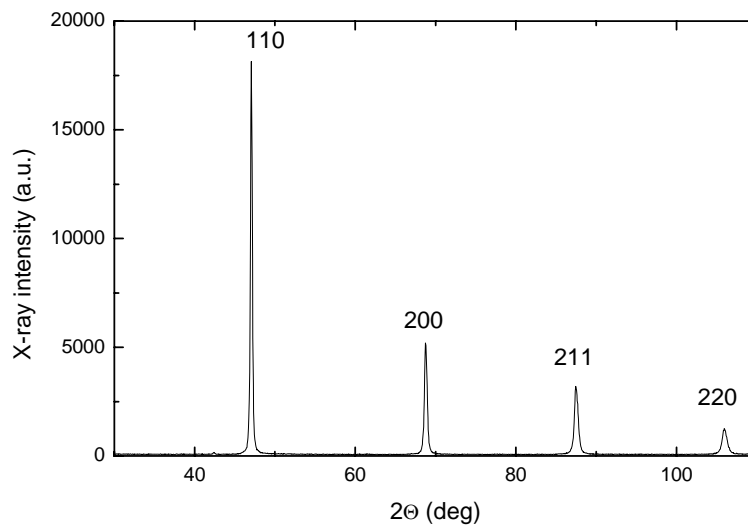
Fig. IV-2- XRD spectrum of the material.

{h k l}	{110}	{200}	{211}	{220}
(JCPDS-ICDD 4-806).	100	15	23	8
W	100	30	15	7

Table IV-1- Comparison between the relative intensities of the main XRD peaks of W.

From the comparison with the relative intensities of tungsten with randomly oriented grains (JCPDS-ICDD 4-806 file) the examined material exhibits a weak {100} texture. From the precision peak positions the lattice parameter $a = 0.320$ nm has been determined.

_____

Fig. IV-3 shows the trends of Q^{-1} and E vs. T.
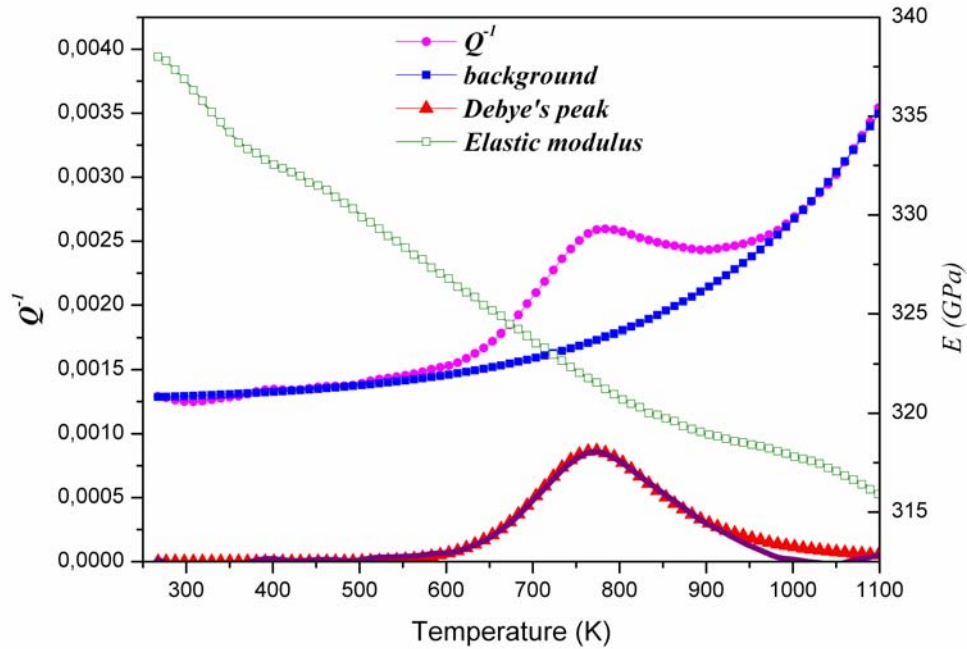
Fig. IV-3- Trends of Q^{-1} and E vs. T

The elastic modulus at room temperature is 338 GPa, a value consistent with the measured density. The relationship between the elastic moduli of the same material with (E) and without (E_0) porosity is given by:

$$E = E_0 \left(1 - \frac{p}{p_c} \right)^f \qquad\qquad (IV\text{-}1)$$

being p the porosity, p_c the critical porosity value ($\sim 40\%$) where Young's modulus becomes zero, f a parameter depending on grain morphology and pore geometry [IV-7]. Substituting $E_0 = 400$ GPa [IV-8] in eq. (IV-1) and taking $f = 1$ [IV-9] the porosity p results to be 6.2%, a value very close to the experimental one (6%).

The Q^{-1} curve exhibits a peak centred at 778 K superimposed to an exponentially increasing background, in correspondence of the peak the modulus exhibits a slope change. The height of the peak is 8.58 x 10^{-4}.

_____

Fig. IV-4 a) displays normalized IF peaks obtained in experiments performed with different resonance frequency: the peak position clearly depends on the frequency (Eq. II-2). This indicates that the Q^{-1} peak is a relaxation peak.
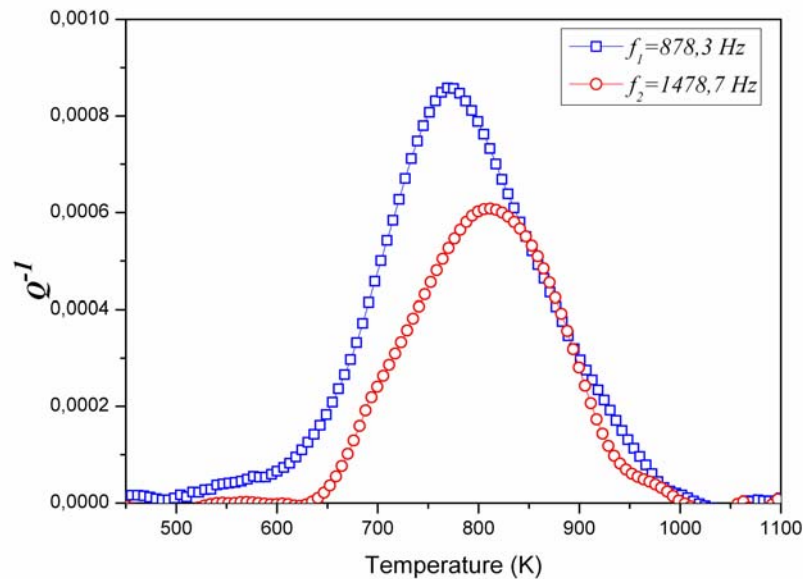
Fig. IV-4- Normalized IF peaks obtained in experiments performed with different resonance frequencies.

The activation energy $H = 75.15$ kJ mol^{-1} and the pre-exponential frequenct factor $\tau_0 = 1.49$ x 10^{-9} s have been obtained. As shown in fig. IV-3, the experimental peak is fitted very well by the equation II-1 describing a Debye peak:

The peak characteristics have been compared with IF literature data (e.g. the review book of Blanter et al. [IV-10]) but no correspondence has been found. Therefore, it seems that such peak has been never observed before by other investigators.

To identify the physical process responsible for the relaxation peak, it has been considered that the activation energy is very close to that (0.75 eV = 72.36 kJ mol^{-1}) found by Bodnar et al. [IV-11] for nitrogen diffusion in tungsten by bulk mechanism. The diffusion parameters have been determined from the dynamics of surface nitrogen concentration after ion-implantation.

It is well known that the activation energy for interstitial solute migration corresponds to the activation energy of Snoek relaxation due to the alternate jumping of interstitial

_____

atoms from neighbouring octahedral sites in bcc metals under an external oscillating stress [IV-12].

Furthermore, in bcc metals with different interstitial solute atoms the pre-exponential frequency factor τ_0 for the Snoek relaxation is rather constant in the range 2.77-6.66 x 10^{-15} s [IV-12].

On these grounds the IF peak evidenced by present experiments can be explained as due to the Snoek relaxation of nitrogen in tungsten lattice.

It is noteworthy to recall that inconsistent data are reported in literature about the diffusion of nitrogen in tungsten (see for example ref. [IV-13-15]). Such inconsistence of results mainly depends on the quality of the examined materials. On the contrary of other experiments [IV-13-15], the tests of Bodnar et al. have been carried out on single crystals where the grain boundary diffusion does not so strongly affect the results at relatively low temperatures.

4.4 Conclusions

Tungsten has been investigated by IF and dynamic modulus measurements in the temperature range from room temperature to 1123 K.

The elastic modulus at room temperature is 338 GPa, a value consistent with the measured density (18.14 g cm^{-3}), i.e. 94% of that of bulk material.

The IF spectrum exhibits a relaxation peak (H = 75.15 kJ mol^{-1} and τ_0 = 1.49 x 10^{-9} s) superimposed to an exponentially increasing background. The Q^{-1} peak is a single Debye peak. Being its activation energy very close to the diffusion energy of nitrogen in tungsten lattice independently found by Bodnar et al. [IV-18] it is believed to be a Snoek peak due to nitrogen in the tungsten lattice.

References

[IV-1] H. Bolt, V. Barabash, W. Krauss, J. Linke, R. Neu, S. Suzuki, Nyoshida, Journal of Nuclear Materials 329-333 (2004) 66-73.

[IV-2] B. Riccardi, A. Pizzuto, A. Orsini, S. Libera, E. Visca, L. Bertamini, F. Casadei, E. Severini, R. Montanari, R. Vesprini, P. Varone, G. Filacchioni, N. Litunovsky, Fusion Technology 1 (1998) 223.

[IV-3] R. Montanari, B. Riccardi, R. Volterri, L. Bertamini, Materials Letters, 52 (2002) 100.

[IV-4] B. Riccardi, R. Montanari, M. Casadei, G. Costanza, G. Filacchioni, A. Moriani, Journal of Nuclear Materials 352 (2006) 29.

[IV-5] Plansee, Technical Report.

[IV-6] S. Amadori, E.G. Campari, A.L. Fiorini, R. Montanari, L. Pasquini, L. Savini, E. Bonetti, Materials Science and Engineering A, 442 (2006) 543.

[IV-7] K. K. Phani, S. K. Niyogi, Journal of Material Science, 22 (1987) 257.

[IV-8] *www.matweb.com*

[IV-9] D.C. Lam , F.F. Lange, A.G. Evans, Journal of American Ceramic Society 77 (1994) 2113.

[IV-10] M.S. Blanter, I.S. Golovin, H. Neuhauser, H.R. Sinning, Internal Friction in Metallic Materials-A Handbook, Springer Berlin, 2007, p.261.

[IV-11] O.B. Bodnar, I.M. Aristova, A.A. Mazilkin, L.N. Pronina, A.N. Chalka, P.Yu. Popov, Physics of the Solid State 48-1 (2006) 10-14.

[IV-12] A.S. Nowick, B.S. Berry, Anelastic Relaxation in Crystalline Solids, Academic Press, New York and London, 1972, p. 225.

[IV-13] R. Frauenfelder, J. Chem. Phys. 48 (1968) 3966.

[IV-14] R.L. Wagner, Metallurgical Transaction 1 (1970) 3365.

[IV-15] H. Jehn, E. Fromm, J. Less Common Metals, 21 (1970) 333.

[IV-16] J. Keinonen, J. Räisänen, A. Anttila, Applied Physics A 35 (1984) 227-232.

Chapter 5

Nickel Based Superalloys

5.1 Introduction

A superalloy is a metallic alloy which can be used at high temperatures, often in excess of 0.7 of the absolute melting temperature. Creep and oxidation resistance are the prime design criteria. Superalloys can be based on iron, cobalt or nickel, the latter being best suited for aeroengine applications.

The essential solutes in nickel based superalloys are aluminium and/or titanium, with a total concentration which is typically less than 10 atomic percent. This generates a two-phase equilibrium microstructure, consisting of gamma (γ) and gamma-prime (γ'). It is the γ' which is largely responsible for the elevated-temperature strength of the material and its incredible resistance to creep deformation. The amount of γ' depends on the chemical composition and temperature, as illustrated in the ternary phase diagrams reported in Figure V-1.
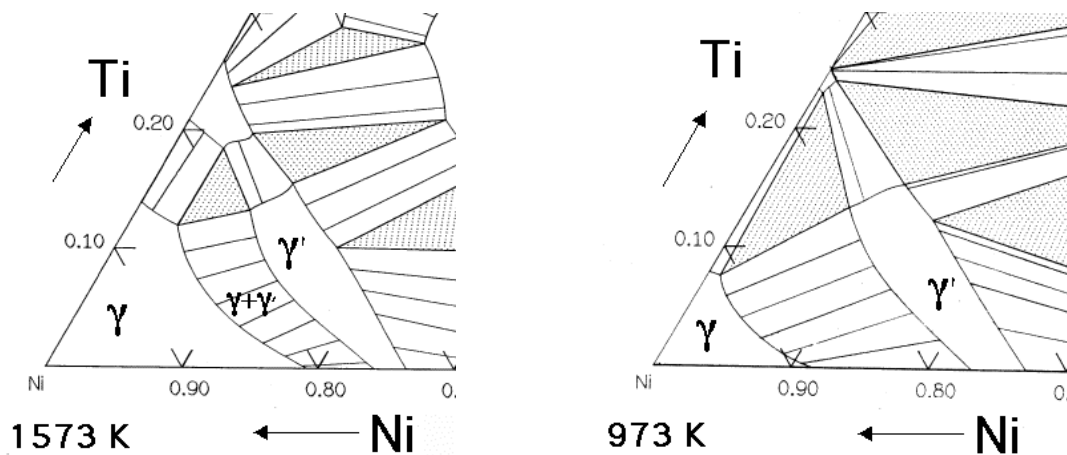

Fig. V-1 nickel based superalloy ternary phase diagram

The Ni-Al-Ti ternary phase diagrams show the γ and γ' phase field. For a given chemical composition, the fraction of γ' decreases with temperature increase. This phenomenon is used in order to dissolve the γ' at a sufficiently high temperature

_____

(a solution treatment) followed by ageing at a lower temperature in order to generate a uniform and fine dispersion of strengthening precipitates.

The γ-phase (Fig. V-2) is a solid solution with a cubic-face-centred lattice and a random distribution of the different species of atoms.

By contrast, γ' has a cubic lattice in which the nickel atoms are at the face-centres and the aluminium or titanium atoms at the cube corners. This atomic arrangement has the chemical formula $Ni_3(Al,Ti)$. However, as can be seen from the (γ+γ')/γ' phase boundary on the ternary sections of the Ni, Al, Ti phase diagram, the phase is not strictly stoichiometric. May exist an excess of vacancies on one of the sub lattices which leads to deviations from stoichiometry; alternatively, some of the nickel atoms might occupy the Al sites and vice-versa. In addition to aluminium and titanium, niobium, hafnium and tantalum partition preferentially into γ'.

a)   b)
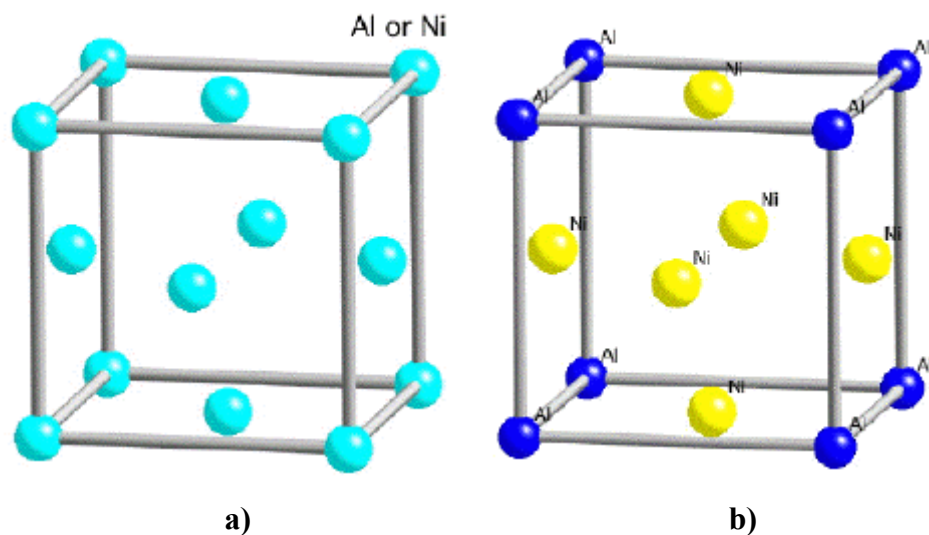
Fig. V-2 a) Crystal structure of γ; b) Crystal structure of γ'.

The γ phase forms the matrix in which the γ' precipitates. Since both the phases have a cubic lattice with similar lattice parameters, the γ' precipitates in a cube-cube orientation relationship with the γ. This means that its cell edges are exactly parallel to corresponding edges of the γ phase. Furthermore, because their lattice parameters are similar, the γ' is coherent with the γ when the precipitate size is small. Dislocations in the γ nevertheless find it difficult to penetrate γ', partly because the γ' is an atomically ordered phase. The order interferes with dislocation motion and hence strengthens the alloy.

The small misfit between the γ and γ' lattices is important for two reasons. Firstly, when combined with the cube-cube orientation relationship, it ensures a low γ/γ' interfacial energy. The ordinary mechanism of precipitate coarsening is driven entirely by the minimisation of total interfacial energy. A coherent or semi-coherent interface therefore makes the microstructure stable, a property which is useful for elevated temperature applications.

The magnitude and sign of the misfit also influences the development of microstructure under the influence of a stress at elevated temperatures. The misfit is said to be positive when the γ' has a larger lattice parameter than γ. The misfit can be controlled by altering the chemical composition, particularly the aluminium to titanium ratio. A negative misfit stimulates the formation of rafts of γ', essentially layers of the phase in a direction normal to the applied stress. This can help reduce the creep rate if the mechanism involves the climb of dislocations across the precipitate rafts.

The transmission electron micrographs (Fig. V-3) shown below illustrate the large fraction of γ', typically in excess of 0.6, in turbine blades designed for aeroengines, where the metal experiences temperatures in excess of 1000°C. Only a small fraction (0.2) of γ' is needed when the alloy is designed for service at relatively low temperatures (750°C) and where welding is used for fabrication.

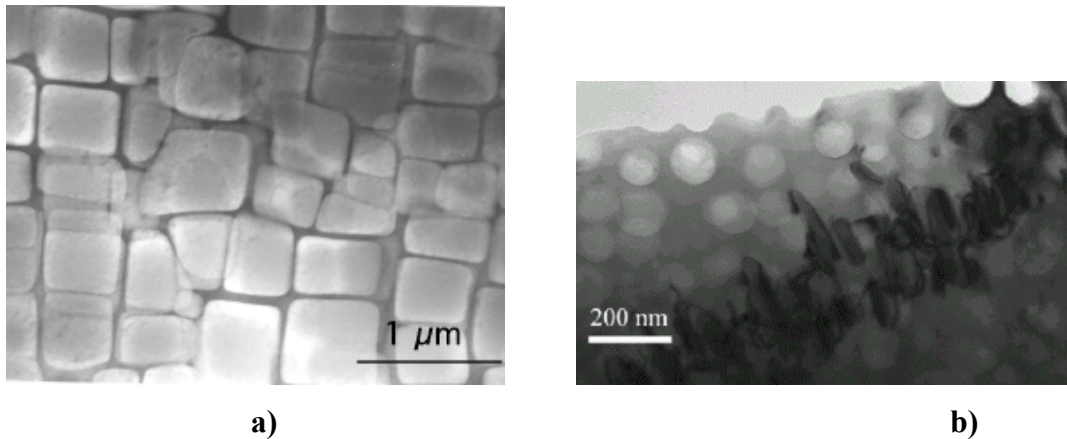a)   b)

Fig. V-3 a) Transmission electron micrograph showing a large fraction of cuboidal γ' particles in a γ matrix. b)Transmission electron micrograph showing a small fraction of spheroidal γ' prime particles in a γ matrix.

5.2 Strength versus Temperature

The strength of most metals decreases as the temperature is increased, because assistance from thermal activation makes it easier for dislocations to move. However, nickel based superalloys containing γ', which essentially is an intermetallic compound based on the formula $Ni_3(Al,Ti)$, are particularly resistant to temperature.

Ordinary slip in both γ and γ' occurs on the {111}<110>. If slip was confined to these planes at all temperatures then the strength would decrease as the temperature is raised. However, there is a tendency for dislocations in γ' to cross-slip on to the {100} planes where they have a lower anti-phase domain boundary energy. This is because the energy decreases with temperature. Situations arise where the extended dislocation is then partly on the close-packed plane and partly on the cube plane. Such a dislocation becomes locked, leading to an increase in strength. The strength only decreases beyond about 600°C whence the thermal activation is sufficiently violent to allow the dislocations to overcome the obstacles.

To summarise, it is the presence of γ' which is responsible for the fact that the strength of nickel based superalloys is relatively insensitive to temperature (Fig. V-4).
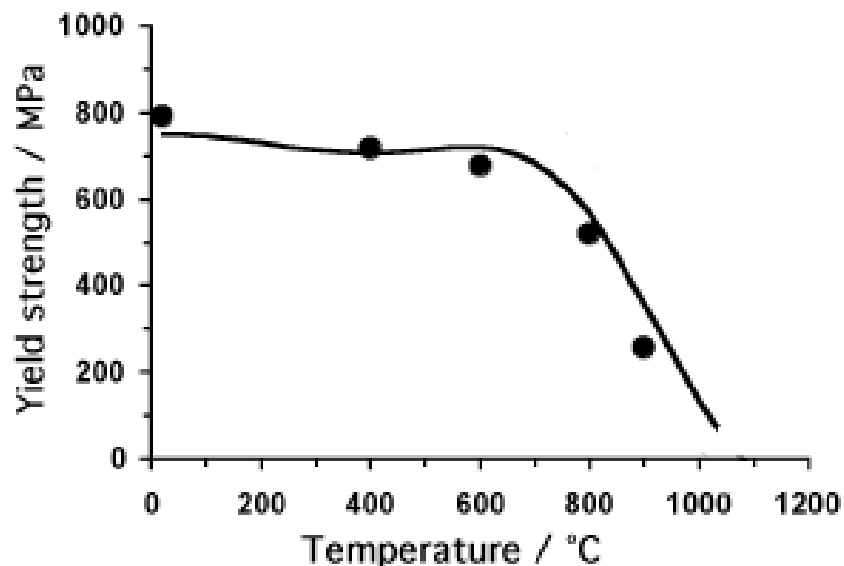

Fig. V-4 Trend of yield stress of superalloy, containing 20% of γ'. The points are measured and the curve is a theoretical prediction. Notice how the strength is at first insensitive to temperature.

When greater strength is required at lower temperatures (e.g. turbine discs), alloys can be strengthened using another phase known as γ" (Fig. V-5).
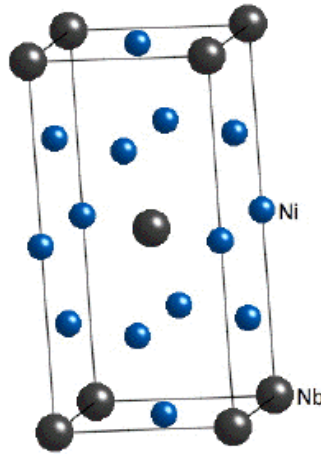
Fig. V-5 Crystal structure of γ"

This phase occurs in nickel superalloys with significant additions of niobium, the crystal structure of γ" is based on a body-centred tetragonal lattice with an ordered arrangement of nickel and niobium atoms. Strengthening occurs therefore by coherency hardening and order hardening mechanism.

5.3 Alloy Compositions

Commercial superalloys contain more than just Ni, Al and Ti. Chromium and aluminium are essential for oxidation resistance small quantities of yttrium help the oxide scale to cohere to the substrate. Polycrystalline superalloys contain grain boundary strengthening elements such as boron and zirconium, which segregate to the boundaries. The resulting reduction in grain boundary energy is associated with better creep strength and ductility when the mechanism of failure involves grain de-cohesion. There are also the carbide formers (C, Cr, Mo, W, C, Nb, Ta, Ti and Hf). The carbides tend to precipitate at grain boundaries and hence reduce the tendency for grain boundary sliding.

Elements such as cobalt, iron, chromium, niobium, tantalum, molybdenum, tungsten, vanadium, titanium and aluminium are also solid-solution strengtheners, both in γ and γ' (Fig. V-6).
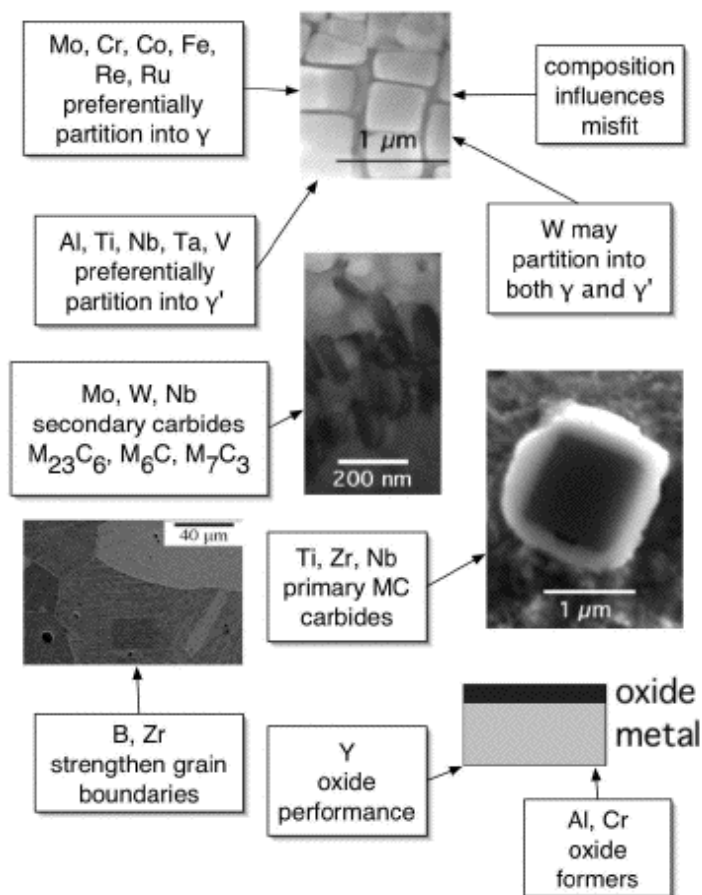
Alloy		Cr	Co	Mo	W	Ta	Nb	Al	Ti	Fe	C	B	Zr	Re	Hf	Others
Astroloy	PM	14.9	17.2	5.1				4	3.5		0.03		0.04			
CMSX2	SX	8	4.6	0.6	7.9	5.8		5.6	0.9							
CMSX4	SX	5.7	11	0.42	5.2	5.6		5.2	0.74					3	0.1	
CMSX6	SX	9.8	5	3		2.1		4.8	4.7							
CMSX10	SX	2	3	0.4	5	8	0.1	5.7	0.2					6	0.03	
FT750DC	wrought	20			3.5			2.3	2.1	5	0.07	0.005				0.4 Si
Hastelloy X	wrought	22	1.5	9	6					18.5	0.1					0.5Mn, 0.5Si
Hastelloy S	wrought	15.5		14.5				0.2		1	0.02	0.009				0.02 La
Inconel 600	wrought	15.8								7.2	0.04					0.2Mn, 0.2 Si
Inconel 718	wrought	18.6		3.1			5	0.4	0.9	18.5	0.04					0.2Mn, 0.3Si
MA758	MA/ODS	30						0.3			0.05					0.6 yttria
MA760	MA/ODS	19.5			3.4			6	1.2		0.06					1.0 yttria
MA6000	MA/ODS	15			3.9			4.5	2.3	1.5	0.06					1.1 yttria
MAR-M200	cast	9	10		12		1	5	2		0.15	0.015	0.05			
Nimonic 80A	wrought	19.5	1.1					1.3	2.5			0.06				
Nimonic 105	wrought	14.5	20	5				1.2	4.5			0.2				
PM1000	MA/ODS	20						0.3	0.5	3						0.6 yttria
Rene N5	SX	7	8	2	5	7		6.2						3	0.2	
Rene N6	SX	4.2	12.5	1.4	6	7.2		5.75						5	0.15	
Rene 41	wrought	19	11	10				1.5	3.1		0.09	0.05				
RR2000	SX	10	15	3				0.05	4							1 V
SRR99	SX	8.5	5		9.5	2.8		5.5	2.2							
TMS 63	SX	6.9		7.5		8.4		5.8	0							
Udimet 500	wrought	18	18.5	4				2.9	2.9		0.08	0.006	0.05			
Udimet 700	wrought	15	18.5	5.2				4.3	3.5		0.08	0.03				
Waspaloy	wrought	19.5	13.5	4.3				1.3	3		0.08	0.006	0.06			

Fig. V-6 Alloying element effects (wt %) in nickel based superalloys. MA/ODS ≡ mechanically alloyed, oxide dispersion-strengthened. PM ≡ powder metallurgical origin, SX ≡ single crystal.

There are, naturally, limits to the concentrations that can be added without inducing precipitation. It is particularly important to avoid certain embrittling phases such as Laves and Sigma. There are no simple rules governing the critical concentrations; it is best to calculate or measure the appropriate part of a phase diagram.

The single-crystal superalloys are often classified into first, second and third generation alloys. The second and third generations contain about 3 wt % and 6 wt % of rhenium respectively. Rhenium is a very expensive addition but leads to an improvement in the creep strength. It is argued that some of the enhanced resistance to creep comes from the promotion of rafting by rhenium, which partitions into the γ and makes the lattice misfit more negative. Atomic resolution experiments have shown that the Re occurs as clusters in the γ phase. It is also claimed that rhenium reduces the overall diffusion rate in nickel based superalloys.

The properties of superalloys deteriorate if certain phases known as the topologically close-packed (TCP) phases precipitate. In these phases, some of the atoms are arranged as in nickel, where the close-packed planes are stacked in the sequence ...ABCABC... However, although this sequence is maintained in the TCP phases, the atoms are not close-packed, hence the adjective 'topologically'. TCP phases include σ and μ. Such phases are not only intrinsically brittle but their precipitation reduce, in the matrix, the concentration of elements which are added for different purposes. The addition of rhenium promotes TCP formation, so alloys containing these solutes must have their Cr, Co, W or Mo concentrations reduced to compensate. It is generally not practical to remove all these elements, but the chromium concentration in the new generation superalloys is much reduced. Chromium does protect against oxidation, but oxidation can also be prevented by coating the blades.

5.4 Applications of nickel based superalloys

A major use of nickel based superalloys is in the manufacture of aero engine turbine blades (Fig. V-7).

a)   b)   c)

d)
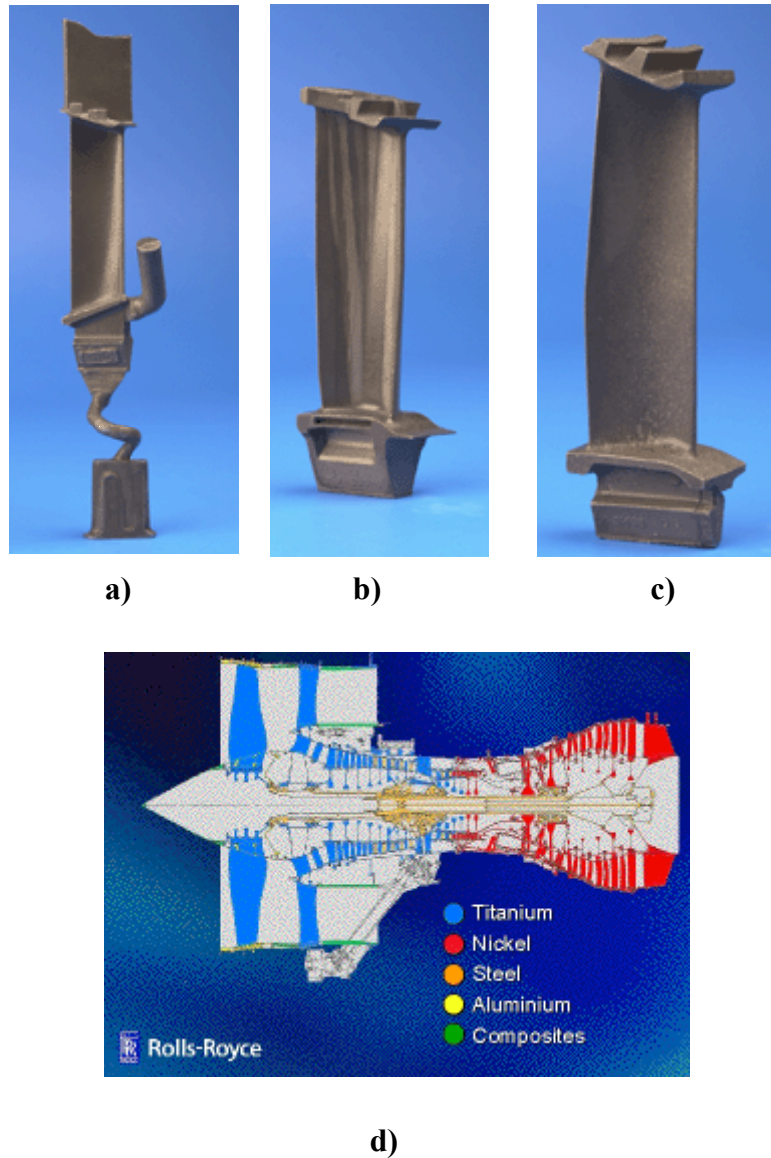
Fig. V-7 a) Single crystal, b) Directionally solidified columnar grains, c) Equiaxed polycrystalline, d) Engine materials

A single-crystal blade is free from γ/γ grain boundaries. Boundaries are easy diffusion paths and therefore reduce the resistance of the material to creep deformation. The directionally solidified columnar grain structure has many γ grains, but the boundaries are mostly parallel to the major stress axis; the performance of such blades is not as

good as the single-crystal blades. However, they are much better than the blade with the equiaxed grain structure which has the worst creep life.

One big advantage of the single-crystal alloys over conventionally cast polycrystalline superalloys is that many of the grain boundaries strengthening solutes are removed. This results in an increase in the incipient melting temperature (i.e., localised melting due to chemical segregation). The single-crystal alloys can therefore be heat treated to at temperatures in the range 1240-1330°C, allowing the dissolution of coarse γ' which is a residual of the solidification process. Subsequent heat treatment can therefore be used to achieve a controlled and fine-scale precipitation of γ'. The primary reason why the first generation of single-crystal superalloys could be used at higher temperatures than the directionally solidified ones, was because of the ability to heat-treat the alloys at a higher temperature rather than any advantage due to the removal of grain boundaries. A higher heat-treatment temperature allows all the γ' to be taken into solution and then by aging, to precipitate in a finer form.

Superalloy blades are used in aero engines and gas turbines in regions where the temperature is in excess of about 400°C, with titanium blades in the colder regions. This is because there is a danger of titanium igniting in special circumstances if its temperature exceeds 400°C.

Turbine blades are attached to a disc (Fig. V-8) which in turn is connected to the turbine shaft. The properties required for an aero engine discs are different from that of a turbine, because the metal experiences a lower temperature. The discs must resist fracture by fatigue. Discs are usually cast and then forged into shape. They are polycrystalline.
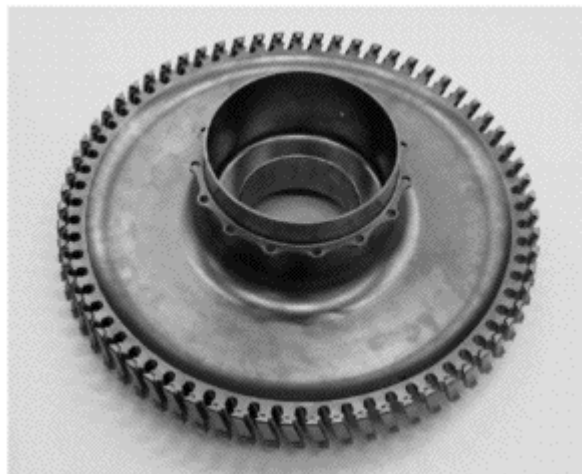

Fig. V-8 Powder metallurgical aero engine disc (Rolls-Royce).

One difficulty is that cast alloys have a large columnar grain structure and contain significant chemical segregation; the latter is not completely eliminated in the final product. This can lead to scatter in mechanical properties. One way to overcome this is to begin with fine, clean powder which is then consolidated. The powder is made by atomisation in an inert gas; the extent of chemical segregation cannot exceed the size of the powder. After atomisation, some discs are made from powder which is hot-isostatically pressed, extruded and then forged into the required shape. The process is difficult because of the need to avoid undesired particles introduced, for example, from the refractories used in the atomisation process, or impurities picked up during solidification. Such particles initiate fatigue; the failure of an aeroengine turbine disc can be catastrophic.

5.5 Dislocation rearrangement and damping phenomena for PWA 1483 SX and IN792DS superalloy.

5.5.1 Introduction

Ni-based superalloys with biphasic structure ($\gamma + \gamma$') are usually applied in hot parts of gas and aeronautical turbines. For such applications the mechanical stability is of the utmost importance. Anelastic behaviour of these materials has been extendedly investigated by different techniques [V-1-7].

Hermann et al. [V-2] have shown that the CMSX-4 alloy has two relaxation peaks: activation enthalpy $\Delta H \cong 3.10$ eV and relaxation time $\tau_0 \sim 10^{-16}$ (peak 1), $\Delta H \cong 2.7$ eV and $\tau_0 \sim 10^{-13}$ (peak 2). From the comparison of ΔH values of the two peaks with the diffusion energies of Ni and Al obtained in a Ni_3Al single-crystal by diffusion experiments of Frank et al. [V-8], peak 2 was attributed to the diffusion of Ni in the sub-lattice of Ni. The peak 1, with higher activation enthalpy, was ascribed to the diffusion of Al which jumps in near sites of Al or Ni forming anti-site defects.

A peak with characteristics (ΔH and τ_0) close to those of peak 1 [V-2] has been observed by other investigators [V-1,3,4] who given different interpretations. The peak was attributed by Gadaud et al. [V-1] to Ni diffusion whereas Mourisco et al. [V-3-4] considered it a Zener peak.

In alloys with a periodic structure of the ordered phase γ' Gadaud and Rivière [V-9] found a peak at 10 Hz, independent on the test temperature, due to thermoplastic relaxation induced by a chemical gradient.

This work presents the results of internal friction (IF) and dynamic modulus measurements performed in repeated test runs on the same samples to assess the microstructural stability of single-crystal PWA 1483 and directional solidified IN792DS superalloys in solubilized condition. The experimental conditions were suitably chosen to avoid the appearing of the aforesaid peaks 1 and 2 in the examined temperature range.

Transmission electron microscopy (TEM) observations have been carried out on the samples in original condition and after test runs to describe the microstructural evolution and explain IF results.

5.5.2 Experimental

The chemical compositions of both superalloys are summarized in table V-1

	C	Cr	Co	Mo	W	Ti	Al	Ta	Ni	
PWA1483	0.05 0.09	11.6 12.7	8.50 9.50	1.65 2.15	3.50 4.10	3.90 4.25	3.40 3.80	4.80 5.20	to bal.	
	C	Cr	Co	Mo	W	Ti	Al	Ta	B	
IN792DS	0.07 0.09	12.2 12.8	8.50 9.50	1.70 2.10	3.85 4.25	3.75 4.15	3.15 3.55	3.85 4.25	0.01 0.02	
	Zr	Si	Mn	P	S	Fe	Cu	Nb	Hf	Ni
	Max 0.01	Max 0.1	Max 0.1	Max 0.015	Max 0.005	Max 0.5	Max 0.05	Max 0.01	0.8 1.2	to bal.

Tab. V-1 Superalloys chemical compositions.

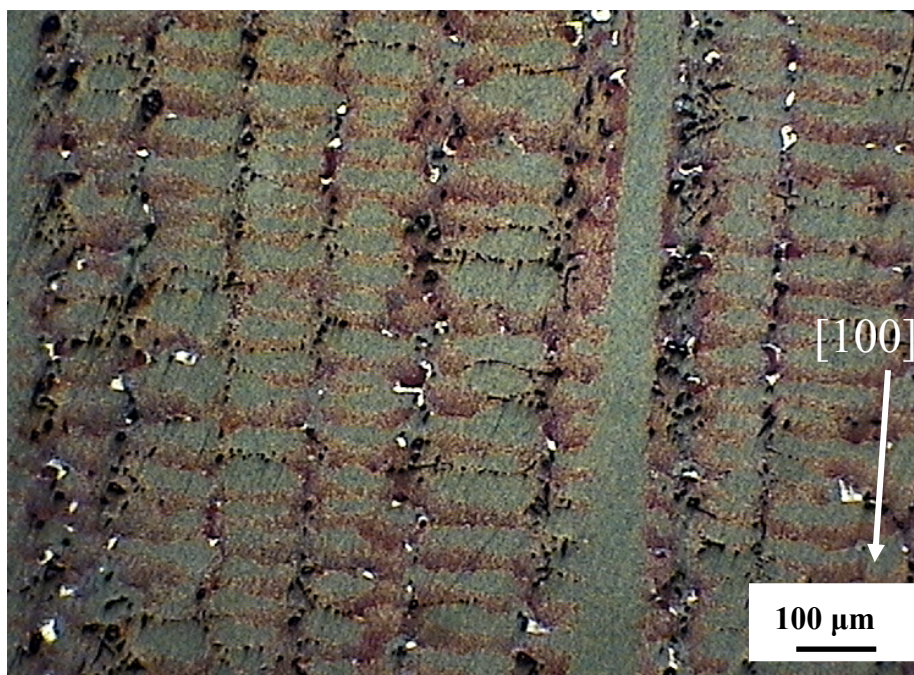As shown in fig. V-9 a, the materials (PWA1483SX) is a single crystal of γ phase hosting the ordered γ' phase, whose particles have the typical squared shape and an average size of about 1 μm. The γ' phase has a substantially homogeneous distribution with channels of ~ 100 nm between the particles; some particle-free (PF) zones of the matrix with size of 1-2 μm can be observed.
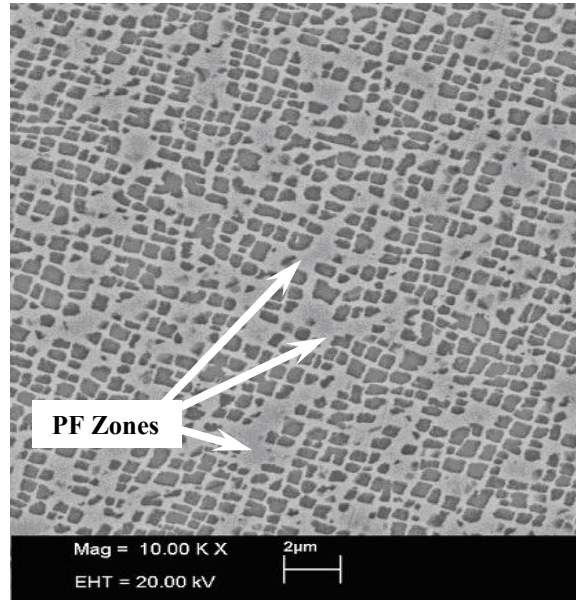
a)
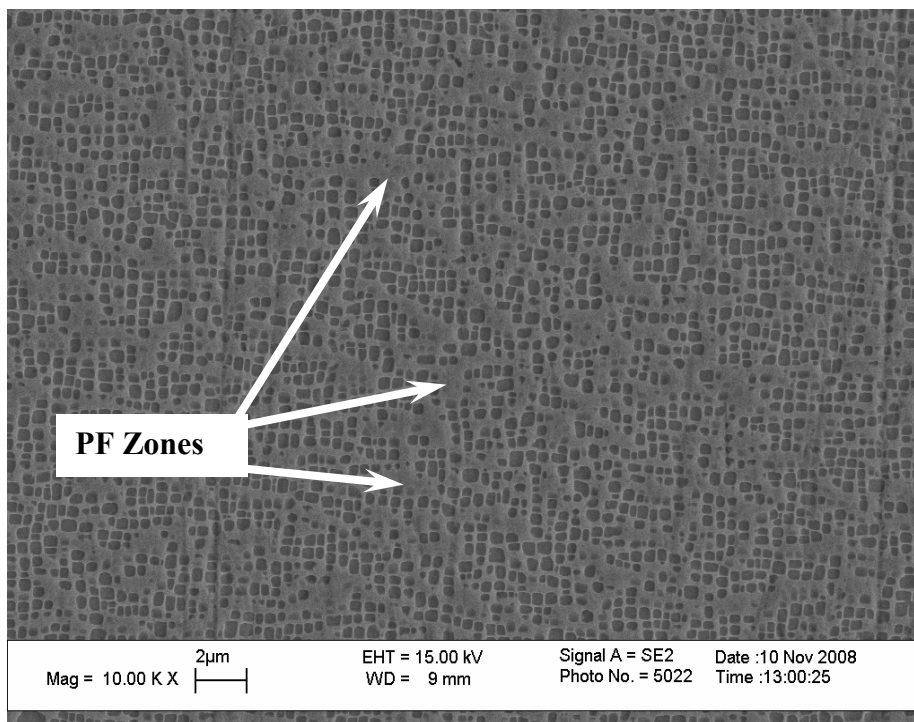
b)

c)

Fig. V-9   SEM micrograph showing the distribution of γ' particles in the matrix, respectively for the PWA1483 (a) and IN792DS (b); unidirectional structure of the alloy with [100] direction parallel to the ingot axis (c).

In figure V-9 are shown the ordered structure of the IN792DS/γ' (b) and in c) the grain direction [100] parallel to the ingot axis. The volume fraction of the ordered γ' phase is about 60 % for the PWA and 70 % for the IN792DS.

For both materials IF and dynamic modulus measurements have been carried out on bar-shaped samples (50 x 6 x 0.7 mm^3) using the method of frequency modulation. The VRA 1604 apparatus employed in the experiments was previously described in detail in [V-13]. Q^{-1} values have been determined from logarithmic decay of flexural vibrations. The resonance frequency was ~ 350 Hz. The samples have been heated from room temperature to 1073 K with heating rate of 1.7 x 10^{-2} K s^{-1}. The strain amplitude was kept lower than 1 x 10^{-5}. Repeated test runs have been performed on the same samples to assess their microstructural stability.

For XRD measurements, on IN792DS, two set of samples, respectively cut parallelly and perpendicularly to the ingot axis, have been subjected to the same thermal cycles performed during IF measurement runs. The spectra were collected using the Co Kα radiation (λ = 0.179 nm) in step-scanning mode with 2Θ steps of 0.05° and counting time of 2 s per step in the 2Θ angular range 40-120 degrees. High precision peak

profiles of the most intense reflections were recorded with 2Θ steps of 0.005° and counting time of 20 s per step.

5.5.3 Results

In successive test runs on the same samples a Q^{-1} maximum (M1) has been always observed at temperatures above 623 K. Its position does not depend on the resonance frequency and randomly changes in each run while its intensity tends to decrease. Sometimes, for the PWA1483 SX, M1 was accompanied by another maximum (M2) at lower temperature (~523 K) and of lower intensity. After some test runs the maxima disappear.

In correspondence of the Q^{-1} maximum, the modulus shows a slow decrease followed by a sharp increase. These results are illustrated in fig. V-10 a,b.
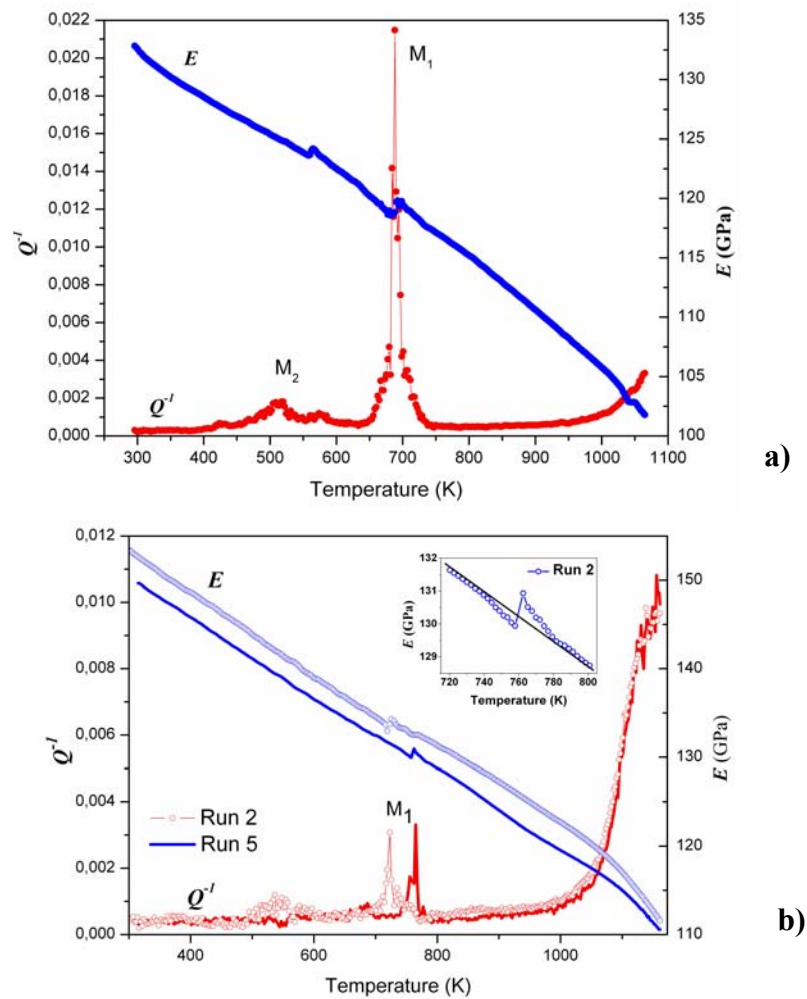

Fig. V-10- a) Q^{-1} and $(f/f_0)^2$ vs. temperature, PWA1483SX in the first test run; b) Q^{-1} and E vs. temperature for IN792DS in the 2nd and 5th test runs. The frame shows in detail the modulus behaviour in correspondence of maximum M$_1$ in the 2nd run.

At the end of each test run the modulus at room temperature is higher than the original one. Q^{-1} is lower for PWA1483SX (Fig. V-11a), and for the IN792DS is the contrary (Fig. V-11b). The variations of E and Q^{-1} occur mainly in the first runs, then negligible changes are observed; after stabilization Young's modulus has increased of $\sim 4\%$ with respect the original value for PWA and of $\sim 9\%$ for IN792DS.
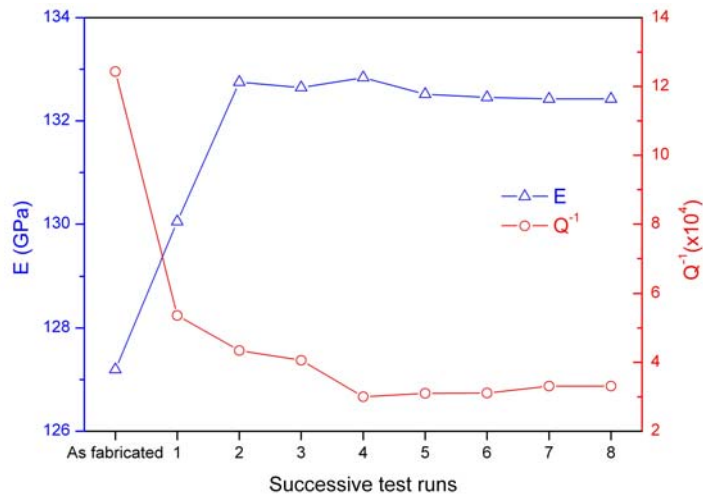
a)
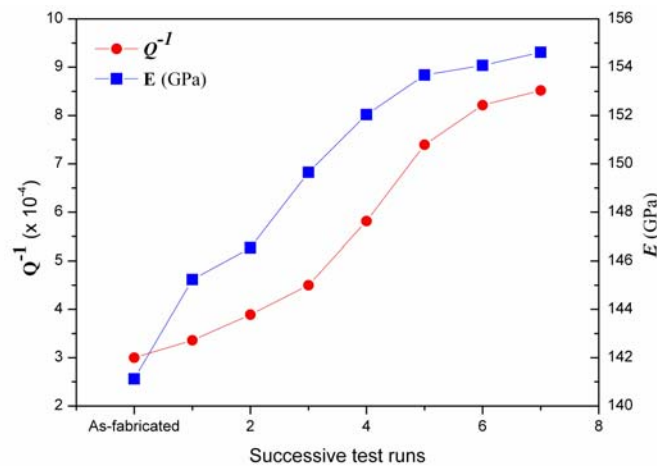
b)

Fig. V-11- Q^{-1} and modulus values at room temperature after successive test runs, a) PWA1483SX and b) for the IN792DS.

To understand the nature of such behaviour, TEM observations have been carried out on the original material and after successive test runs.

Figs. V-12 (a-b) show the PWA1483SX before IF tests. Micrographs display the different structures observed in the PF zones (Fig. V-12 a) and in the zones with homogeneous distribution of γ' phase (Fig. V-12 b).

In PF zones the dislocations are partially arranged to form networks with cells of about 50 nm. These structures are not present in the zones containing the γ' particles. Here dislocations are mainly concentrated in the channels between the particles.

After some test runs dislocation networks disappear and only some cells of large size can be observed. As shown in fig. V-12 c), in the zones with homogeneous γ' distribution the dislocation density decreases. Several of the remaining dislocations form pairs (super dislocations) in the channels, mostly at the γ- γ' phase boundaries.

100 nm
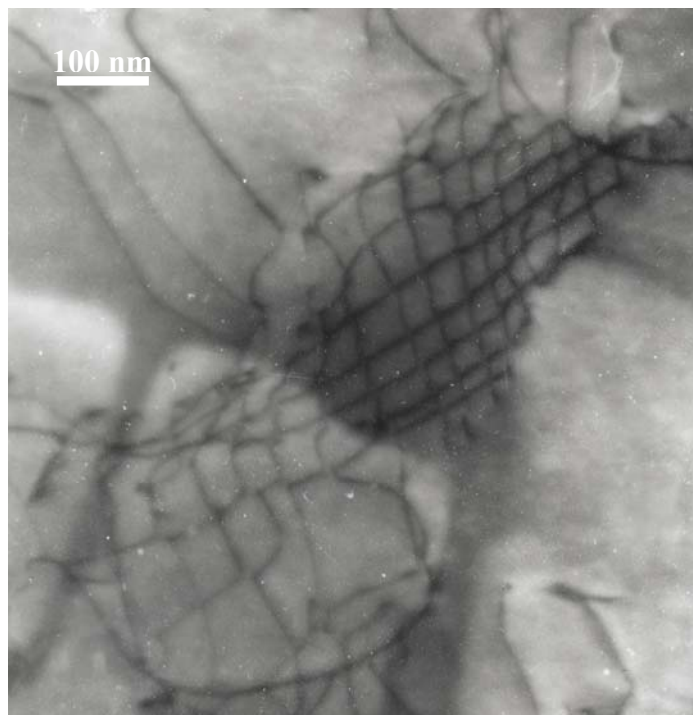
a)
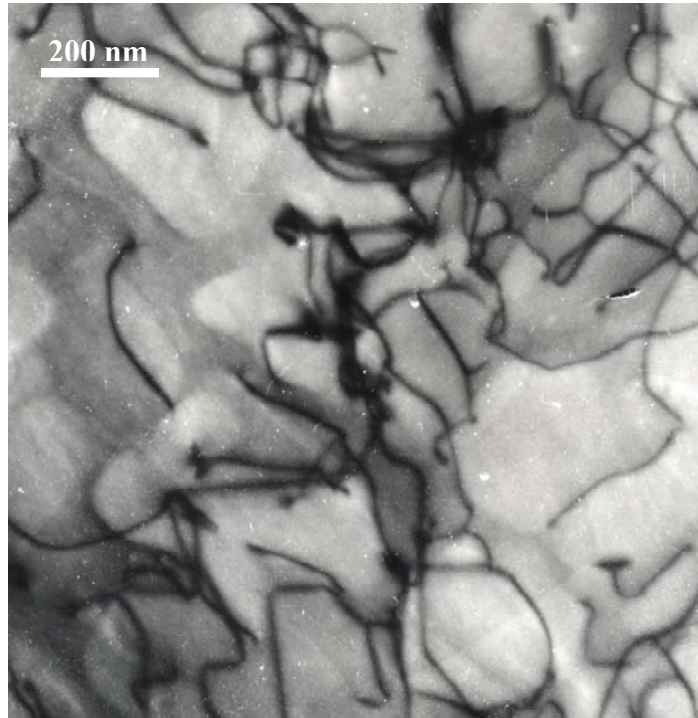
b)
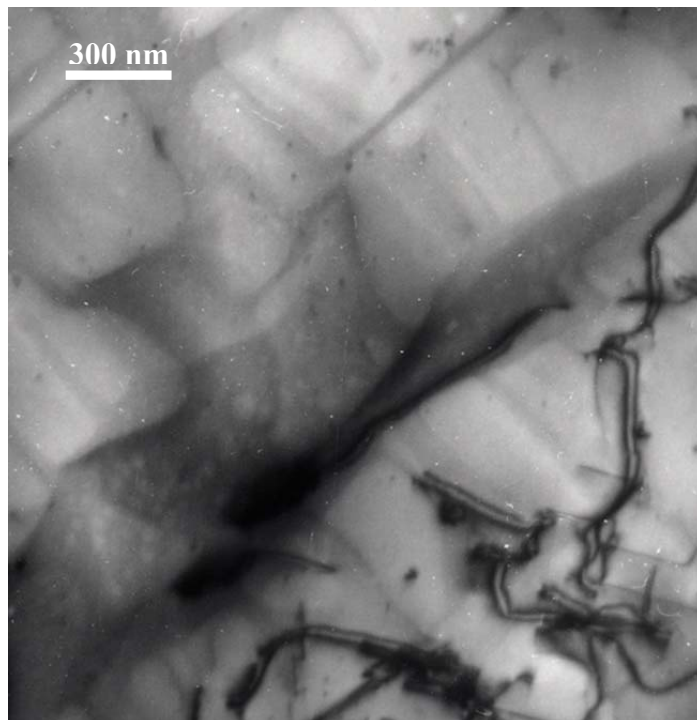
c)

**Fig. V-12- Zone without (a) and with (b) particles of γ' phase before IF test runs.
Zone with homogeneous distribution of γ' particles after eight test runs (c).**

TEM micrographs of fig. V-13 show the microstructural features of the IN792DS superalloy in the original condition (Fig. V-13 a-c) and after stabilization (Fig. V-13 d). In the original material dislocations are mainly present in the disordered γ phase (fig. V-13 a) and often surround the γ' particles (fig. V-13 b). Dislocation cells have been observed in the PF zones (fig. V-13 c). After the heat treatment the matrix has a lower density of dislocations, few dislocation networks with cells of large size are still observed. As shown by fig. V-13 d), some coarsening of γ' phase is observed and it takes place by coalescence of adjacent particles. In some cases the different orientation of particles is accomodated by dislocations at the interface.

a)

b)

c)

d)
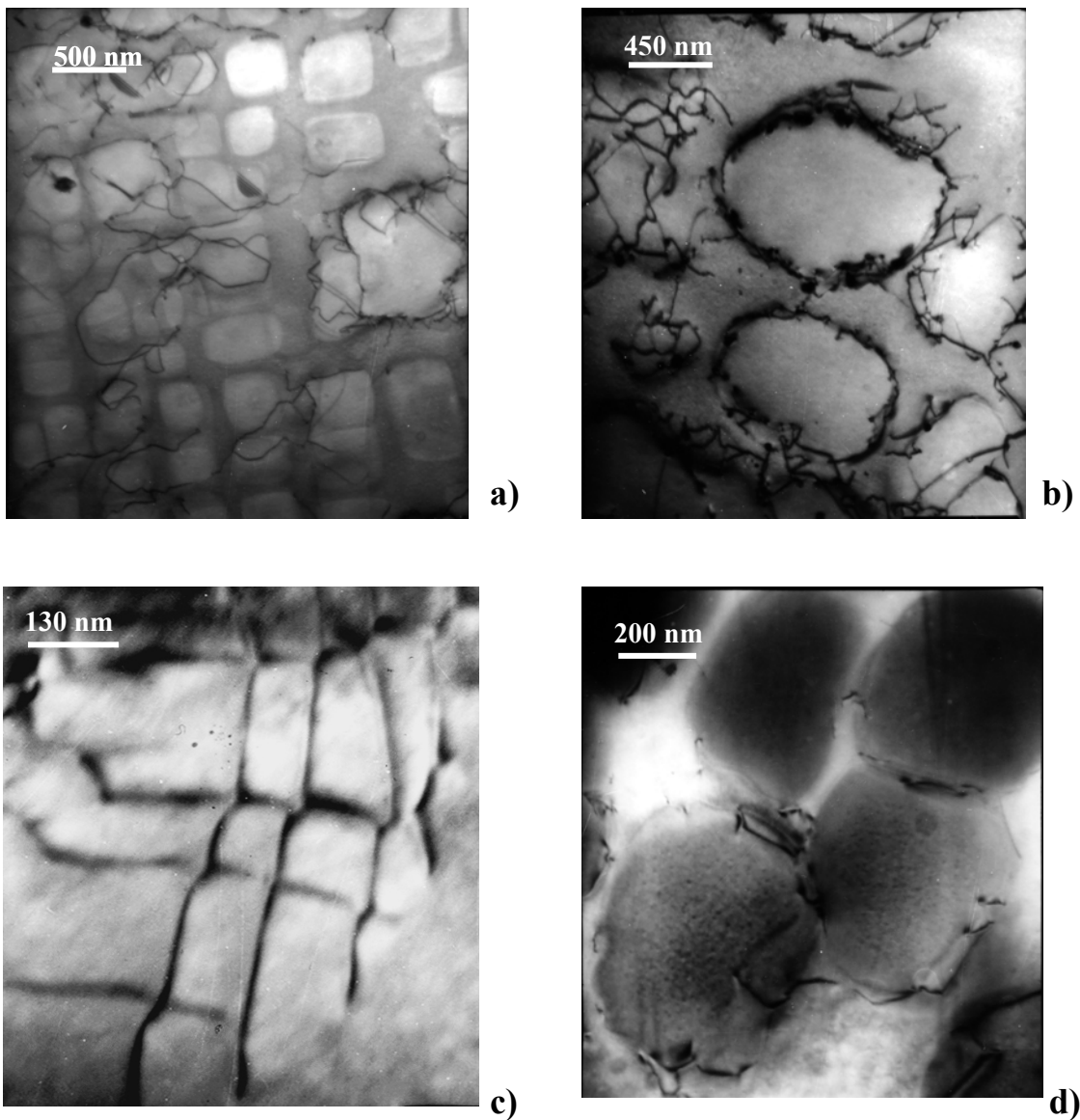
Fig. V-13- TEM micrographs of the superalloy in as-fabricated condition (a-c) and after stabilization heat treatment (IN792DS).

For the IN792DS superalloy, owing to the directional orientation of the grains, XRD spectra collected on samples cut perpendicularly to the ingot axis show only the {200} reflection while more reflections are detected in samples cut parallelly to the same axis (fig. V-14 a).

a)

b)

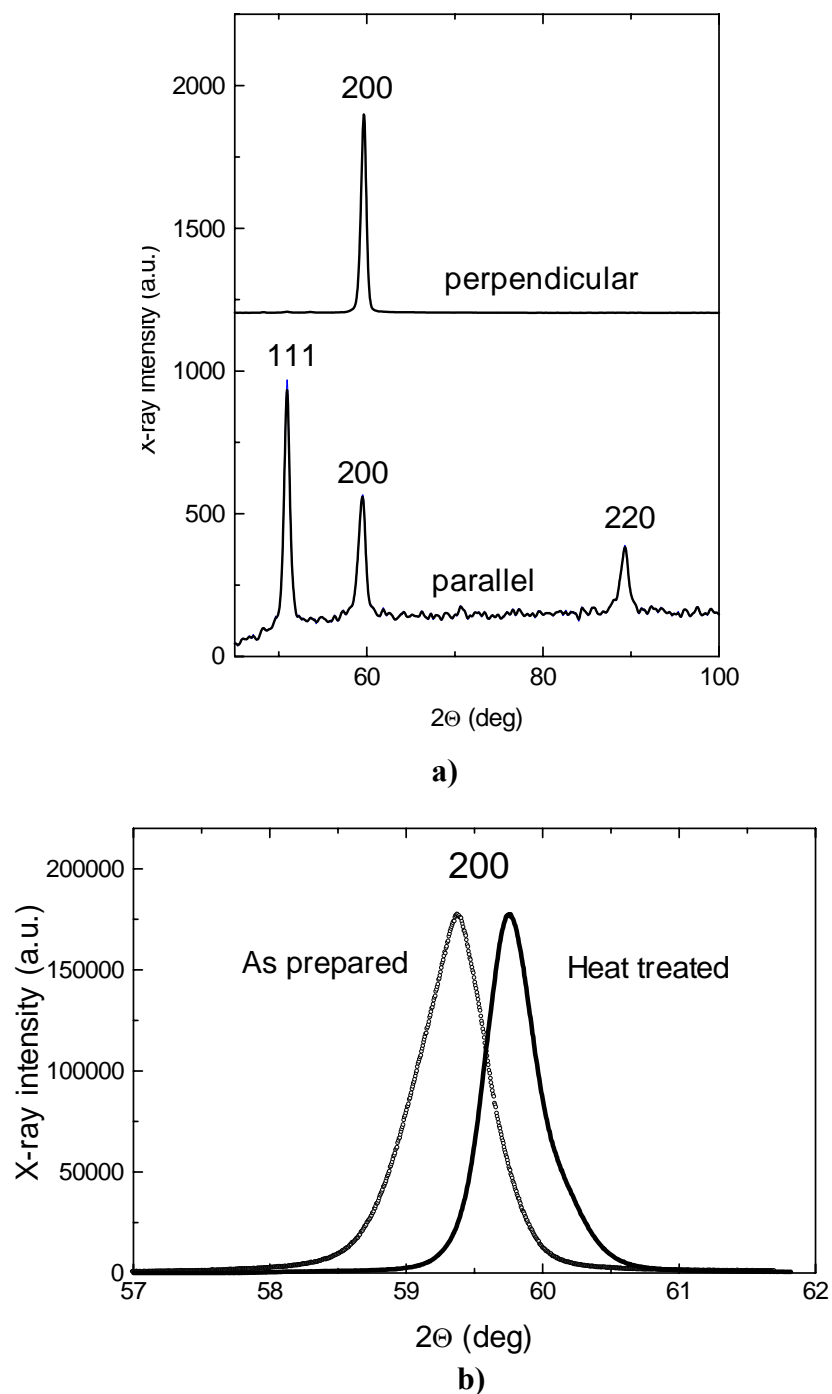**Fig. V-14- a) XRD spectra collected on samples cut parallelly and perpendicularly to the ingot axis. b) {200} reflections of the superalloy in as-prepared condition and after stabilization heat treatment. The intensities of the peaks have been normalized to make easier the comparison.**

Fig. V-14 b) shows the {200} peak profiles of the material in original condition and after stabilization measured on cross sections. The heat treatment induces a remarkable shift of the peak position from 59.435 to 59.775 (2Θ degrees) and a narrowing of peak profile with the half height line broadening β passing from 0.85 to 0.36 (2Θ degrees). Analogous behaviour has been observed for all the reflections collected on samples cut parallelly to the ingot axis, which have been used to determine the dislocation density.

For each XRD reflection the total line broadening β_T, corrected from instrumental contribution, is basically due to two terms, the size of coherently diffracting domains (β_D) and the micro-strains (β_ε), eq. (II-4).

From the plot of $\beta_T \cos\vartheta / \lambda$ vs. $\sin\vartheta / \lambda$ of the main reflections the domain size D and the micro-strain ε have been determined.

Finally, the dislocation density ρ was calculated by means of the Williamson-Smallman relationship [V-14] eq. (II-5).

From this calculation the values of $\rho_0 = 1.10 \times 10^{11}$ cm^{-2} and $\rho_S = 2.50 \times 10^{10}$ cm^{-2} for the as-prepared and stabilized materials have been obtained.

5.5.4 Discussion

The main characteristics of the aforesaid anelastic phenomena can be summarized as follows:

1- the positions of maxima M1 and M2 (when present) do not depend on the resonance frequency and randomly change in each test run;

2- modulus changes in correspondence of Q^{-1} maximum;

3- after each run the original values of resonance frequency f_0 and Q^{-1} at room temperature result modified.

These results are compatible with an irreversible microstructural transformation taking place in successive steps giving rise to Q^{-1} maxima. When the transformation has been completed the structure is stable and maxima are no more observed in IF spectra. The occurring of an irreversible transformation is in agreement also with the trends of Q^{-1} and f_0 measured at room temperature after successive test runs (fig.V-11 a-b). They progressively change and finally tend to constant values when transformation has been completed.

The explanation is based on the evolution of dislocation structures observed by TEM and XRD for the directional solidified superalloy. For simplicity, it is assumed that the only contribution to dislocation damping comes from free dislocations. At low frequencies, i.e. in kilohertz range, the Granato-Lücke string model for dislocation damping [V-11] predicts the following relationships:

$$Q^{-1} \propto \rho l^4 \omega \qquad\qquad \text{(V-1)}$$

$$\frac{\Delta G}{G} \cong -\beta \rho l^2 \qquad\qquad \text{(V-2)}$$

where β is a constant, ρ the dislocation density, l the average length between pinning points, $\omega=2\pi f$ where f is the vibration frequency. Although eq. (V-2) refers to the shear modulus G, the same effect occurs also for the Young's modulus. According to eqs. (V-1 and V-2), a decrease of ρ and l leads to higher values of modulus and lower values of Q^{-1}.

As schematically sketched in fig. V-15, the growth of cells occurs by coalescence, namely two or more cells of smaller size (Fig. V-15 a) from a cell of larger size   (Fig. V-15 c).

a)   b)   c)
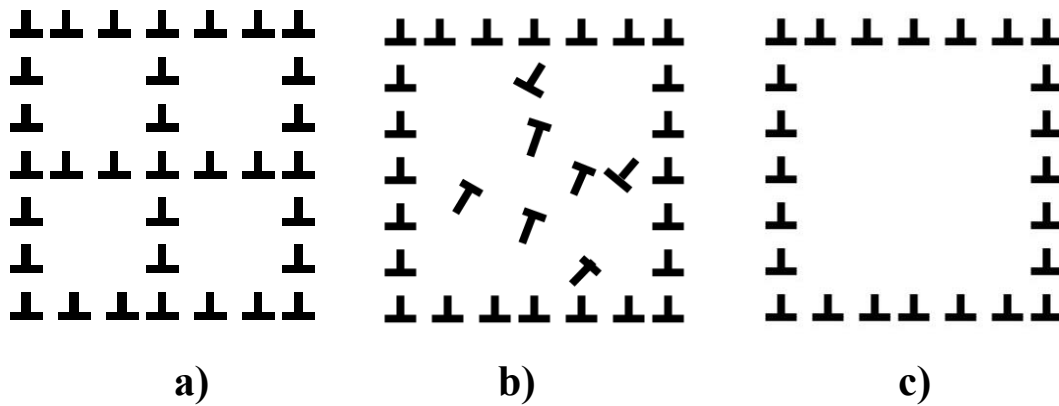
Fig. V-15- Cell structure (a). The walls dividing 4 cells break up (b). Dislocations in part annihilate, in part rearrange (c).

The process requires that the walls dividing the cells, which merge together, disappear. When a wall breaks up the dislocations forming the wall become free and are able to give their contribution to the damping, thus ρ increases determining the initial modulus decrease and the ascending part of a IF maximum. When dislocations rearrange in the walls of the new cell of larger size they can not contribute to damping so modulus increases and Q^{-1} decreases (descending part of maximum). Cell growth ends when the cells reach a size comparable to that of the corresponding PF zone. At that point the material has a stable microstructure which can not be further modified by successive heat cycling in the temperature range examined here.

If the mean distance l between dislocation pinning points remains unchanged the diminution of the dislocation density induces an increase of E (eq. V-2) and a decrease of Q^{-1} (eq. V-1). This has been previously observed to occur in the PWA 1483 single crystal superalloy in similar conditions of microstructural instability. On the contrary, for the IN792DS Q^{-1} shows an increasing trend.

Under the assumption that the IF background at room temperature is mainly due to dislocations damping, the ratio between the Q^{-1} values of the stabilized ($Q^{-1}{}_S$ = 8.5 x 10^{-4}) and as-prepared ($Q^{-1}{}_0$ = 3.0 x 10^{-4}) material, can be written in terms of eq. (V-1):

$$\frac{Q_S^{-1}}{Q_0^{-1}} = \frac{\rho_s l_s^4 \omega_s}{\rho_0 l_0^4 \omega_0} = 2.83 \qquad (V\text{-}3)$$

Substituting in eq. (V-3) ρ_S and ρ_0 determined by the XRD measuremnts and the experimental values ω_S = 2413 s^{-1} and ω_0 = 2306 s^{-1}, a ratio l_S / l_0 = 1.86 has been determined. This indicates that material stabilization is accompanied by a change of the average length between pinning points, being l higher in the heat treated material than in the original one. The phenomenon is likely connected to the begin of γ' coarsening because the coalescence of adjacent particles is driven by solute atom migration which could lead to dislocation unlocking.

From experimental results it is possible to conclude that the microstructure of the IN792 superalloy in as-fabricated condition is not stable.

Following the heat treatment the dislocation cells, present in the matrix, tend to grow forming cells of larger size. The irreversible process is not continuous but proceeds by steps occurring in successive test runs and each transformation step gives rise to an IF maximum. The rearrangement of dislocation structures in the matrix modifies both dislocation density and average distance of pinning points. When the growth leads to cells of size comparable to that of the corresponding PF zone, the process stops.

References

[V-1] H. Monjati, M. Jahazi, R. Bahrami, S. Yue, Materials Science and Engineering A, 373 (2004) 286-293.

[V-2] Shuangqu Zhao, Xishan Xie, Gaylord D. Smith, Shailesh J. Patel, Materials Letters, 58 (2004) 1784-1787.

[V-3] A.M. Ges, O. Fornaro, H.A. Palacio, Materials Science and Engineering A, 458 (2007) 96-100.

[V-4] P. Gadaud, K. Chakib, Materials Science Forum, Vol. 119-121 (1993) 397-400.

[V-5] W. Hermann, Th.V. Ort, H.G. Sockel, Journal de Physique III, Vol. 6 (1996) C8-223-226.

[V-6] A. Mourisco, N. Baluc, J. Bonneville, R. Schaller, Journal de Physique III, Vol. 6 (1996) C8-235-238.

[V-7] A. Mourisco, N. Baluc, J. Bonneville, R. Schaller, Materials Science and Engineering A, 239-240 (1997) 281-286.

[V-8] S. Frank, U. Södervall, Ch. Herzig, Phys. Stat. Sol. (b), Vol. 191 (1995) 45.

[V-9] L. di Masso, B. Coluzzi, F.M. Mazzolai, Journal de Physique III, Vol. 6 (1996) C8-247-250.

[V-10] P. Gadaud, A. Rivière, Journal de Physique III, Vol. 6 (1996) C8-867-870.

[V-11] E. Bonetti, E.G. Campari, A. Casagrande, L. Pasquini, E. Sampaolesi, Journal of Alloys and Compounds, 310 (2000) 351-355.

[V-12] M. Weller, M. Hirscher, E. Schweitzer, H. Kronmüller, Journal de Physique III, Vol. 6 (1996) C8-231-234.

[V-13] S. Amadori, E.G. Campari, A.L. Fiorini, R. Montanari, L. Pasquini, L. Savini, E. Bonetti, Materials Science and Engineering A, 442 (2006) 543-546.

[V-14] G.K. Williamson, R.A. Smallman, Philosophical Magazine, 1 (1956) 34-46.

[V-15] A.S. Nowick, B.S. Berry, Anelastic Relaxation in Crystalline Solids, Academic Press, New York and London, 1972, p. 415.

_____

Chapter 6

Spark Plasma Sintering (SPS)

6.1 Introduction

Nanostructured materials (d < 100 nm) can be produced by sintering nanostructured powders obtained by mechanical milling. The preparation of bulk nanostructured samples requires special consolidation processes, characterized by an overall low thermal load on the powder.

Spark Plasma Sintering (SPS) is a pressure assisted consolidation technology characterized by a high heating rate, a low sintering temperature and a short isothermal time at the sintering temperature.

The spark plasma sintering process offers significant improvements over conventional hot press and hot isostatic press sintering.

Theories on the SPS process vary, but most commonly accepted is the micro-spark/plasma concept, which is based on the electrical spark discharge phenomenon where in a high-energy, low-voltage pulse current momentarily generates spark plasma at high temperatures (many thousands of °C) in fine local areas between particles.

SPS' operational or "monitored" temperatures (200-2400°C) are commonly 200 to 500°C lower than with conventional sintering, classifying SPS as a lower-temperature sintering technology. Material processing (pressure and temperature rise and hold time) is completed in short periods of approximately 5 to 25 minutes. The relatively low temperatures combined with fast processing times ensure tight control over grain growth and microstructure.

6.2 Process
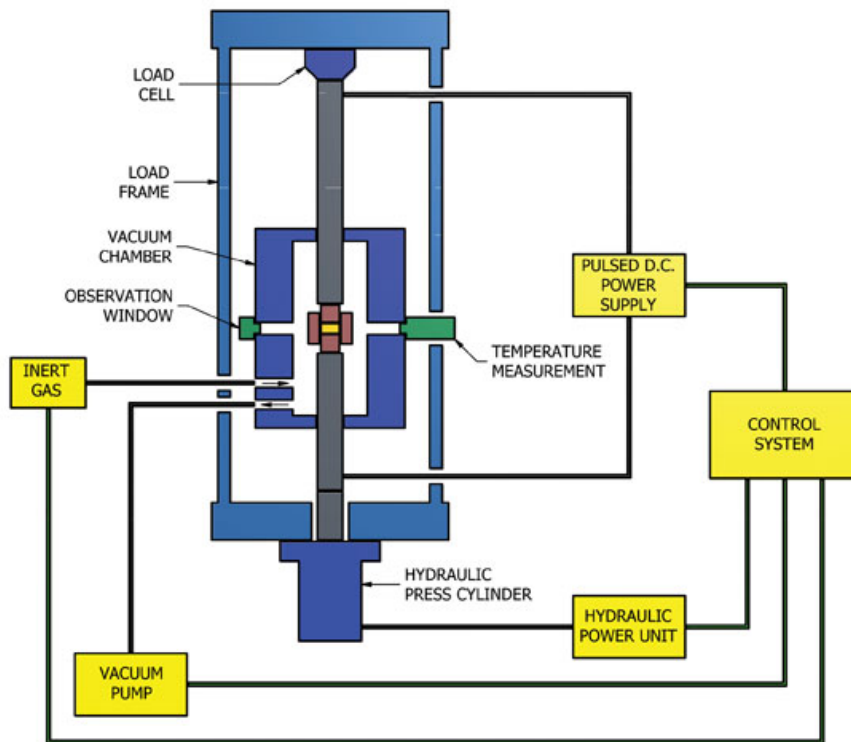
Fig. VI-1 Basic configuration of an SPS machine.

SPS utilizes uniaxial force and ON-OFF DC pulse energizing. The ON-OFF DC pulse voltage and current creates spark discharge and Joule heat points between material particles (high-energy pulses at the point of intergranular bonding). The high frequency transfers and disperses the spark/Joule heat phenomena throughout the specimen, resulting in a rapid and thorough heat distribution, high homogeneity and consistent densities.

The initiation of the spark discharge in the gap between particles is assisted by fine impurities and gases on and between the surfaces of the particles. The spark discharge creates a momentary local high-temperature state of up to 10000°C, causing vaporization of both the impurities and the surfaces of the particles in the area of the spark. Immediately behind the area of vaporization, the surfaces of the particles melt. Via electron draw during ON TIME and the vacuum of OFF TIME, these liquidized surfaces are drawn together, creating "necks." The ongoing "radiant" Joule heat and pressure causes these necks to gradually develop and increase. The radiant heat also

_____

causes plastic deformation on the surface of the particles, which is necessary for higher-density applications.

During the SPS process, heat is concentrated primarily on the surfaces of the particles. Particle growth is limited due to the speed of the process and the fact that only the surface temperature of the particles rises rapidly. The entire process - from powder to finished bulk sample - is completed quickly, with high uniformity and without changing the particles' characteristics.

Force (pressure) plays an important and predictable role in curbing particulate growth and influencing overall densities, but in the SPS process, accurate manipulation of force can actually enhance the process. Force multiplies spark initiation (diffusion) throughout the sample as the material moves under pressure, especially during critical out-gassing stages. Both too much and too little pressure can negatively influence the process. In large samples where high density is required, force is commonly increased in stages to enhance out-gassing and electrical diffusion.
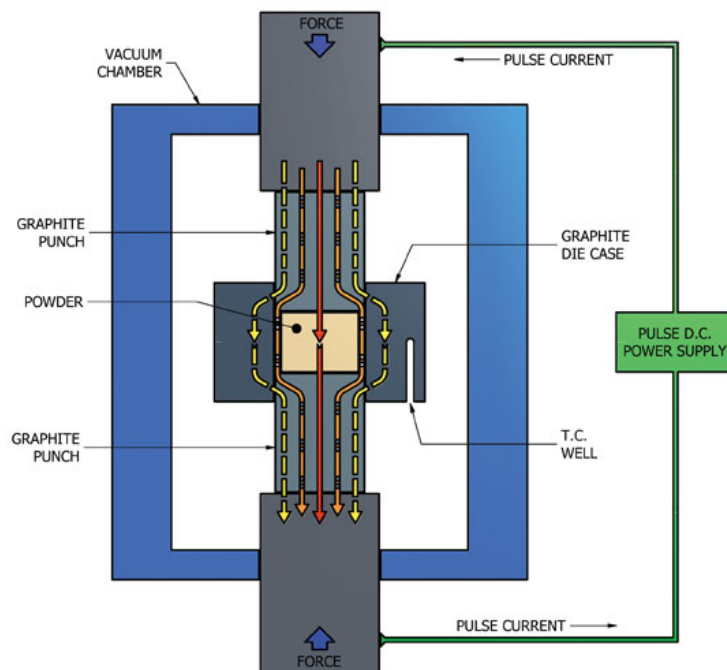
6.3 Applications

Fig. VI-2 ON-OFF pulsed current path through the machine.

_____

SPS is effective for any powder material application, but interest is especially high for nanocrystalline structures. Generally, super-fine materials have more surface area per volume than the same material made with larger particles. This, along with the way particles interact once compacted, "amplifies" material characteristics. In theory, high-strength materials show an increase in strength, highly wear-resistant materials show higher wear resistance, highly magnetic materials show higher magnetism, and so on. Suitable applications include advanced lightweight armament, guidance optics and ultra-high-strength tooling.

Nanomaterials haven't seen much industrial commercialization to date because conventional sintering technologies cause substantial particulate damage and growth. However, since SPS technology can sinter nanocrystalline materials with very little grain growth and negative particulate effect, the door is now open to test and study new ideas in powder material applications. Many common materials may well find new applications with substantially improved characteristics.

SPS technology can sinter materials without the use of binders. Most conventional powdered material sintering technologies require pre-forming and binders, and in many cases, expensive binder removal processes. Binders weaken the part due to their susceptibility to chemical wear, reduced hardness and strength, and oxidation breakdown. The availability of binder-less material could be valuable in numerous applications, including cobalt-less tungsten carbide, high-purity ceramic fuel cells and ceramic optics.
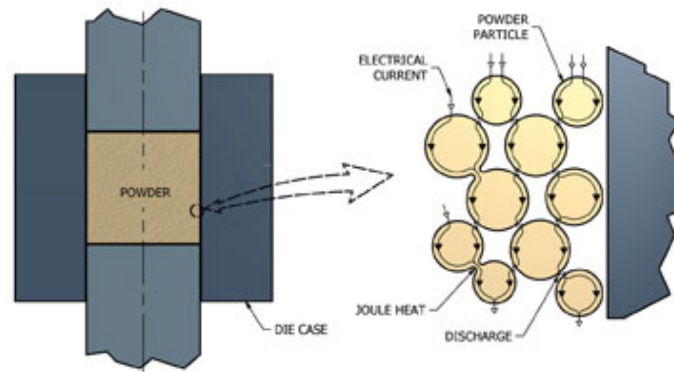
6.4 Part Characteristics

Fig. VI-3 ON-OFF pulsed current path through the powder.

The rapid spark diffusion and the consistent heat throughout the part produces very little internal stress within a part made with SPS. Many part failures occur due to internal stress and micro-cracks caused by heat migration during conventional sintering. SPS technology binds particles with electrical discharge energy evenly throughout the part. The heat is simultaneously consistent at the outside of the part and the centre. Along with the relative speed of the process, this eliminates much of the internal stress commonly seen in conventionally sintered parts.

SPS technology is capable of achieving nearly 100% theoretical density in almost any metallurgical or ceramic material, including composites. When ultra-high densities are required, some grain growth is necessary. Some materials require binders that are added to facilitate density with less grain growth, while other applications require very specific and uniform porosity. By accurately controlling compression and temperature, SPS technology can control material porosity while maintaining strong particle bonds throughout the shape.

"Net" and "near-net" shapes are also possible with SPS, going directly from powder to finished part in one step. Currently, these shapes need to be symmetrical and relatively simple; a complex shape would require secondary machining.

SPS technology can produce true seamless bonding (dry and liquid phase bonding). The SPS process draws particles together and offers the ability to reach nearly 100% theoretical density, the process can produce bonded parts that have no seam. This bonding phenomenon is possible between like and dissimilar materials, though radically

_____

dissimilar materials require progressing layers between the initial materials to account for different thermal stresses. In the case of bonding rough surfaces, loose powder can be applied between the surfaces to ensure a solid bond.
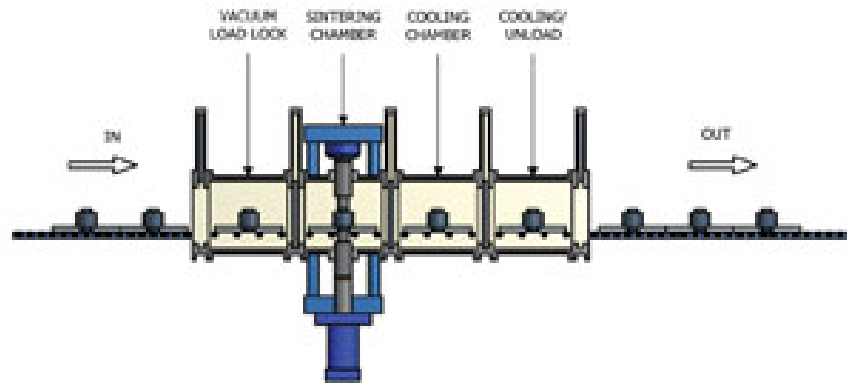

6.5 Benefits

Fig. VI-4 Example of a production concept.

As mentioned previously, the SPS process utilizes high-amperage pulse DC current to generate spark plasma energy between each particle. Physical compression can be up to 300 tons and the chamber is under negative atmospheric pressure (vacuum) with or without inert gas. Heat is concentrated on the surface area of each particle, and every particle is equally and completely bonded with the surrounding particles. Under high pressure, mild plastic deformation of the particles ensures ultra-high density values, while high-porosity, fully bonded materials can be achieved with lower pressure and less heat and time.

Pre-existing oxidation and contaminates are vaporized from particle surfaces during sintering, providing for higher-purity materials and stronger bonding between particles. SPS is capable of sintering dissimilar materials without going to a liquid phase on the lower-temperature materials. In the case of composite materials, high homogeneity is possible even with lower densities. In the case of layered materials known as functionally graded materials (FGMs), preformed layers remain consistent in density and shape even if the materials have radically different sintering properties.

Consideration of a powdered metallurgical "recipe" requires metallurgical expertise, but the actual operation of the machine is quite simple. Once the die set is loaded and the t

_____

emperature feedback system (thermocouple or pyrometer) is in place, the operator programs the temperature and pressure ramp-up and hold settings. The atmosphere (vacuum and/or inert gas) is set, the electrical settings (ON-OFF times and frequency strategy) are programmed and then the data feedback graphics are set up. SPS technology can also be combined with various forms of production and automation systems, including multi-head, rotary, batch, and conveyor systems. Robotic interface is also possible.

Finally, SPS operational expenses are consistently 50 to 80% less than conventional sintering technologies, due primarily to speed. In some applications, SPS technology has been more than 20 times faster than conventional sintering technologies. Most SPS applications only require minutes in comparison to the hours needed with conventional systems.

6.6 Damping of nanostructured Alloy FeMo produced by Spark Plasma Sintering

6.6.1 Introduction

Nanostructured materials ($d < 100$ nm) possess a better strength as compared to the conventional ones [VI-1-3]. They can be produced by sintering nanostructured powders obtained by mechanical milling. A fully dense material can be produced by conventional sintering only at high temperature, which leads to grains of larger size [VI-4-6] thus the preparation of bulk nanostructured samples requires special consolidation processes, characterized by an overall low thermal load on the powder. Spark Plasma Sintering (SPS) is a novel pressure assisted consolidation technology characterized by a high heating rate, a low sintering temperature and a short isothermal time at the sintering temperature [VI-7-9]. It has been successfully used by one of the authors to process nanostructured powders [VI-10-12].

To investigate the microstructural stability, repeated tests of mechanical spectroscopy have been performed on samples prepared under different conditions. The samples have been also observed by transmission electron microscopy (TEM) and examined by X-ray diffraction (XRD).

_____

6.6.2 Materials and experimental

The examined materials have been prepared through the following steps:

   1- a powder of Fe–1.5 wt.% Mo (FeMo), produced by water atomization, has been mixed with 1.5 wt.% of nanometric SiO_2 powder with mean particle size of 10 nm and purity better than 99.5 %;

   2- the mixture has been high energy milled to obtain a nanostructure;

   3- it has been then consolidated by SPS under different conditions.

Oxide particles were added to control grain growth on sintering. Details on the preparation of the mixture, as well as on the high energy milling conditions, are reported in [VI-10].

SPS was carried out on a DR.SINTER$^{®}$ SPS1050 (Sumitomo Coal & Mining, now SPS Syntex Inc.) apparatus with graphite punches and die. Disks (30 mm diameter, 5 mm height) were produced with the following sintering schedule:

   1- heating at 1.7 Ks^{-1} up to the maximum temperature (varying from 1073 to 1173 K); 2- holding for 1 minute;

   3- free cooling;

   4- a compressive pressure of 30-60 MPa, was applied during the heating step.

IF and dynamic modulus measurements have been carried out on bar-shaped samples (13.6 x 4.6 x 0.55 mm^3), machined by electric discharge from the disks. The VRA 1604 apparatus employed in the experiments was described in detail in [VI-13]. Q^{-1} values have been determined from logarithmic decay of flexural vibrations. The resonance frequency f was ~ 1800 Hz. The samples have been heated from room temperature to 923 K with heating rate of 1.7 x 10^{-2} Ks^{-1}. The strain amplitude was kept lower than 1 x 10^{-5}. Since the modulus E is proportional to f^2 (see Eq. I-8), its evolution vs. temperature has been described by $(f/f_0)^2$ where f_0 is the initial resonance frequency at room temperature.

Test runs have been repeated on the same samples to assess the structural stability.

Discs for TEM inspections were prepared as follows:

   a) FeMo powders: by electrolytic deposition. The experimental setting consisted of a Ni anode and a stainless steel cathode with a DC of 100 mA, equipped with electromagnetic stirring, pH and temperature controlling devices. Current is made to pass though a solution of 300 g $Ni(SO_3NH_2)4H_2O$, 20 g of H_3BO_3, 10 g of $NiCl_2$ in 500 ml distilled water (pH fixed at the value of 3 and T at room temperature).

_____

b) All the SPS materials: by ion-milling. A PIPS ion miller was used. Thin foils were mechanically ground to 100-120 µm, punched and dimpled down to a thickness ranging 30-35 µm. Ion milling was initially set to a V=5V and a tilt angle of 4°, followed by the final step at a tilt angle of 2°. The rotating specimen holder was kept chilled with liquid nitrogen.

TEM inspections were carried out using a Philips™ CM200 equipped with a double tilt specimen holder and nano-probe microanalysis facility. Identification of phases and oxides was performed through several nano-probe analyses, together with selected area electron diffraction patterns (SAEDPs) indexing, when possible. HREM and TEM images were recorded using a dedicated CCD camera.

XRD measurements have been carried out using the radiation Mo-Kα (λ = 0.07093 nm). Spectra were collected in step-scanning mode with 2Θ steps of 0.05° and counting time of 2 s per step in the angular range 10°-50°. High precision peak profiles of the most intense reflections were recorded with 2Θ steps of 0.005° and counting time of 20 s per step. In tab. 1 are reported the values of the dislocation density calculated from the eq. (II-5).

Material	D (nm)	ξ (cm^{-2})
Set A as-prepared	100	2.6×10^{11}
Set A after IF test runs	120	7.6×10^{9}
Set B as-prepared	1000	5.7×10^{11}
Set B after IF test runs	4000	9.8×10^{10}

Table VI-1- Average grain size D and dislocation density ξ of samples of sets A and B in as-prepared condition and after IF test runs.

_____

6.6.3 Results

SPS sintering in aforesaid conditions always produced samples with good density, 95÷100 % of that of the bulk alloy, however, remarkable differences were observed in the final grain size. In particular, the sintering temperature T_S is a critical parameter because, passing from 1113 K to 1128 K, variations of average grain size from ~100 nm to ~1 μm are observed. The results reported here regard two groups of samples: set A with T_S = 1113 K and set B with T_S = 1128 K. To evaluate the structural stability of the materials each sample has been subjected to successive IF test runs.

Fig.VI-5 a) shows Q^{-1} and $(f / f_0)^2$ vs. temperature for a sample of set A in two successive tests.

In all the tests Q^{-1} exponentially increases at high temperature while the modulus monotonically decreases except in the first run where an anomalous drop of resonance frequency has been observed in the temperature range 650-700 K.

The Q^{-1} and $(f/f_0)^2$ values measured at room temperature after each run are reported in fig. VI-5 b).

After the first run Q^{-1} and modulus show a slight decrease then remain substantially stable.

A different behaviour has been observed in samples of set B (fig. VI-6 a-b).

Some maxima of different intensity are superimposed to the Q^{-1} exponential increase with corresponding modulus variations. Successive runs do not stabilize the material, on the contrary, the phenomena seem to become more important. After successive runs the room temperature value of dynamic modulus increases while that of Q^{-1} decreases (fig. VI-6 b).

The particles of ball milled powder are formed by two different zones: the outer zone exhibits a high density of dislocations, the inner one is highly deformed but has few dislocations (fig. VI-7 a-b).

After SPS it is not possible to distinguish the original particles; the average grain size is ~100 nm in the samples sintered at 1113 K (fig. VI-8 a) while it is at least one order of magnitude larger in the samples sintered at 1128 K (fig. VI-8 b). In both the sets A and B nano-pores can be observed. As shown in figs. VI-8 e) and f), they are of smaller size (~10 nm) and more homogeneous distribution in set A than in set B (size of ~80 nm).

a)

b)

Fig.VI-5- Set A- a) Trends of Q^{-1} and $(f/f_0)^2$ vs. temperature in two successive test runs. **b)** f_0 and Q^{-1} measured at room temperature after successive test runs.
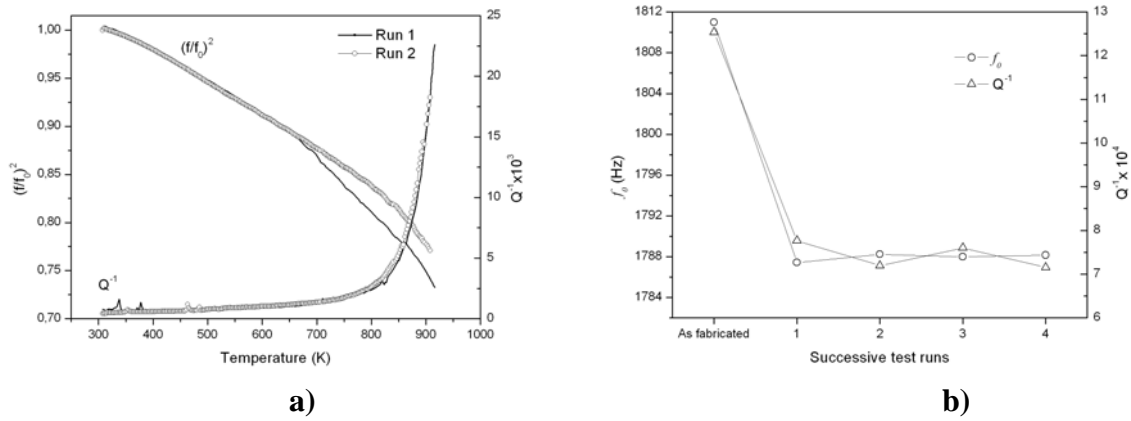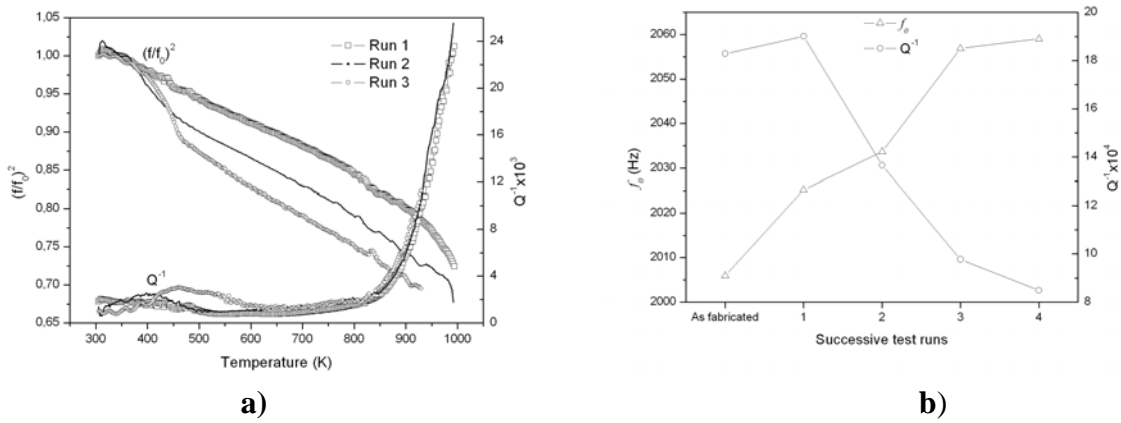

a)

b)

Fig. VI-6- Set B- a) Trends of Q^{-1} and $(f/f_0)^2$ vs. temperature in three successive test runs. **b)** f_0 and Q^{-1} measured at room temperature after successive test runs.
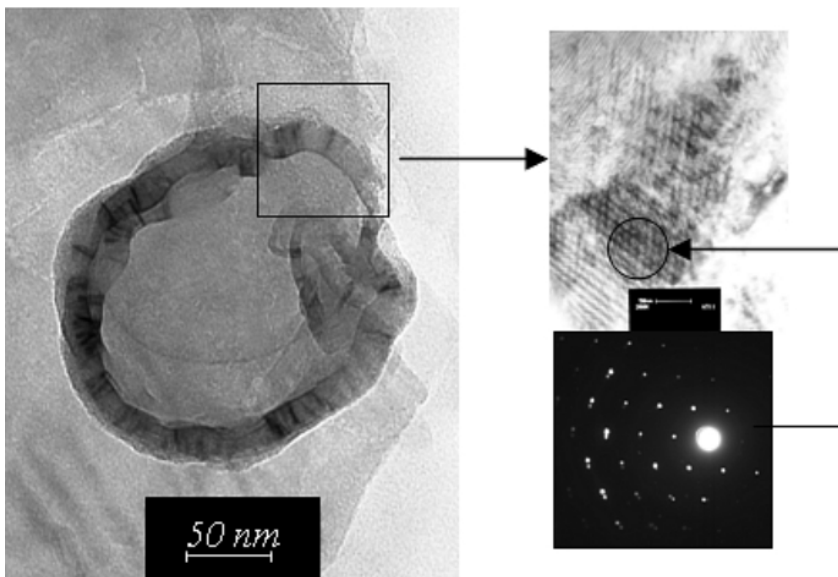

50 nm

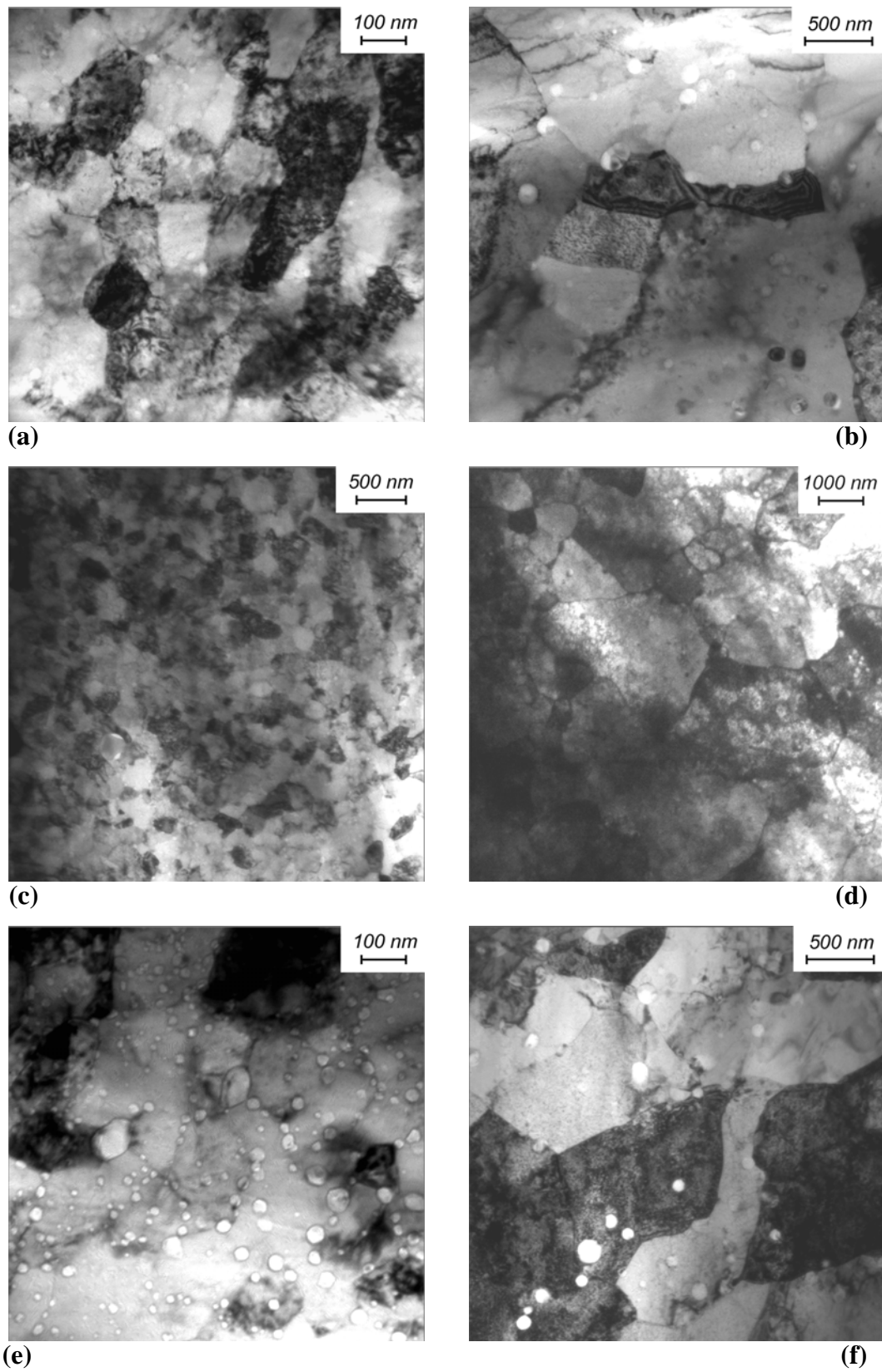**Fig. VI-7- Particles of ball milled powder (a-b).**

Fig. VI-8- Set A before (a) and after test runs (c-e). Set B before (b) and after test runs (d-f).

IF test runs induce small changes in the average grain size of set A (fig. VI-8 e) whereas that of set B shows a further increase with grains of about 4-5 µm (fig. VI-8 f). Pore size distribution seems to be scarcely affected by IF measurement cycles.

XRD shows that peak profiles of set A are always broader than those of set B. For example, fig. VI-9 displays the {211} reflections of both the sample groups before and after IF test runs. To make easier the comparison their intensities have been normalized. The analysis of peak profiles has been exploited to get the dislocation density. For each XRD reflection the total line broadening β_T (eq. II-4), corrected from instrumental broadening, is basically due to two contributions, the size of coherently diffracting domains (β_D), i.e. the grains, and the micro-strains (β_ε).

Plotting $\beta_T \cos\vartheta / \lambda$ vs. $\sin\vartheta / \lambda$ for several reflections the values of D and ε have been determined. D values correspond to those measured by TEM. Finally, the dislocation density ξ was calculated by means of the Williamson-Smallman relationship [VI-14] (Eq. II-5), with $\Xi = 16$ is a constant, $b = 0.1241$ nm the modulus of Burgers vector and $k_0 \cong 1$ a factor depending on dislocation interaction. The calculated values are reported in Tab. 1.
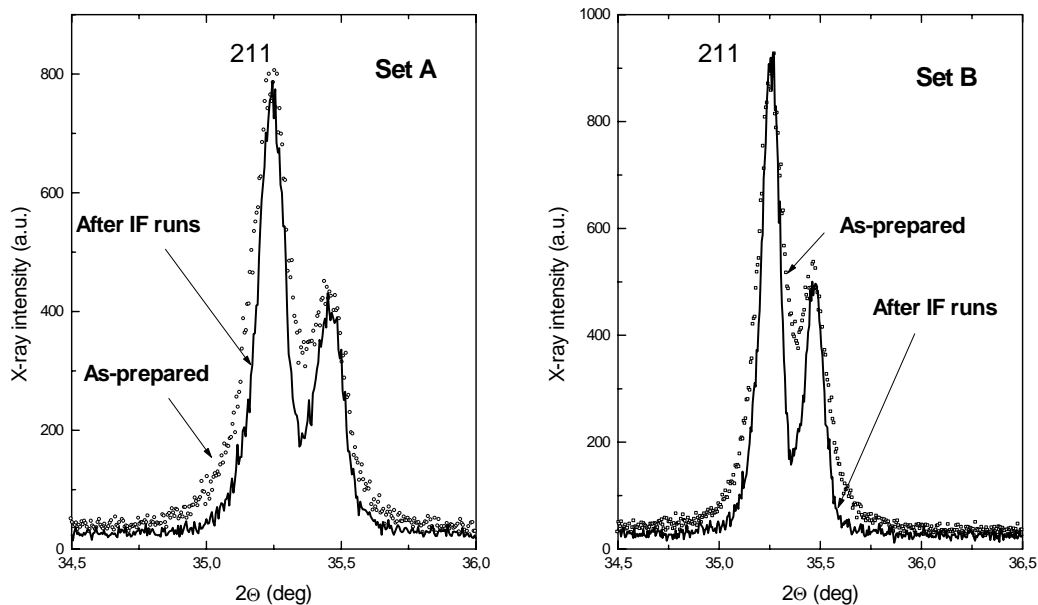

Fig. VI-9- {211} precision peak profiles of sets A and B before and after test runs. Their intensities have been normalized.

_____

6.6.4 Discussion

The change of Q^{-1} and $(f/f_0)^2$ values after successive test runs (fig. VI-5 and fig VI-6 b) clearly indicates that irreversible transformations take place in the samples of both the sets. In set A, these values show a slight decrease after the first run then remain substantially stable. The behaviour of set B is quite different: the changes occur in all the cycles, in addition the modulus exhibits an increasing trend.

Although materials consolidated via SPS have a high density (99.7 % for set A and 99.9 % for set B), there is always a residual presence of nano-pores.

IF cycles involve the successive heating and cooling of samples; since the pores act as sinks for vacancies during cooling step, they tend to grow. However, the conditions of present experiments seem to scarcely affected their size distribution (see fig. VI-8). Therefore, nano-pore evolution can not be responsible for the anelastic behaviour of materials.

To explain the aforesaid damping phenomena, one has to consider that the main microstructural effect of IF measurement cycles on samples of set B is to further increase their average grain size. Some grain coarsening has been observed also in set A but it is of very limited extent. The coalescence of grains involves rearrangement of dislocations, which can produce dissipative effects. At low frequencies, i.e. in kilohertz range, the Granato-Lücke string model for dislocation damping [VI-15], predicts the relationships IV-1 and IV-2.

The coalescence of two grains can be thought as a two step process. In the first step the grain boundary breaks up and the dislocations forming the boundary become free and able to oscillate under the external sinusoidal stress. So, according to Eqs. (IV-1 and IV-2), the increase of ξ and l leads to higher values of Q^{-1} and lower values of elastic modulus. In fact, this corresponds to the ascending part of the maxima. In the second step the dislocations, which formed the old boundary, in part annihilate in part rearrange in the remaining boundaries. Consequently, ξ and l decrease inducing a decrease of Q^{-1} (descending part of maxima).

Grain coalescence is a jerk process thus several successive maxima are observed in test runs of samples of set B. After each cycle the overall dislocation density is in general lower than the initial one, consequently the trend of Q^{-1} is decreasing and that of modulus increasing.

As shown by XRD, also dislocation density of set A decreases after test runs so one would expect Q^{-1} and $(f/f_0)^2$ trends similar to those of set B. How do explain that modulus decreases after the first run? The as-prepared samples of set A have nanometric grain size and homogeneously distributed nano-porosity. These features make them harder and more brittle than samples of set B. It is reasonable that small cracks may form during the first test to accommodate internal stresses. Crack formation would reduce the effective sample thickness h and, according to Eq. (I-8), the resonance frequency. The anomalous resonance frequency behaviour can be ascribed to the formation of cracks.

_____

References

[VI-1] S. Takaki, K. Kawasaki, Y. Kimura, J. of Mater. Proc. Tech., 117 (2001) 359.

[VI-2] N. Tsuji, Y. Ito, Y. Saito, Y. Minamino, Scripta Materialia, 47 (2002) 893.

[VI-3] D. P. Harvey, R. Kalianaraman, T. Sudarshan, Mater. Sci. and Tech., 18 (2002) 959.

[VI-4] D. R. Amador, M. A. Monge, J. M. Torralba, R. Pareja, Appl. Phys. A, 80 (2005) 803.

[VI-5]. T. R. Malow, C. C. Koch, Acta Materialia, 45 (1997) 2177.

[VI-6] C. E. Krill, L. Helfen, D. Michels, H. Matter, A. Fitch, O. Masson, R. Birringer, Phys. Rev. Lett., 86 (2001) 842.

[VI-7] M. Kawahara, H. Kim, M. Tokita, Proc. of Powder Metallurgy World Congress, 741; 2000.

[VI-8] H. W. Zhang, R. Gopalan, T. Mukai, K. Hono, Scripta Materialia, 53 (2005) 863.

[VI-9] M. Zadra, F. Casari, L. Girardini, A. Molinari, Powder Metallurgy, 50 (2007) 40.

[VI-10] S. Libardi, M. Leoni, L. Facchini, M. D'Incau, P. Scardi, A. Molinari, Mater. Sci. and Eng. A, 445-446 (2007) 244.

[VI-11] L. Girardini, M. Zadra, F. Casari, A. Molinari, Proc. of EUROPM2007, Tolouse (France), September 2007.

[VI-12] M. Zadra, F. Casari, A. Molinari, Materials Science Forum, 534-536 (2007) 1401.

[VI-13] S. Amadori, E.G. Campari, A.L. Fiorini, R. Montanari, L. Pasquini, L. Savini, E. Bonetti, Materials Science & Engineering A, 442 (2006) 543.

[VI-14] G.K.Williamson and R.A.Smallman, Phil. Mag., 1 (1956) 34.

[VI-15] A.S. Nowick, B.S. Berry, Anelastic Relaxation in Crystalline Solids, Academic Press, New York and London, 1972, p. 415.

Chapter 7

Human Teeth

7.1 Introduction

Dental anatomy is a field of anatomy dedicated to the study of tooth structures. The development, appearance, and classification of teeth fall within its field of study, though dental occlusion, or contact among teeth, does not. Dental anatomy is also a taxonomical science as it is concerned with the naming of teeth and their structures.

The anatomic crown of a tooth is the area covered in enamel above the cement-enamel junction (CEJ) [VII-1-3]. The majority of the crown is composed of dentin with the pulp chamber in the centre [VII-4]. The crown is within bone before eruption [VII-5]. After eruption, it is almost always visible. The anatomic root is found below the cement-enamel junction and is covered with cementum. As with the crown, dentin composes most of the root, which normally have pulp canals. A tooth may have multiple roots or just one root. Canines and most premolars, except for maxillary (upper) first premolars, usually have one root. Maxillary first premolars and mandibular molars usually have two roots. Maxillary molars usually have three roots. Additional roots are referred to as supernumerary roots.

Teeth are classified as incisors, canines, and molars. In the primary set of teeth, there are two types of incisors, centrals and laterals, and two types of molars, first and second. All primary teeth are replaced with permanent counterparts except for molars, which are replaced by permanent premolars. Among permanent teeth, 16 are found in the maxilla with the other 16 in the mandible. The maxillary teeth are the maxillary central incisor, maxillary lateral incisor, maxillary canine, maxillary first premolar, maxillary second premolar, maxillary first molar, maxillary second molar, and maxillary third molar. The mandibular teeth are the mandibular central incisor, mandibular lateral incisor, mandibular canine, mandibular first premolar, mandibular second premolar, mandibular first molar, mandibular second molar, and mandibular third molar. Third molars are commonly called "wisdom teeth" and may never erupt into the mouth or form at all. If any additional teeth form, for example, fourth and fifth molars, which are rare, they are referred to as supernumerary teeth [VII-6]

Most teeth have identifiable features that distinguish them from others. There are several different notation systems to refer to a specific tooth. The three most common systems are the FDI World Dental Federation notation, the universal numbering system, and Palmer notation method. The FDI system is used worldwide, and the universal is used widely in the United States.

7.2 Parts

Enamel is the hardest and most highly mineralized substance of the body and is one of the four major tissues which make up the tooth, along with dentin, cementum, and dental pulp [VII-7]. It is normally visible and must be supported by underlying dentin. Ninety-six percent of enamel consists of mineral, with water and organic material composing the rest [VII-8]. The normal colour of enamel varies from light yellow to grayish white. At the edges of teeth where there is no dentin underlying the enamel, the colour sometimes has a slightly blue tone. Since enamel is semi translucent, the colour of dentin and any restorative dental material underneath the enamel strongly affects the appearance of a tooth. Enamel varies in thickness over the surface of the tooth and is often thickest at the cusp, up to 2.5 mm, and thinnest at its border, which is seen clinically as the cement-enamel junction (CEJ) [VII-9]
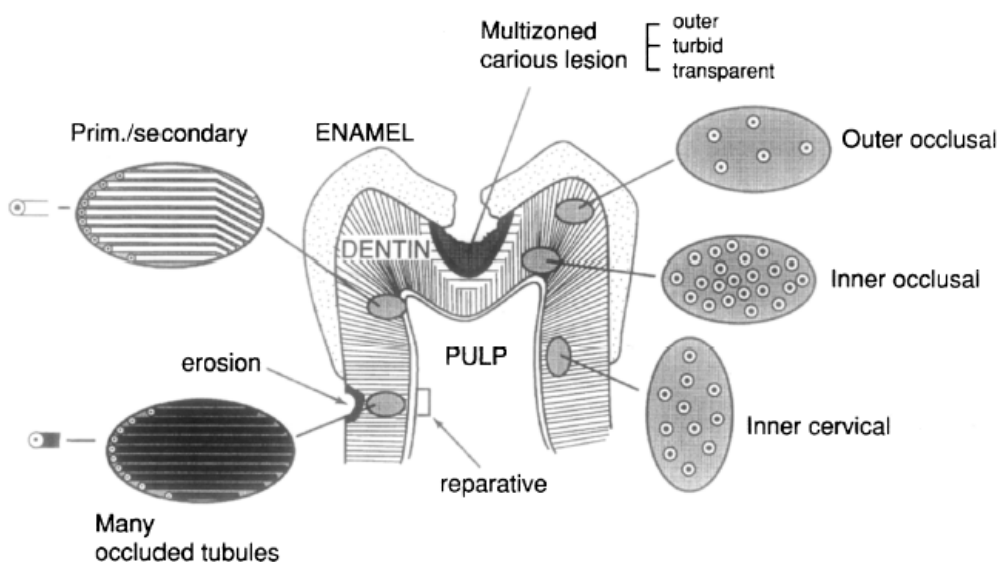

Fig. VII-1 Section of human teeth

Enamel's primary mineral is hydroxyapatite, which is a crystalline calcium phosphate [VII-10]. The large amount of minerals in enamel accounts not only for its strength but also for its brittleness [VII-11]. Dentin, which is less mineralized and less brittle, compensates for enamel and is necessary as a support [VII-10]. Unlike dentin and bone, enamel does not contain collagen. Instead, it has two unique classes of proteins called amelogenins and enamelins. While the role of these proteins is not fully understood, it is believed that they aid in the development of enamel by serving as framework support among other functions [VII-12].

7.2.1 Dentin

Dentin is the substance between enamel or cementum and the pulp chamber. It is secreted by the odontoblasts of the dental pulp [VII-13]. The formation of dentin is known as dentinogenesis. The porous, yellow-hued material is made up of 70% inorganic materials, 20% organic materials, and 10% water by weight [VII-14]. Because it is softer than enamel, it decays more rapidly and is subject to severe cavities if not properly treated, but dentin still acts as a protective layer and supports the crown of the tooth.

Dentin is a mineralized connective tissue with an organic matrix of collagenous proteins. Dentin has microscopic channels, called dentinal tubules, which radiate outward through the dentin from the pulp cavity to the exterior cementum or enamel border [VII-15]. The diameter of these tubules range from 2.5 μm near the pulp, to 1.2 μm in the midportion, and 900 nm near the dentino-enamel junction [VII-16]. Although they may have tiny side-branches, the tubules do not intersect with each other. Their length is dictated by the radius of the tooth. The three dimensional configuration of the dentinal tubules is genetically determined.

7.2.2 Cementum

Cementum is a specialized bony substance covering the root of a tooth [VII-13]. It is approximately 45% inorganic material (mainly hydroxyapatite), 33% organic material (mainly collagen) and 22% water. Cementum is excreted by cementoblasts within the root of the tooth and is thickest at the root apex. Its coloration is yellowish and it is softer than either dentin or enamel. The principal role of cementum is to serve as a

medium by which the periodontal ligaments can attach to the tooth for stability. At the cement-enamel junction, the cementum is acellular due to its lack of cellular components, and this acellular type covers at least ⅔ of the root [VII-17]. The more permeable form of cementum, cellular cementum, covers about ⅓ of the root apex [VII-18].

7.2.3 Pulp

The dental pulp is the central part of the tooth filled with soft connective tissue [VII-14]. This tissue contains blood vessels and nerves that enter the tooth from a hole at the apex of the root [VII-19] along the border between the dentin and the pulp are odontoblasts, which initiate the formation of dentin [VII-14]. Other cells in the pulp include fibroblasts, preodontoblasts, macrophages and T lymphocytes [VII-20]. The pulp is commonly called "the nerve" of the tooth.

7.3 Development

Tooth development is the complex process by which teeth form from embryonic cells, grow, and erupt into the mouth. Although many diverse species have teeth, non-human tooth development is largely the same as in humans. For human teeth to have a healthy oral environment, enamel, dentin, cementum, and the periodontium must all develop during appropriate stages of fetal development. Primary (baby) teeth start to form between the sixth and eighth weeks in utero, and permanent teeth begin to form in the twentieth week in utero [VII-21]. If teeth do not start to develop at or near these times, they will not develop at all.

A significant amount of research has focused on determining the processes that initiate tooth development. It is widely accepted that there is a factor within the tissues of the first branchial arch that is necessary for the development of teeth [VII-22].

Tooth development is commonly divided into the following stages: the bud stage, the cap, the bell, and finally maturation. The staging of tooth development is an attempt to categorize changes that take place along a continuum; frequently it is difficult to decide what stage should be assigned to a particular developing tooth [VII-22]. This determination is further complicated by the varying appearance of different histologic sections of the same developing tooth, which can appear to be different stages.

The tooth bud is an aggregation of cells that eventually forms a tooth. It is organized into three parts: the enamel organ, the dental papilla and the dental follicle [VII-23]. The enamel organ is composed of the outer enamel epithelium, inner enamel epithelium, stellate reticulum and stratum intermedium [VII-23]. These cells give rise to ameloblasts, which produce enamel and the reduced enamel epithelium. The growth of cervical loop cells into the deeper tissues forms Hertwig's Epithelial Root Sheath, which determines a tooth's root shape. The dental papilla contains cells that develop into odontoblasts, which are dentin-forming cells [VII-23]. Additionally, the junction between the dental papilla and inner enamel epithelium determines the crown shape of a tooth [VII-24]. The dental follicle gives rise to three important entities: cementoblasts, osteoblasts, and fibroblasts. Cementoblasts form the cementum of a tooth. Osteoblasts give rise to the alveolar bone around the roots of teeth. Fibroblasts develop the periodontal ligaments which connect teeth to the alveolar bone through cementum [VII-25].

Dentine is a calcified tissue of the body, and along with enamel, cementum and pulp is one of the four major components of teeth. In a natural tooth, it is covered by enamel on the crown and cementum on the root and surrounds the entire pulp. Dentine is made of collagen and hydroxyapatite; its highly ordered microstructure can be modeled as a continuous fibre-reinforced composite, with the intertubular dentine forming the matrix and the tubule lumens with their associated cuffs of peritubular dentine forming the cylindrical fibre reinforcement [VII-26-31].

Dentine has different morphology near the enamel and in the inner part thus mechanical properties progressively change in correspondence of structure variation. Young's modulus and strength are also influenced by tubule orientation, i.e. they are higher in the direction perpendicular to the tubule axis [VII-31].

Furthermore, dentine exhibits time-dependent properties like creep and stress relaxation [VII-32-36].

In clinical dentistry, the knowledge of local dentine properties is important for understanding the effects of the wide variety of restorative dental procedures from the design of preparations to the choice of bonding methods. In the last decade nano-indentation has been applied to measure Young's modulus of mineralized tissues and other biomaterials [VII-37-43]. However, the technique provides data affected by a large scattering because the imprint size is comparable to that of tubule sections. In

addition, surface roughness is an unavoidable drawback when one operates on a nanoscale.

7.4 Damping on human teeth

7.4.1 Introduction

In this work different experimental techniques have been employed to measure the mechanical properties of dentine. Particular attention has been paid to the development of a reliable methodology based on instrumented indentation for the local mechanical characterization of dentine in different tooth positions. FIMEC (Flat-top cylinder Indenter for Mechanical Characterization) is an indentation technique, developed by one of the authors, which employs a cylindrical punch [VII-44-46]. It permits to determine yield stress, Young's modulus and to investigate stress-relaxation and creep behaviour on local scale. In the past it has been successfully used for investigating different types of metals in the temperature range from -180 to 600°C. The experimental apparatus, described in detail in [VII-45], has been suitably modified to operate with lower applied loads and tests have been performed with a punch of diameter $\Phi = 0.5$ mm in different positions of sections of human teeth. The imprint size allows an accurate mapping of mechanical properties but, at the same time, is large enough to avoid large scattering of data. For comparing the results indentation tests with a conical punch have been also performed.

Furthermore, Mechanical Spectroscopy (MS) measurements have been carried out to determine the dynamic modulus and the damping factor Q^{-1}.

7.4.2 Material and Methods

Human molars were extracted from individuals (males 55-70 years old) as part of their dental treatment. After disinfection by immersion in a solution of sodium hypochlorite in water for about 12 hours, they were longitudinally sectioned in order to obtain 2 mm-thick slices.

The sections have been used for Vickers (100 g) micro-hardness and instrumented indentation tests.

From some sections bar-shaped samples (length L = 13 mm, width W = 4 mm, thickness K = 0.8 mm) have been cut for MS measurements. The samples, mounted in free-clamped mode, have been tested with the method of frequency modulation to get dynamic modulus and damping factor Q^{-1}.

The modulus E was obtained from the resonance frequency f (see Eq. I-8).

Q^{-1} values have been determined from the logarithmic decay of flexural vibrations keeping the strain amplitude lower than 1×10^{-5}.

Instrumented indentation tests with both cylindrical (FIMEC) and conical punch have been carried out at a constant penetration rate of 1.7 μms^{-1}. A pre-load of 15 N was applied. The tests with different indenters were made about in the same positions of teeth sections to better compare the results. During each test, applied load P and penetration depth h are measured and loading-unloading P-h curves obtained. Typical trends are shown in fig. VII-2 a).

From the contact stiffness S, i.e. the slope of the initial part of the unloading curves, the equivalent modulus Eq. has been determined [VII-48]:

$$S = \frac{dp}{dh} = \frac{2}{\sqrt{\pi}} \frac{E_{eq}}{\left(1 - \upsilon^2\right)} \sqrt{A(h)} \qquad \text{(VII-1)}$$

with ν the Poisson's ratio of dentine (ν = 0.29 [VII-24]) and A (h) the contact area at the penetration h.

The Young's modulus E was then calculated by the following equation from the FIMEC tests:

$$\frac{1}{E_{eq}} = \frac{1-\upsilon^2}{E} + \frac{1-\upsilon_i^2}{E_i} \qquad\qquad \text{(VII-2)}$$

being vi and E_i Poisson's ratio and Young's modulus of the indenter material respectively. For the cylindrical punch (sintered WC) $v_i = 0.24$ and $E_i = 668$ GPa while for the conical punch (diamond) vi $= 0.29$ and $E_i = 1200$ GPa.

The yield stress σ_Y has been determined from the FIMEC curves according to the procedure described in [VII-44-46]. As shown in fig. VII-2 a), when the load reaches the value p_y the curve shows a sudden slope decrease. The yield stress σ_Y is given by $p_y / 3[\pi (\Phi/2)^2]$. The relationship has been already verified for a lot of materials (pure metals, alloys, composites etc.).

FIMEC test has been also used to carry out local stress-relaxation and creep tests.

Stress-relaxation is significant in clinical situations such as use of threaded post in root canal, placement of pins during endodontic treatments and polymerization contraction of composite restorations [VII-50-52]. To perform stress-relaxation tests, the cylindrical punch penetration has been interrupted at a load of ~ 94 N and the load evolution has been monitored for increasing time up to 4×10^3 s, keeping constant the penetration depth, so load vs. time curves were obtained.

Creep plays an important role in pathological situations such as bruxism, i.e. the grinding of the teeth. In particular, teeth are subjected to constant stress for a period ranging from some seconds to some minutes [VII-53, 54] and this event can be repeated several times, especially at night. The tests have been made by measuring the penetration depth for 25 hours under a constant stress applied.

7.4.3 Results and discussion

Elastic modulus and damping factor of dentine (E = 19 GPa and $Q^{-1} = 1 \times 10^{-2}$) obtained by IF measurements (Fig. VII-4, Fig. VII-5) represent average values. Elastic modulus is in agreement with data of other investigators [VII-55,56] while no data of dentine damping factor have been found in literature. However, Q^{-1} values of human bone ranging from 2×10^{-2} to 4×10^{-2} [VII-57-59] are compatible with that of dentine determined in the present experiments.

Micro-hardness maps on teeth sections show that hardness progressively decreases from the external part (HV = 1 GPa) to the inner one (HV = 0.6 GPa). The scattering of data depends on tooth position varying in the range ± 7-11 %.
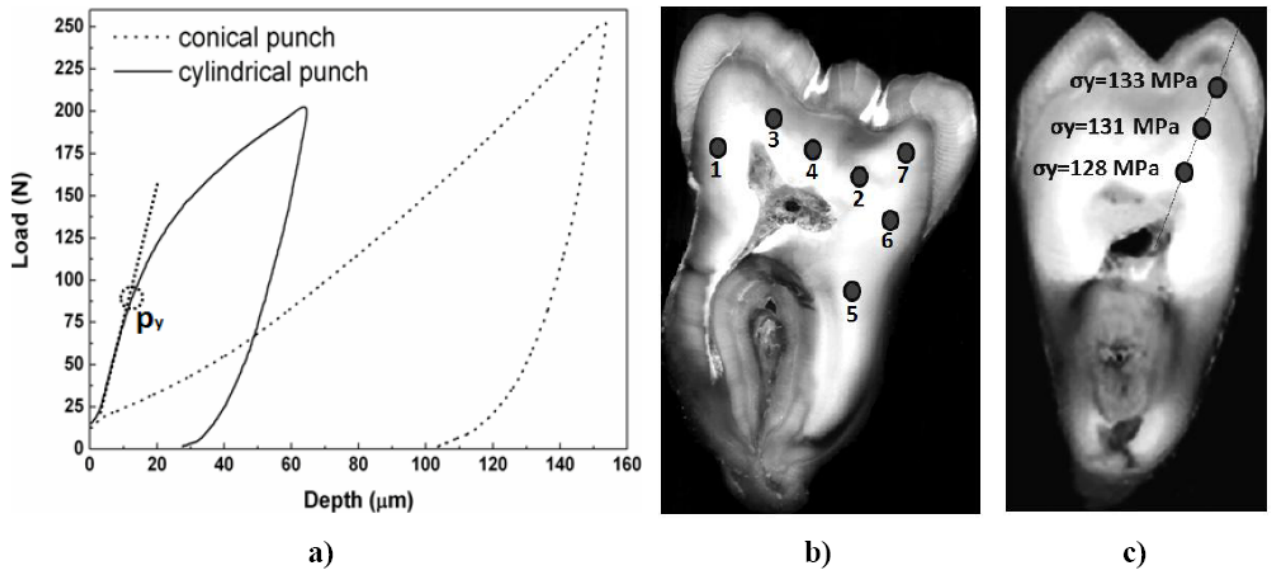

Fig. VII-2 a) Indentation loading-unloading curves obtained with cylindrical and conical punch; b) - c) maps indentation sites of on tooth sections.

Fig. VII-2 b) shows a tooth section and the positions where FIMEC tests have been performed. The corresponding values of Young's modulus are reported in Tab. VII-1 along with those obtained from tests employing the conical punch on another section in similar positions.

Young's modulus of human teeth							
Position	1	2	3	4	5	6	7
E_{cyl} (GPa)	16	16	20	17	16	17	20
E_{con}(GPa)	17	17	19	17	15	18	19

Tab. VII-1: Values of E obtained from indentation tests performed using cylindrical and conical punch. The tests with cylindrical punch have been performed in the positions (1-7) of fig. VII-2 b), those with conical punch in analogous positions of another molar tooth section.

The two sets of data are very close and show that E decreases from the coronal dentine (sites 3 and 7) to the root (site 5) with variations of about 20 %. The results of tests

made in similar positions of different tooth sections exhibit a scattering of ± 1%. There is agreement with literature data obtained with various techniques [VII-37-43].

Yield stress σ_Y determined from FIMEC exhibits a trend similar to that of Young's modulus. An example is reported in Fig. VII-2 c). A pre-molar tooth has been tested along a radial direction from the enamel to the pulp and σ_Y changes from 133 to 128 MPa. In literature a mean value of 130 MPa is reported, determined by compression tests [VII-36].

FIMEC stress-relaxation curves in different tooth positions are displayed in Fig. VII-3 a). The measurements have been performed both on the coronal dentine and on the roots. As shown in fig. VII-3 b), the curves tend to an asymptotic value P_0 and can be interpolated by the function:

$$P = P_0 + P_1 e^{-\frac{t}{\tau_1}} + P_2 e^{-\frac{t}{\tau_2}} \qquad \text{(VII-3)}$$

To simplify, in fig. VII-3 b) the P_0 term has been subtracted from the experimental data. The interpolating function consists of two exponential terms with relaxation times τ_1 and τ_2, which describe two different mechanical processes typical of porous materials.

The first exponential term, $P_1 e^{-t/\tau_1}$, describes the initial steep load decrease corresponding to the structural collapse of dentine walls. The second term, $P_2 e^{-t/\tau_2}$, describes the real stress relaxation, i.e. the progressive and slow change of elastic into plastic strain.

The values of time constants τ_1 and τ_2 exhibit variations of ~ 20% depending on the position where the test is made: τ_1 varies from 159 to 192 s while τ_2 from 1820 to 2300 s.
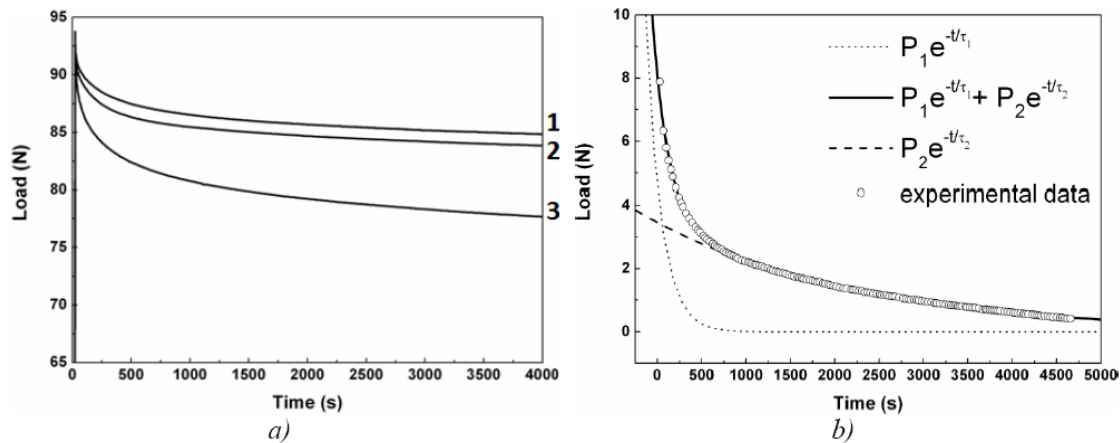
Fig. VII-3 - a) Stress relaxation curves in different tooth position: 1- root, 2- mid coronal dentine, and 3- dentine near the pulp; b) Interpolation of a stress-relaxation curve after subtraction of the asymptotic value P_0.

Typical FIMEC creep curves are displayed in Fig. VII-3. In order to investigate how penetration rate depends on the applied stress, the experimental measurements are carried out on similar positions of different teeth section. The slope *dh/dt* in the second stage (steady state creep) gives the penetration rate. From the curves in Fig. VII-3, penetration rates of 1.12×10^{-4} µm s^{-1} and 1.35×10^{-4} µm s^{-1} have been obtained for the applied stresses of 56 MPa and 110 MPa, respectively.

7.4.4 Conclusions

FIMEC, a technique of instrumented indentation employing a cylindrical punch, has been used to determine elastic modulus, yield stress, stress-relaxation and creep behaviour in different positions of human teeth. The main results can be summarized as follows.

1- All the values from FIMEC tests are in agreement with literature data obtained by various techniques.

2- Elastic modulus data are not affected by a so large scattering as those from micro- and nanoindentation tests.

3- Stress-relaxation curves evidenced a two-stage mechanism of deformation. They can be interpolated by a function with two exponential terms. The first exponential term, corresponding to the initial steep load decrease, describes the structural collapse of the intertubular walls. The second one, corresponding to the long tail of the curve, describes the progressive and slow change of elastic into plastic strain.

4- Creep curves permit to determine on a local scale penetration rate variations depending on the applied stress.

Therefore, FIMEC proved to be a reliable methodology to measure the mechanical properties of dentine on a local scale. In the future it will be employed to extensively study human teeth taking into account factors of clinical interest such as tooth type (i.e. molar, pre-molar, canine and incisive), age and gender.

Furthermore, dynamic modulus and damping factor Q^{-1} have been measured through tests of mechanical spectroscopy and they are showed in Figure VII-4.
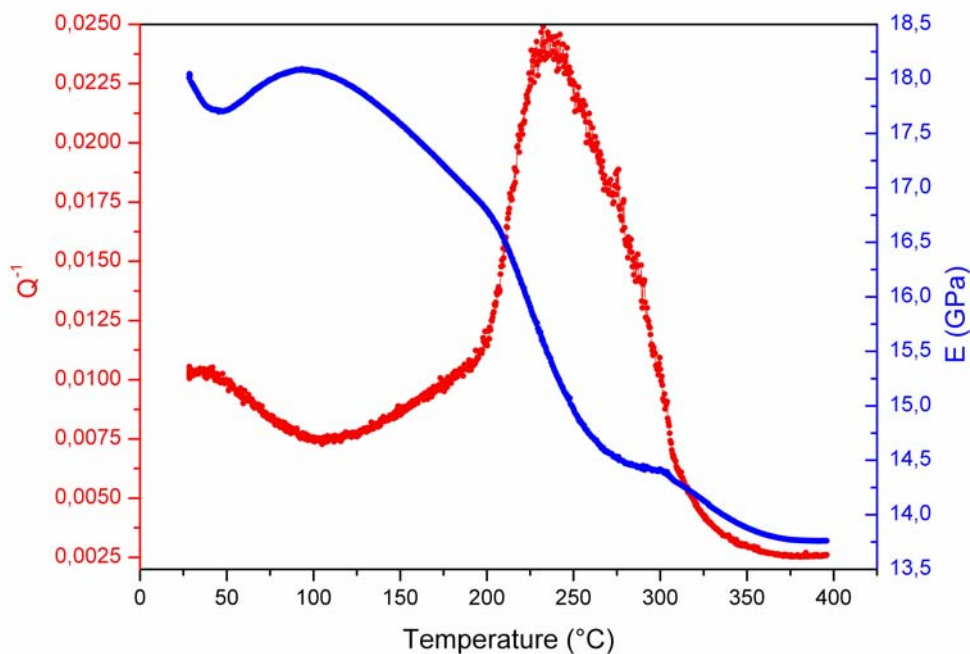

Fig. VII-4 Trend of dynamic modulus and damping factor Q^{-1}.

The value of dynamic modulus E=19 GPa is in good agreement with the literature [VII-55,56].

The peak of internal friction is substantially due to the thermal deterioration of collagen, in fact after successive test runs the peak disappear (Fig. VII-5).
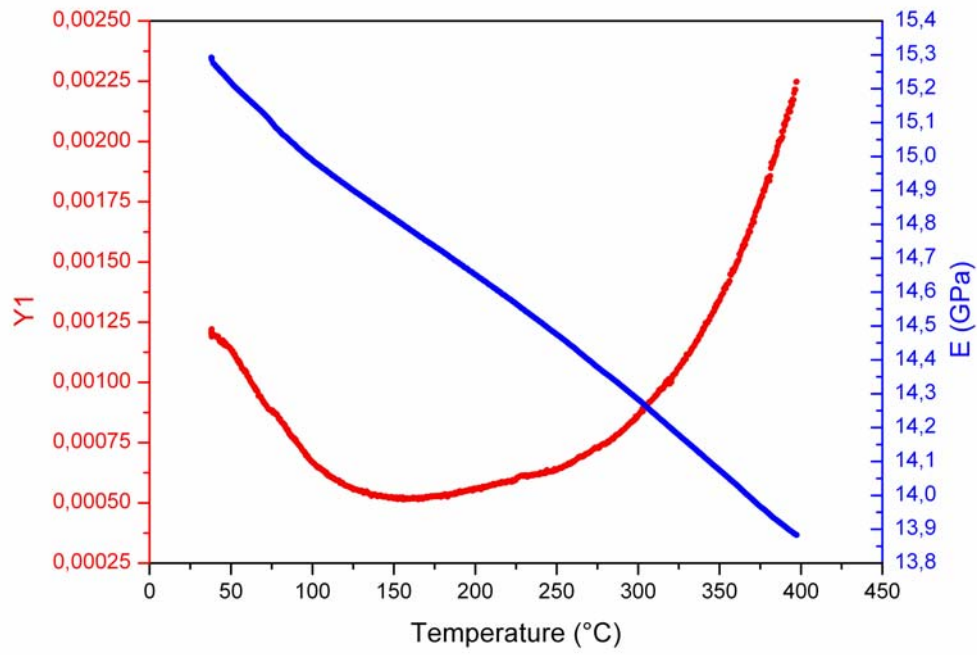
Fig. VII-5 Dynamic modulus and Q^{-1} after successive test runs.

References

[VII-1] Tummers M, Thesleff I (March 2003). "Root or crown: a developmental choice orchestrated by the differential regulation of the epithelial stem cell niche in the tooth of two rodent species". Development 130 (6): 1049–57. doi:10.1242/dev.00332. PMID 12571097.

[VII-2] Hunt AM (1959). "A description of the molar teeth and investing tissues of normal guinea pigs". J. Dent. Res. 38 (2): 216–31. PMID 13641521.

[VII-3] Ash, Major M. and Stanley J. Nelson, 2003. Wheeler's Dental Anatomy, Physiology, and Occlusion. 8th edition. Page 6. ISBN 0-7216-9382-2.

[VII-4] Cate, A.R. Ten. Oral Histology: development, structure, and function. 5th ed. 1998. Page 3. ISBN 0-8151-2952-1.

[VII-5] Ash, Major M. and Stanley J. Nelson, 2003. Wheeler's Dental Anatomy, Physiology, and Occlusion. 8th edition. Page 9. ISBN 0-7216-9382-2.

[VII-6] Kokten G, Balcioglu H, Buyukertan M (November 2003). "Supernumerary fourth and fifth molars: a report of two cases". J Contemp Dent Pract 4 (4): 67–76. PMID 14625596.

[VII-7] Ross, Michael H., Gordon I. Kaye, and Wojciech Pawlina, "Histology: a Text and Atlas", 4th ed. (Baltimore: Lippincott Williams & Wilkins, 2002), p. 441.

[VII-8] Cate, A. R. Ten, "Oral Histology: Development, Structure, and Function", 5th ed. (Saint Louis: Mosby-Year Book, 1998), p. 1.

[VII-9] Cate, A. R. Ten, "Oral Histology: Development, Structure, and Function", 5th ed. (Saint Louis: Mosby-Year Book, 1998), p. 219.

[VII-10] Johnson, Clarke. "Biology of the Human Dentition," 1998. Page accessed on January 24, 2007.

[VII-11] Cate, A. R. Ten, "Oral Histology: Development, Structure, and Function", 5th ed. (Saint Louis: Mosby-Year Book, 1998), p. 219.

[VII-12] Cate, A. R. Ten, "Oral Histology: Development, Structure, and Function", 5th ed. (Saint Louis: Mosby-Year Book, 1998), p. 198.

[VII-13] Ross, Michael H., Gordon I. Kaye, and Wojciech Pawlina, 2003. Histology: a text and atlas. 4th edition. Page 448. ISBN 0-683-30242-6.

[VII-14] Cate, A.R. Ten. Oral Histology: development, structure, and function. 5th ed. 1998. Page 150. ISBN 0-8151-2952-1.

[VII-15] Ross, Michael H., Gordon I. Kaye, and Wojciech Pawlina, 2003. Histology: a text and atlas. 4th edition. Page 450. ISBN 0-683-30242-6.

[VII-16] Cate, A.R. Ten. Oral Histology: development, structure, and function. 5th ed. 1998. Page 152. ISBN 0-8151-2952-1.

[VII-17] Cate, A.R. Ten. Oral Histology: development, structure, and function. 5th ed. 1998. Page 236. ISBN 0-8151-2952-1.

[VII-18] Cate, A.R. Ten. Oral Histology: development, structure, and function. 5th ed. 1998. Page 241. ISBN 0-8151-2952-1.

[VII-19] Ross, Michael H., Gordon I. Kaye, and Wojciech Pawlina, 2003. Histology: a text and atlas. 4th edition. Page 451. ISBN 0-683-30242-6.

[VII-20] Walton, Richard E. and Mahmoud Torabinejad. Principles and Practice of Endodontics. 3rd ed. 2002. Pages 11-13. ISBN 0-7216-9160-9.

[VII-21] A. R. Ten Cate, Oral Histology: Development, Structure, and Function, 5th ed. (Saint Louis: Mosby-Year Book, 1998), p. 95. ISBN 0-8151-2952-1.

[VII-22] A. R. Ten Cate, Oral Histology: Development, Structure, and Function, 5th ed. (Saint Louis: Mosby-Year Book, 1998), p. 81. ISBN 0-8151-2952-1.

[VII-23] University of Texas Medical Branch. "Lab Exercises: Tooth development."

[VII-24] A. R. Ten Cate, Oral Histology: Development, Structure, and Function, 5th ed. (Saint Louis: Mosby-Year Book, 1998), pp. 86 and 102. ISBN 0-8151-2952-1.

[VII-25] Ross, Michael H., Gordon I. Kaye, and Wojciech Pawlina. Histology: a text and atlas. 4th edition, p. 453. 2003. ISBN 0-683-30242-6.

[VII-26] G.W. Jr Marshall: Quintessence Int. Vol. 24 (1993), p. 606

[VII-27] D.H. Pashley: Crit. Rev. Oral. Biol. Med. Vol. 7 (1996), p. 104

[VII-28] J.H. Kinney, S.J. Marshall, G.W. Marshall: Crit. Rev. Oral. Biol. Med. Vol. 14 (2003), p. 13

[VII-29] J.H. Kinney, M. Balooch S.J. Marshall, G.W. Marshall: Arch. Oral. Biol. Vol. 44 (1999), p. 813

[VII-30] Q.H. Qin, M.V. Swain: Biomaterials Vol. 25 (2004), p. 5081

[VII-31] J.H. Kinney, J.R. Gladden, G.W. Marshall, J.H. So, J.D. Maynard: J. Biomech. Vol. 37 (2004),
p. 437

[VII-32] R.G. Craig, F.A. Peyton: J. Dent. Res. Vol. 37 (1958), p. 710

[VII-33] M.G. Duncanson, E. Korostoff: J. Dent. Res. Vol. 54 (1975), p. 1207

[VII-34] E. Korostoff, S.R. Pollack, M.G. Duncanson: J. Biomed. Mater. Res. Vol. 9 (1958), p. 661

[VII-35] H.G. Tengrove, G.M. Carter, J.A. Hood: Dent. Mater. Vol. 11 (1995), p. 310

[VII-36] J. Jantarat, J.E.A. Palmara, C. Lynder, H.H. Messer: Dent. Mater. Vol. 18 (2002), p. 486

[VII-37] H. Kinney, M. Balooch S.J. Marshall, G.W. Marshall, T.P. Weihs: Arch. Oral. Biol. Vol. 41

(1996), p. 9

[VII-38] W. Tesch, N. Eidelman, P. Roschger, F. Goldenberg, K. Klaushofer, P. Fratzl: Calcif. Tissue

Int. Vol. 69 (2001), p. 147

[VII-39] S. Habelitz, S.J. Marshall, G.W. Marshall, M. Balooch: Arch. Oral. Biol. Vol. 46 (2001), p.

173

[VII-40] G. Balooch, G.W. Marshall, S.J. Marshall, O.L. Warren, S.A.S. Asif, M. Balooch: J. Biomech.

Vol. 37 (2004), p. 1223

[VII-41] P. K. Zysset, X.E. Guo, C.E. Hoffler, K.E. Moore, S.A. Goldstein: J. Biomech. Vol. 32 (1999),

p. 1005

[VII-42] M.L. Oyen: J. Biomech. Vol. 39 (2006), p. 2669

[VII-43] E. Mahoney, A. Holt, M. Swain, N. Kilpatrick: J. Dent. Vol. 28 (2000), p. 589

[VII-44] P. Gondi, R. Montanari, A. Sili, J. Nucl. Mater. Vol. 212-215 (1994), p. 1688

[VII-45] B. Riccardi, R. Montanari: Mater. Sci. Eng. A Vol. 281–291(2004), p. 381

[VII-46] R. Montanari, G. Filacchioni, B. Iacovone, P. Plini, B. Riccardi: J. Nucl. Mater. Vol. 648-652

(2007), p. 367

[VII-47] S. Amadori, E.G. Campari, A.L. Fiorini, R. Montanari, L. Pasquini, L. Savini, E. Bonetti:

Mater. Sci. Eng. A Vol. 442 (2006), p. 543

[VII-48] W.C. Oliver, G.M. Pharr: J. Mater. Res. Vol. 1564-1583, (1998), p. 7

[VII-49] H. Gercek: Int. J. Rock Mech. Min. Vol. 44, (2007), p. 1

[VII-50] A.A. Suliman, D.B. Boyer, R.S. Lakes: Dent. Mater. Vol. 9 (1993), p. 6

[VII-51] N. Meredith, D.J. Setchell: J. Dent. Vol. 25 (1997), p. 331

[VII-52] R.S. Ross, J.I. Nicholls, G.W. Harrington: J. Endod. Vol. 17 (1991), p. 450

[VII-53] N.G. Clarke, G.C. Townsend, S.E. Carey: J. Oral. Rehabil. Vol. 11 (1984), p. 123

[VII-54] D.M. Dettmar, R.M. Shaw, A.J. Tilley: Dent. J. Aust. Vol. 32 (1987), p. 421

[VII-55] F. Povolo, E.B. Hermida: J. Alloy Compd. Vol. 310 (2000), p. 392

[VII-56] J.S. Rees, P.H. Jacobsen, J. Hickman: Clin. Mater. Vol. 17 (1994), p. 11

[VII-57] T. Wanga, Z. Fenga: Mater. Lett. Vol. 59 (2005), p. 2277

[VII-58] Y.N. Yeni, R.R. Shaffer, K.C. Baker, X.N. Dong, M.J. Grimm, C.M. Les, D.P. Fyhrie: J.
Biomed. Mater. Res. Vol. 82 (2007), p. 530

[VII-59] J. Yamashita, X. Li, B.R. Furman, H. R. Rawls, X. Wang, M.Agrawal: J. Biomed. Mater. Res.
Vol. 63 (2002), p. 31